

University of Mississippi

eGrove

Electronic Theses and Dissertations

Graduate School

1-1-2022

Abaqus Implementation of a Hyperelastic Damage Model for Glass-Reinforced Polymers under Shock and Impact Loading

James Stuart Fraser

Follow this and additional works at: <https://egrove.olemiss.edu/etd>

Recommended Citation

Fraser, James Stuart, "Abaqus Implementation of a Hyperelastic Damage Model for Glass-Reinforced Polymers under Shock and Impact Loading" (2022). *Electronic Theses and Dissertations*. 2217.
<https://egrove.olemiss.edu/etd/2217>

This Thesis is brought to you for free and open access by the Graduate School at eGrove. It has been accepted for inclusion in Electronic Theses and Dissertations by an authorized administrator of eGrove. For more information, please contact egrove@olemiss.edu.

ABAQUS IMPLEMENTATION OF A HYPERELASTIC DAMAGE MODEL FOR GLASS-
REINFORCED POLYMERS UNDER SHOCK AND IMPACT LOADING

A Thesis
presented in partial fulfillment of requirements
for the degree of Master of Science
in the Department of Mechanical Engineering
The University of Mississippi

by

JAMES S. FRASER

May 2022

Copyright James S. Fraser 2022

ALL RIGHTS RESERVED

ABSTRACT

Accurate computational modeling of the ballistic response of heterogeneous materials is crucial when designing lightweight armor and protective structures. Currently, due to the structural complexity inherent in composites, this behavior is poorly understood. In the present work, a novel computational model to describe the glass fiber-reinforced polymer (GRP) response to shock and impact loadings was implemented in the commercially available Abaqus[®] finite element software via a VUMAT subroutine. Before damage initiation, the model utilized an experimentally-determined tetragonally-symmetric stiffness matrix for the elastic representation of the GRP. Once damage was initiated, a hyperelastic continuum damage mechanics (CDM) based model described the GRP behavior. The shock and impact simulations utilized plate-on-plate impact and projectile penetration tests respectively. Calibration of the computational model involved simulation of a plate-impact experiment available in open literature, whereby a thick steel or aluminum flyer plate impacted a thin GRP plate at velocities ranging from 111.69 m/s to 417.96 m/s. User-defined computational model parameters were calibrated to realistically match the experimental particle velocity profiles. To validate the calibrated model, Abaqus simulations of fragment-simulating projectile (FSP) penetration into 44 mm thick GRP targets at velocities ranging from 246 m/s to 800 m/s were performed. A sensitivity study was performed to investigate the influence of fiber and matrix damage parameters on depth-of-penetration (DOP). The computational results underestimated the DOP and the GRP back surface displacement while showing good agreement with peak compressive shock stresses at different through-thickness depths compared to experimental values. Furthermore, matrix and fiber damage propagation and

concentrations throughout the GRP were investigated, revealing profound GRP degradation occurred approximately 50 μ s after the initial impact. A wider lateral region of matrix and fiber failure was observed closer to the GRP impact and rear surfaces, and fiber damage was observed to be primarily caused by compressive failures.

LIST OF ABBREVIATIONS AND SYMBOLS

GRP	Glass Fiber-Reinforced Polymer
FCM	Fraser Computational Model
FRP	Fiber Reinforced Polymer
CDM	Continuum Damage Mechanics
FSP	Fragment Simulating Projectile
DOP	Depth of Penetration
VISAR	Velocity Interferometer System for any Reflector
HEL	Hugoniot Elastic Limit
LLM	Lawrence Livermore Model
ALE	Arbitrary Lagrangian-Eulerian
LLNL	Lawrence Livermore National Laboratory
CT	Computed Tomography
EEC	Elastic-Elastic Cracking
FEM	Finite Element Method
C_{ij}	Elastic Stiffness Matrix Constants
σ_{ij}	Stress Vector Components
ε_{ij}	Strain Vector Components
ψ	Helmholtz Free Energy
\mathbf{F}	Deformation Gradient Tensor
\mathbf{C}	Right Cauchy Strain Tensor

I_1, I_4, I_6	Invariants
J	Jacobian
G	Shear Modulus
K	Bulk Modulus
β	Ogden Parameter
k_i	Fiber Stiffness
\mathbf{M}_i	Fiber Reference Direction Vector
\mathbf{m}_i	Fiber Current Direction Vector
\mathbf{S}	Second Piola-Kirchoff Stress Tensor
$\boldsymbol{\sigma}$	Cauchy Stress Tensor
\mathbf{b}	Left Cauchy Strain Tensor
R^{MS}	Matrix Shear Damage Criterion
ε_{eq}	Equivalent Strain
ε^{MS}	Critical Matrix Shear Strain
R^{ME}	Matrix Bulk Damage Criterion
α	Bulk Damage Criterion Empirical Constant
J_e^c	Critical Matrix Relative Volume Expansion Strain Under Compression
J_e^t	Critical Matrix Relative Volume Expansion Strain Under Tension
R^M	General Matrix Damage Criterion
d^M	General Matrix Damage Term

ι	Matrix Damage Damping Constant
R^{ft}	Tensile Fiber Damage Criterion
ε^{ft}	Critical Fiber Tensile Strain
η	Buckled Fiber Stiffness Constant
R^{fc}	Compression Fiber Damage Criterion
ε^{fc}	Critical Fiber Compressive Strain
d^f	Fiber Damage Term
var	Strain Rate Dependent Variable
c_1	Strain Rate Dependency Weighting Constant
$\dot{\varepsilon}_{ref}$	Reference Strain Rate
$\dot{\varepsilon}_{eq}$	Equivalent Strain Rate
\mathbf{R}	Orthogonal Rotation Tensor
\mathbf{U}	Right Stretch Tensor
\mathbf{V}	Left Stretch Tensor
W	Work
IE	Internal Energy
σ_H	Hugoniot Stress
ρ_0	Density
U_s	Shock Velocity
u_p	Particle Velocity

ϵ_H	Hugoniot Strain
C_0	Zero Pressure Sound Velocity
S	Empirical Shock Velocity Parameter
V	Volume
t	Thickness
n	Total Number of Imaging Slices
m	Slice Number of Maximum Penetration
C_L	Longitudinal Wave Speed
e_v	Volumetric Strain
P	Pressure

ACKNOWLEDGEMENTS

I want to express my gratitude to Dr. Arunachalam Rajendran, for his expertise, energy, and guidance in developing this research. I want to thank my supervisors Dr. Aaron Joy and Dr. Shan Jiang, who provided me the opportunity and financial support to complete this thesis. I also want to express my appreciation to Huadian Zhang for his instruction in learning Fortran, and to Matt Nelms for his advanced insight into how to best utilize Abaqus.

To my family, Kelly, and Kelly's family, thank you for your unwavering kindness and support in my academic and life endeavors. To my Cajun friends, I miss you all and thank you for your support during this time.

TABLE OF CONTENTS

ABSTRACT.....	ii
LIST OF ABBREVIATIONS AND SYMBOLS	iv
ACKNOWLEDGEMENTS	viii
LIST OF TABLES	xii
LIST OF FIGURES	xiii
INTRODUCTION	1
METHODOLOGY AND DEVELOPMENT	6
II.1 ELASTIC FCM MODEL	7
II.2 HYPERELASTIC FCM MODEL	8
II.2.A CONSTITUTIVE THEORY.....	8
II.2.B DAMAGE MODEL	10
II.3 VUMAT CONSTRUCTION.....	15
II.3.A INITIALIZATION.....	16
II.3.B SUBROUTINE BODY	19
EXPERIMENTAL BENCHMARKS AND SIMULATIONS	29
III.1 PLATE IMPACT TEST.....	29
III.2 PLATE IMPACT BENCHMARK DATA.....	30

III.3 BALLISTIC PENETRATION TESTS	33
III.4 BALLISTIC PENETRATION BENCHMARK RESULTS	34
ABAQUS SIMULATIONS	37
IV.1 PLATE IMPACT SIMULATION	37
IV.2 BALLISTIC PENETRATION SIMULATION	39
RESULTS AND DISCUSSION	43
V.1 PLATE IMPACT RESULTS	43
V.1.A ELEMENT SIZE	44
V.1.B OGDEN PARAMETER	47
V.1.C MATRIX SHEAR DAMAGE STRAIN RATE DEPENDENCY	51
V.1.D COMPRESSIVE MATRIX BULK DAMAGE.....	53
V.1.E MATRIX DAMAGE DAMPING.....	56
V.1.F ELASTIC UNDAMAGED MODELS	57
V.1.G DAMAGE-CAPTURING MODELS	60
V.2 BALLISTIC PENETRATION RESULTS.....	69
V.2.A TENSILE BULK DAMAGE.....	69
V.2.B FIBER BUCKLING STIFFNESS	71
V.2.C DOP AND REAR BULGE ANALYSIS	72

V.2.D STRESS ANALYSIS	74
V.2.E STRAIN ANALYSIS.....	79
V.2.F FIBER AND MATRIX DAMAGE.....	84
SUMMARY	89
BIBLIOGRAPHY.....	93
APPENDIX.....	97
APPENDIX A	98
APPENDIX B	99
APPENDIX C	106
APPENDIX D	108
VITA.....	109

LIST OF TABLES

Table 1. Elastic constants of the GRP.....	7
Table 2. Symmetric tensor	17
Table 3. Asymmetric tensor.....	17
Table 4. Plate impact experimental results	30
Table 5. Shock velocity, Hugoniot Stress, and Hugoniot strain data for the GRP.....	32
Table 6. DOP and related data for 44 mm thick GRP targets.....	35
Table 7. Abaqus plate impact model mesh details.....	38
Table 8. Abaqus user-defined material properties	39
Table 9. Element sizes for GRP penetration simulation.....	41
Table 10. Element thickness effects on shock wave arrival time	47
Table 11. Abaqus simulation user-material properties and parameters	58
Table 12. Model stress and strain comparison to Hugoniot values	60
Table 13. Compressive and tensile wave arrival times.....	75
Table 14. Peak compressive shock stress comparison.....	76
Table 15. Fiber damage onsets determined from R^{fit} and R^{fic}	86

LIST OF FIGURES

Figure 1. GRP elastic stiffness matrix	7
Figure 2. Compressive Bulk Damage Criterion Evolution, $\alpha=1 \times 10^{-9}$, $J_e^c=0.04$	13
Figure 3. Abaqus user-material properties window displaying property assignments	18
Figure 4. Plate impact test experimental schematic.....	29
Figure 5. Selected experimental free surface particle velocity VISAR data	31
Figure 6. Ballistic penetration stress measurement setup	34
Figure 7. Effect of fragment mass and strike velocity on DOP	35
Figure 8. Stress profiles at 9 mm and 20 mm depths for a 246 m/s 20 mm caliber FSP impact..	36
Figure 9. Mesh size variation on the GRP impact face.....	42
Figure 10. Element size particle velocity profile comparisons.....	46
Figure 11. β effect on the undamaged hyperelastic model	48
Figure 12. Pressure and strain response to β changes.....	49
Figure 13. Bulk modulus evolution for different β values.....	50
Figure 14. Matrix shear damage strain rate effect on velocity profiles	52
Figure 15. Matrix shear damage criterion response to strain rate weighting.....	52
Figure 16. Matrix bulk damage response to α changes.....	54
Figure 17. J_e^c effects on matrix bulk damage	55
Figure 18. Collection of J_e^t and α combinations and their effects on particle velocity profiles...	56
Figure 19. ι damping effect on particle velocity profiles.....	57
Figure 20. Undamaged elastic model comparison to experimental data	60

Figure 21. FCM prediction for free surface particle velocity at low, intermediate, and high-velocity plate impacts	61
Figure 22. Velocity profile comparison between the FCM calibrated to high-velocity and low-velocity tests.....	63
Figure 23. GRP shock stress history at different distances from the impact surface.....	64
Figure 24. Matrix damage evolution at different distances from the impact surface	65
Figure 25. Contributions of shear and bulk matrix damage criteria comparison.....	66
Figure 26. Decoupled damage effect on lateral shock stress	67
Figure 27. GRP lateral shock stress at different distances from the impact surface.....	68
Figure 28. Compressive shock stress evolution in terms of volumetric strain	69
Figure 29. DOP response to J_e^t changes	70
Figure 30. DOP responses to η changes	71
Figure 31. DOP comparison between FCM and experimental test data.....	72
Figure 32. Rear surface displacement comparison between FCM and experimental data	74
Figure 33. Stress in shock direction evolution at different GRP depths.....	75
Figure 34. "Centered" element set shock stress time history.....	76
Figure 35. "Radial" element set shock stress time history.....	77
Figure 36. "Centered" element set lateral stress time history	78
Figure 37. "Radial" element set lateral stress time history	79
Figure 38. "Centered" element set maximum principal logarithmic strain time history	80
Figure 39. "Centered" element set nominal strain in shock direction time history	81

Figure 40. "Radial" element set nominal strain in shock direction time history	81
Figure 41. "Centered" element set maximum principal nominal strain with particle conversion threshold = 4.6	82
Figure 42. "Centered" element set lateral (x-direction) nominal strain time history	83
Figure 43. "Radial" element set lateral (x-direction) nominal strain time history	84
Figure 44. "Centered" element set fiber and matrix damage time history	85
Figure 45. "Radial" element set fiber and matrix damage time history	85
Figure 46. Matrix damage progression contours: rows represent the position on or through the GRP thickness, columns represent time stamps	87
Figure 47. Fiber damage progression contours: rows represent the position on or through the GRP thickness, columns represent time stamps	88

CHAPTER I

INTRODUCTION

The demand in many fields for increasingly advantageous properties in new materials has fueled the development of fiber-reinforced polymer (FRP) composites. Studying the complex dynamic response of these heterogeneous materials is challenging, yet crucial to understanding their usefulness for desired applications. In military and civil applications, it is important to accurately model the response of FRP-type composites subject to high-velocity impacts when designing protective structural or armor systems. A fundamental understanding of how glass fiber-reinforced polymers (GRP) dissipate and mitigate energy under dynamic loading conditions can lead to the optimization of these systems. In contrast to the existing understanding of the ballistic response of homogenous materials such as metals and ceramics, the dynamic response of heterogeneous materials is poorly understood. The complexity of modeling the constitutive response of GRP stems from its architecture. Variable woven construction, multiple constituent materials, and a multitude of failure modes contribute to a highly nonlinear impact response. For plate impact and projectile penetration testing, multi-axial loading conditions may induce failure mechanisms such as tensile fiber breakage, fiber shearing, compressive fiber damage, matrix microcracking, and delamination. An in-depth discussion on composite failure modes is outside the scope of this paper, yet much literature exists on the topic [1]–[7].

To attain a fundamental understanding of the GRP response to impact, idealized conditions can be utilized, as in the case of a one-dimensional plate impact test creating a one-dimensional strain state. Shock responses of many materials (ceramics, metals, concrete, cement, and layered

composites) have historically been tested using this method [8]–[10]. Signor et al. [8] used plate impact testing to investigate the transition from solid-state spalling to molten-state micro-spalling in metals. Elamin and Varga [10] reviewed the fundamentals of various types of plate impact experiments and recent innovations in the field. Most of these experiments were performed to develop models to predict failure (such as spallation) in metals and ceramics under tensile loading conditions. However, the damage processes in GRP under shock include compressive failure due to several failure mechanisms. Tsai et al. [11] conducted shock wave propagation experiments to study the compressive failure of GRP and whose data is used extensively in this paper. In their tests, thick (~25 mm) metallic flyer plates were launched at velocities ranging from 8.5 m/s to 417.96 m/s to impact a stationary thin (~3-20 mm thick) S2 glass/polyester target sample. VISAR (Velocity Interferometer System for Any Reflector) was used to measure the velocity of the target sample's back free surface, providing insight into the shock wave compression and release paths. Physically, impact-induced compressive stresses are transmitted as a stress pulse to unstressed regions of the target in microseconds. Once the pulse arrives at a GRP's stress-free back surface, the wave reflects back into the GRP as a tensile release (or unloading) wave to generate an unstressed state in the GRP. When the compressive pulse and the tensile release wave interact, the material unloads towards an unstressed state. In the experiments of Tsai et al., during the VISAR measurements, no release waves from any lateral surfaces contributed and therefore, the time history of particle velocity only accounted for the compressive response of the GRP.

A transition from elastic to plastic behavior within the material can also be induced by compressive stresses exceeding the Hugoniot Elastic Limit (HEL). This limit represents the maximum one-dimensional compression stress a material can undergo before the internal structure rearranges at the shock front, initiating plasticity (or permanent strain). The heterogeneity and

stacked lamina structure of a GRP makes finding its HEL notably more difficult under the elastic or hyperelastic response of GRP. Though a theoretical approach to calculating stresses is possible by accounting for impedance changes in the GRP plies, the added dimensions of damage initiation and propagation demand the use of computational modeling.

The computational model presented in this paper is referred to as the Fraser Computational Model (FCM) to distinguish the developed model by name from other computational models referenced throughout this thesis. The FCM combines an anisotropic linear elastic model using constants provided by Tsai et al. [11] with elements of a hyperelastic large-strain-based continuum damage mechanics (CDM) model proposed by Barham et al. [12] at the Lawrence Livermore National Laboratory (LLNL). For this thesis, the model by Barham et al. is referred to as the Lawrence Livermore Model (LLM). The governing constitutive relation of the hyperelastic FCM is based on the Helmholtz free energy function. The hyperelastic FCM encompasses isotropic and anisotropic terms, as well as several constants that describe damage initiation and growth due to mechanisms such as matrix microcracking, fiber buckling, and fiber breakage under tensile and compressive loads. Though the LLM was optimized for use with Arbitrary Lagrangian-Eulerian (ALE) finite element software such as ALE3D [13], the FCM was implemented in the Abaqus finite element software through the construction of a VUMAT subroutine.

The initial aim of the FCM is to match the experimental data of Tsai et al. [11] for multiple thin-GRP plate impact tests and provide a quantitative visualization of the physical response seen in the GRP. The particle velocity profiles obtained by Tsai et al. illustrate the complex elastic and plastic (or inelastic) behaviors of GRPs subjected to a range of plate impact velocities. For calibration of the FCM parameters, velocity profile features such as rise time, shock front elastic-inelastic transition velocity, velocity tapering, and the peak velocity are focused on. The calibration

of user-defined model parameters used in the FCM is benchmarked against particle velocity data from a high-velocity (417.96 m/s) plate impact test. This test was deemed most applicable for calibration due to the higher projectile velocities encountered in bullet penetration simulations.

The main objective of the present work is to validate the applicability of the FCM implementation in Abaqus through simulations of ballistic tests on GRP samples utilizing the model parameters determined from plate impact experiments. Experimental Fragment Simulating Projectile (FSP) penetration test results from Prifti et al. [14] provide the depth-of-penetration (DOP) and rear surface displacement data to which the FCM is compared. Using the same experimental environment, internal shock stress data obtained by Rajendran et al. [15] is compared to the FCM. These penetration depth tests are replicated and simulated in Abaqus to study the damage evolution in GRP due to a wide range of failure mechanisms. The contour plots of various damage parameters provide an insight into how the energy is dissipated laterally and longitudinally due to the fiber reinforcement.

Chapter II of this thesis covers the governing theory of the elastic and hyperelastic damage constituents of the FCM, and how these are constructed in the Abaqus/Explicit VUMAT subroutine. For the sake of completion, Chapter III details the experiments Tsai et al. [11] performed to generate particle velocity profiles, as well as the ballistic penetration experiments run by Prifti et al. [14] to attain DOP and rear surface displacement data, and by Rajendran et al. [15] to obtain internal shock stress data. In Chapter IV, some salient details of the Abaqus model simulations for the plate impact test and FSP penetration test configurations are provided. Chapter V presents the results of sensitivity studies performed on Abaqus element geometry and several user-defined damage-related FCM parameters. For plate impact implementation, results of a hyperelastic-only model are compared to the FCM for undamaged and damage-enabled model

configurations. The FCM is examined with regard to the experimental results of Tsai et al. and the salient features of the velocity profiles the FCM captures. The FCM model implementation culminates with an investigation into the GRP response to FSP penetration simulations. DOP, rear surface displacement, and internal shock stress comparisons are made between the FCM and experimental results. An insight into the damage response of the GRP is attained through contour plots, highlighting regions of concentration of certain damage modes. A closing summary of the above results follows in Chapter VI.

CHAPTER II

METHODOLOGY AND DEVELOPMENT

As a preface, the LLM developed by Barham et al. [12] was specifically built for ALE finite element code implementation. The authors noted that this application dictated their decision to minimize the usage of vector and tensor history variables. Instead of a more commonly used damage tensor, scalar damage variables representative of physical phenomena are used. Though Abaqus uses a different numerical method to ALE3D, this choice by Barham et al. benefited the model's implementation in a VUMAT.

The LLM constitutive equations follow large deformation theories using right Cauchy-Green strain tensors. The model assumes that damage initiation under different failure modes occurs when strain exceeds a certain critical value. A two-parameter exponential relationship describes damage growth under different modes: matrix cracking under shear, matrix cracking under extension/contraction, fiber breakage under tension, fiber buckling under compression, and ply delamination. The LLM also allows strain rate dependency in all model constants through an ad-hoc one-parameter logarithmic equation. This parameter governs strain rate sensitivity for each failure mode. Using the conventional CDM approach, the shear and bulk moduli are degraded as the damage parameter increases from zero to one. The LLM assumes no permanent deformation and therefore, in principle, the model implementation into any FEA code is fairly simple. In this thesis work, a three-dimensional CDM-based hyperelastic model (the FCM) was implemented into Abaqus through the user-defined material VUMAT subroutine.

II.1 ELASTIC FCM MODEL

Before the initiation of any damage, the GRP exhibits anisotropic elastic behavior. Tsai et al. [11] reported six independent elastic constants of the tetragonal symmetry stiffness matrix as shown in Table 1 and Fig. 1.

Table 1. Elastic constants of the GRP

Elastic constants	GPa
C_{11}	31.55
C_{33}	20.12
C_{44}	4.63
C_{66}	4.94
C_{12}	15.86
C_{13}	9.75

$$\begin{bmatrix} C_{11} & C_{12} & C_{13} & 0 & 0 & 0 \\ C_{12} & C_{11} & C_{13} & 0 & 0 & 0 \\ C_{13} & C_{13} & C_{33} & 0 & 0 & 0 \\ 0 & 0 & 0 & C_{44} & 0 & 0 \\ 0 & 0 & 0 & 0 & C_{44} & 0 \\ 0 & 0 & 0 & 0 & 0 & C_{66} \end{bmatrix}$$

Figure 1. GRP elastic stiffness matrix

The elastic stress-strain relationship for the undamaged GRP is described by the generalized

Hooke's Law:

$$\begin{bmatrix} \sigma_{xx} \\ \sigma_{yy} \\ \sigma_{zz} \\ \sigma_{yz} \\ \sigma_{zx} \\ \sigma_{xy} \end{bmatrix} = \begin{bmatrix} C_{11} & C_{12} & C_{13} & 0 & 0 & 0 \\ C_{12} & C_{11} & C_{13} & 0 & 0 & 0 \\ C_{13} & C_{13} & C_{33} & 0 & 0 & 0 \\ 0 & 0 & 0 & C_{44} & 0 & 0 \\ 0 & 0 & 0 & 0 & C_{44} & 0 \\ 0 & 0 & 0 & 0 & 0 & C_{66} \end{bmatrix} \begin{bmatrix} \varepsilon_{xx} \\ \varepsilon_{yy} \\ \varepsilon_{zz} \\ 2\varepsilon_{yz} \\ 2\varepsilon_{zx} \\ 2\varepsilon_{xy} \end{bmatrix} \quad (1)$$

This elastic model is what is used in the FCM before damage initialization. The LLM proposed by Barham et al. [12] assumed the elastic response as homogeneous isotropic using the GRP's shear and bulk moduli and employed a hyperelastic constitutive relation. A comparison between the

elastic FCM and the undamaged hyperelastic LLM model is presented in the Results and Discussion chapter.

II.2 HYPERELASTIC FCM MODEL

Once damage in the GRP initiates, the FCM model follows the hyperelastic damage formulation of Barham et al. [12], with modifications made to damage contributions.

II.2.A CONSTITUTIVE THEORY

The constitutive equation is derived from the Helmholtz free energy function, with the addition of anisotropic terms to represent fiber contributions. The Helmholtz free energy ψ is a scalar function of deformation:

$$\psi = \psi(\mathbf{F}) = \psi(\mathbf{C}) \quad (2)$$

where \mathbf{F} is the deformation gradient tensor and \mathbf{C} is the right Cauchy strain tensor. The strain-based Helmholtz free energy is a function of strain invariants and the Jacobian, where each term is tied to a specific assumed physical contribution:

$$\psi(I_1, J, I_4, I_6) = \frac{G}{2} \left(I_1 J^{\frac{2}{3}} - 3 \right) + \frac{K}{\beta^2} \left(\beta \ln(J) + J^{-\beta} - 1 \right) + \frac{k_1}{2} (I_4 - 1)^2 + \frac{k_2}{2} (I_6 - 1)^2 \quad (3)$$

where G and K are the shear and bulk modulus respectively of the isotropic GRP, J is the Jacobian, β is the Ogden parameter, k_1 and k_2 are the Young's modulus of the fibers in reference directions 1 and 2 respectively, and I_1 , I_4 and I_6 are invariants. Definitions for the invariants and the Jacobian are:

$$I_1 = \text{tr}(\mathbf{C}) \quad (4)$$

$$\mathbf{C} = \mathbf{F}^T \mathbf{F} \quad (5)$$

$$I_4 = \mathbf{M}_1 \cdot \mathbf{C} \mathbf{M}_1 \quad (6)$$

$$I_6 = \mathbf{M}_2 \cdot \mathbf{C} \mathbf{M}_2 \quad (7)$$

$$J = \det(\mathbf{F}) \quad (8)$$

where \mathbf{M}_1 and \mathbf{M}_2 are fiber reference direction vectors. The $\frac{G}{2} \left(I_1 J^{\frac{2}{3}} - 3 \right)$ term is an isochoric contribution, derived from the Neo-Hookean model for incompressible hyperelasticity. It is applicable for stiff rubbers and cross-linked polymers subjected to strains less than 0.5. The $\frac{K}{\beta^2} (\beta \ln(J) + J^\beta - 1)$ term is derived from the Ogden model for compressible hyperelasticity and is a volumetric contribution. The Ogden parameter β is one of the variables calibrated to experimental particle velocity profiles; its sensitivity study results are presented in the following chapter. The anisotropic $\frac{k_1}{2} (I_4 - 1)^2$ and $\frac{k_2}{2} (I_6 - 1)^2$ terms are associated with fiber stretch. The FCM assumes no fiber-fiber interaction and is therefore only applicable for stacked unidirectional plies and not suitable for woven architectures.

The constitutive relation in terms of Second Piola-Kirchoff stress is found by differentiating the Helmholtz free energy function with respect to the right Cauchy strain according to Eq. (9).

$$\mathbf{S} = 2 \frac{\partial \psi}{\partial \mathbf{C}} = 2 \sum \left(\frac{\partial \psi}{\partial I_i} \cdot \frac{\partial I_i}{\partial \mathbf{C}} \right) \quad (9)$$

Performing this operation on the free energy function yields:

$$\mathbf{S} = \frac{G}{J^{\frac{2}{3}}} \left(\mathbf{I} - \frac{I_1}{3} \mathbf{C}^{-1} \right) + \frac{K}{\beta} (1 - J^\beta) \mathbf{C}^{-1} + 2k_1 (\mathbf{m}_1 \cdot \mathbf{m}_1 - 1) \mathbf{M}_1 \otimes \mathbf{M}_1 + 2k_2 (\mathbf{m}_2 \cdot \mathbf{m}_2 - 1) \mathbf{M}_2 \otimes \mathbf{M}_2 \quad (10)$$

where \mathbf{m}_1 and \mathbf{m}_2 are the current fiber directions given by:

$$\mathbf{m}_i = \mathbf{F} \mathbf{M}_i \quad (11)$$

For mathematical completion, all derivations involved in calculating the constituents of Eq. (10) are presented in Appendix A. Pre- and post-multiplying this result by the deformation gradient tensor converts the Second Piola-Kirchoff stress to Cauchy stress:

$$\boldsymbol{\sigma} = \frac{1}{J} \mathbf{F} \mathbf{S} \mathbf{F}^T \quad (12)$$

The conversion to Cauchy stress is necessary for Abaqus/Explicit VUMAT implementation.

Applying Eq. (12) to Eq. (10) gives:

$$\boldsymbol{\sigma} = \frac{G}{J} \left(\bar{\mathbf{b}} - \frac{\text{tr}(\bar{\mathbf{b}})}{3} \mathbf{I} \right) + \frac{K}{J^\beta} (1 - J^{-\beta}) \mathbf{I} + \frac{2k_1}{J} (\mathbf{m}_1 \cdot \mathbf{m}_1 - 1) \mathbf{m}_1 \otimes \mathbf{m}_1 + \frac{2k_2}{J} (\mathbf{m}_2 \cdot \mathbf{m}_2 - 1) \mathbf{m}_2 \otimes \mathbf{m}_2 \quad (13)$$

where $\bar{\mathbf{b}}$ is the modified left Cauchy strain tensor given by:

$$\bar{\mathbf{b}} = \mathbf{J}^{\frac{2}{3}} \mathbf{b} \quad (14)$$

$$\mathbf{b} = \mathbf{F} \mathbf{F}^T \quad (15)$$

The invariants of \mathbf{C} and \mathbf{b} are equivalent, which is useful for later calculations.

II.2.B DAMAGE MODEL

With the fundamental constitutive relation established, damage parameters are introduced to capture the degradation of the GRP. The four damage modes considered are matrix cracking due to shear and volume expansion, and fiber breakage in tension and compression. “Matrix damage” results in a loss of strength in all directions since the matrix permeates throughout the whole GRP. “Fiber damage” refers to fiber breakage, degrading the GRP properties only in the direction of the damaged fiber. The continuum nature of the damage model means all fiber damage contributions affect the whole GRP, not individual lamina. By modeling the GRP as a continuum, the separation of individual plies and ply bond strength cannot be captured, greatly complicating the representation of the delamination effect on the whole GRP. Barham et al. [12] accounted for delamination in their LLM by including separate lamina in their simulations. Scott et al. [16] introduced a delamination effect to a very closely related model by using a Tsai-Hill criterion to construct a lamina-level failure envelope, however, due to its perceived lack of physical meaning, it was not incorporated into the FCM. For these reasons, the decision was made to not include

delamination as a damage mode. Potential limitations resulting from this decision are addressed in the Results and Discussion chapter.

Matrix damage criteria R^{MS} and R^{ME} capture the degradation of the shear and bulk modulus of the GRP. The shear damage criterion is:

$$R^{MS} = \frac{\varepsilon_{eq}}{\varepsilon^{MS}} \quad (16)$$

where ε^{MS} is the critical matrix shear strain and ε_{eq} is the GRP equivalent strain given by:

$$\varepsilon_{eq} = \sqrt{\frac{3(\varepsilon_{xx}^2 + \varepsilon_{yy}^2 + \varepsilon_{zz}^2)}{2} + \frac{3(\gamma_{xy}^2 + \gamma_{yz}^2 + \gamma_{zx}^2)}{4}} \quad (17)$$

$$\varepsilon_{xx} = \frac{2}{3}\varepsilon_{xx} - \frac{1}{3}\varepsilon_{xx} - \frac{1}{3}\varepsilon_{xx} \quad (18)$$

$$\varepsilon_{yy} = \frac{2}{3}\varepsilon_{yy} - \frac{1}{3}\varepsilon_{xx} - \frac{1}{3}\varepsilon_{zz} \quad (19)$$

$$\varepsilon_{zz} = \frac{2}{3}\varepsilon_{zz} - \frac{1}{3}\varepsilon_{xx} - \frac{1}{3}\varepsilon_{yy} \quad (20)$$

$$\gamma_{ij} = 2\varepsilon_{ij} \quad (21)$$

The bulk damage criterion is defined as:

$$R^{ME} = \begin{cases} \alpha(1 - J)e^{\frac{J}{J_e^c}} & , J \leq 1 \\ \frac{J-1}{J_e^t-1} & , J > 1 \end{cases} \quad (22)$$

where α is an arbitrary empirical parameter, J_e^c is the critical matrix relative volume expansion strain under compression, and J_e^t is the critical matrix relative volume expansion strain in tension. α , J_e^c , and J_e^t are user-defined variables dictating the extent of bulk modulus degradation with respect to applied volumetric strain. Both α and J_e^c are featured in the sensitivity study in the Results and Discussion chapter. The top piecewise function describing compressive damage evolution captures the physical ‘‘bulking’’ effect when a material undergoes compressive impact loading, as well as the eventual modulus stiffness regained via a mechanism called lateral

confinement. Combined axial and lateral compressive stress can induce fracture in brittle materials through the “Wing Crack” mechanism. Lee and Ravichandran [17] subjected Columbia Resin (CR39) to dynamic loading conditions to observe “Wing Crack” propagation using photoelasticity. Horii and Nemat-Nasser [18], [19] proposed that Mode I crack propagation, “faulting”, is a result of unstable growth of tension cracks at certain points of interacting flaws. However, when the compressive volumetric strains of a material become large enough, lateral confinement begins to inhibit fault growth and effectively re-stiffens the material. A graph of this equation is depicted in Fig. 2. When $J = 1$ (no deformation), R^{ME} is zero, signifying no damage initiation. As J progresses towards 0 (compressive strains increase), R^{ME} asymptotically approaches α , which in the developed model is very close to zero. At this point, the material is physically so compressed that lateral confinement effects dominate, and further matrix cracking is inhibited. The peak of the graph occurs when the compressive strain equals J_e^c , after which the effects of lateral confinement begin to recover the bulk modulus of the material. Bulk degradation in tension follows a linear relationship in accordance with the criterion used by Barham et al. [12] and Scott et al. [16].

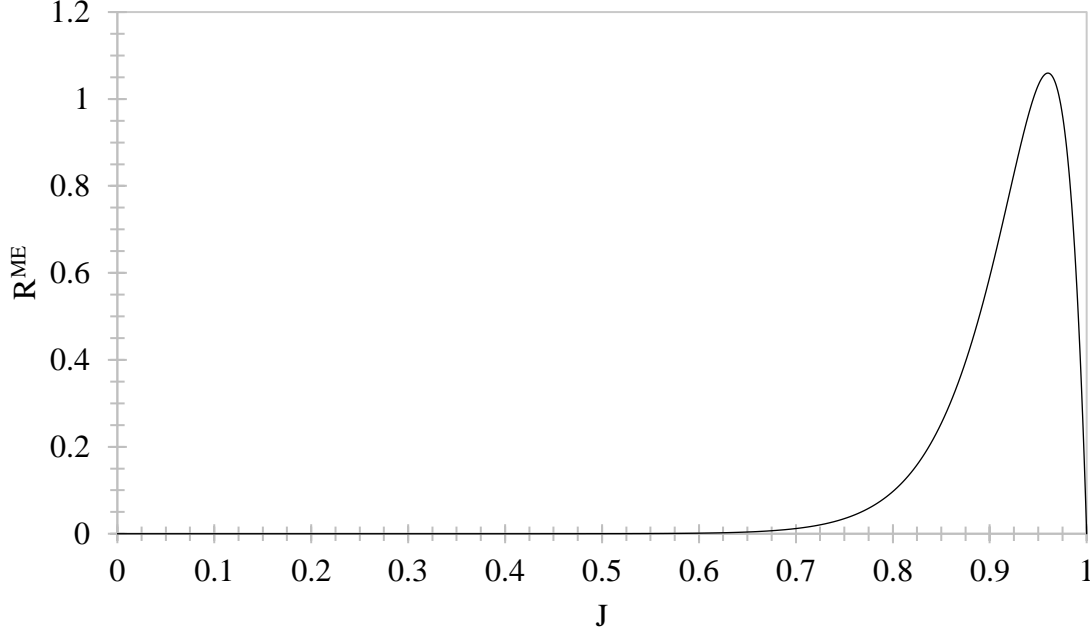


Figure 2. Compressive Bulk Damage Criterion Evolution, $\alpha=1 \times 10^{-9}$, $J_e^c=0.04$

The hyperelastic damage model used in this paper couples the contributions from bulk and shear damage terms into a generalized matrix damage criterion:

$$R^M = \sqrt{R^{ME^2} + R^{MS^2}} \quad (23)$$

For the matrix damage criteria to initiate damage, it must equal or exceed 1. When this is satisfied, the damage term evolves based on the exponent law:

$$d^M = \begin{cases} 0 & , R^M < 1 \\ 1 - \exp\left(\frac{1 - R^M}{\iota}\right) & , R^M \geq 1 \end{cases} \quad (24)$$

where ι is the matrix damage damping constant. By evolving damage in this manner, the isotropic GRP exhibits a linear elastic response until the onset of damage at $R^M = 1$ where moduli begin exponential decay. The unloading rate parameter ι is user-defined and featured in the model calibration sensitivity study. The bulk and shear moduli of the isotropic GRP are damage-adjusted according to Eqs. (25) and (26) respectively:

$$K = (1 - d^M)K^{\text{undamaged}} + d^M K^{\text{damaged}} \quad (25)$$

$$G = (1 - d^M)G^{\text{undamaged}} \quad (26)$$

where K^{damaged} is some arbitrarily-set value for the residual bulk modulus of a pulverized GRP. Physically, the K^{damaged} term is justified by the fact that shock waves can still propagate through a pulverized GRP when under compression. If under tension, however, the pulverized GRP disintegrates and K^{damaged} becomes zero.

Fiber damage criteria R^{fit} and R^{fic} represent fiber breakage in tension and compression respectively. These criteria apply for both fiber systems, denoted by $i = 1, 2$. Fibers in tension damage completely (no residual strength) once the critical tensile strain is exceeded. The fiber damage in tension criterion is:

$$R^{\text{fit}} = \frac{\varepsilon_i}{\varepsilon_i^{\text{fit}}} \quad (27)$$

where $\varepsilon_i^{\text{fit}}$ is the critical tensile strain in fiber 'i' and ε_i is the fiber strain:

$$\varepsilon_i = \mathbf{m}_i \cdot \mathbf{m}_i - 1 \quad (28)$$

When fibers in compression surpass their elastic compressive strain limit, either buckling or breakage ensues depending on if there is existing matrix or fiber damage. Buckling will only occur if both the matrix and fiber are undamaged. During buckling, the fiber and matrix de-bond, transferring a greater portion of the compressive load onto the matrix. However, since the buckled fiber has not failed, it still possesses a fraction of its original stiffness and contributes to the GRP strength in the fiber direction; Eq. (29) reflects this:

$$k_i^{\text{buckled}} = \eta k_i^{\text{undamaged}} \quad (29)$$

where η is the buckling constant. For the developed model, the fraction of residual strength the buckled fiber still possesses is arbitrarily chosen between 0 and 1. Future experimental efforts can hopefully determine a material-dependent value for this constant. Fiber breakage in compression occurs when the matrix surrounding the fiber is damaged. In this scenario, the surrounding matrix

provides less support, meaning the fibers shoulder a greater compressive load. Like in tension, when fiber breakage occurs, all fiber stiffness is lost. The compression damage fiber criterion is:

$$R^{fic} = \frac{\varepsilon_i}{\varepsilon^{fic}} \quad (30)$$

where ε^{fic} is the critical compressive strain in fiber 'i'. The damage term governing the contribution of fiber strengths to the FCM is summarized by Eq. (31):

$$d^f = \begin{cases} 1, & R^{fit} > 1 \\ 1 - \eta, & R^{fic} > 1 \text{ and } d^M = 0 \\ 1, & R^{fic} > 1 \text{ and } d^M > 0 \end{cases} \quad (31)$$

The fiber damage term and fiber stiffness are related by Eq. (32):

$$k_i = (1 - d_i^f)k_i^{\text{undamaged}} \quad (32)$$

Most fiber-reinforced composites exhibit strain rate-dependent behavior. Therefore, it is beneficial to introduce a strain rate adjustment to variables that affect damage criteria. In the implemented hyperelastic damage model, ε^{MS} and α are the two strain rate adjusted variables. A simple logarithmic expression governs any viscous effects associated with the aforementioned damage processes:

$$\text{var}_{\text{adjusted}} = \text{var} \left(1 + c_1 \ln \frac{\dot{\varepsilon}_{eq}}{\dot{\varepsilon}_{ref}} \right) \quad (33)$$

where 'var' is some selected variable, c_1 is some arbitrary weighting constant, $\dot{\varepsilon}_{eq}$ is the equivalent strain rate, and $\dot{\varepsilon}_{ref}$ is the reference strain rate which is assumed to be unity. The c_1 values corresponding to the strain rate dependent parameters were calibrated and included in the sensitivity study.

II.3 VUMAT CONSTRUCTION

An Abaqus/Explicit VUMAT is a useful tool for researchers to define the mechanical constitutive response of a material that does not appear in Abaqus' existing material properties

tool. The code read by Abaqus to implement the VUMAT is called the user subroutine. As noted by Hohenberger et al. [20], VUMATs have been used by many researchers but complete subroutine codes are rarely published and are often of poor quality. Abaqus documentation [21] provides a subroutine for an elastic-plastic material model with kinematic hardening, though it gives vague instruction on the nuances, techniques, and syntax involved in its construction. The VUMAT sample provided in Bergström's textbook [22] is obsolete and partially complete. Conversely, Hohenberger et al. published a complete, validated subroutine with a detailed explanation of code features; this resource was pivotal to the completion of this thesis. To help expand the VUMAT resources available for researchers and further efforts in the computational modeling field, this section comprehensively details the VUMAT subroutine developed for the FCM. Furthermore, a working copy of the subroutine is available in Appendix B, written in Fortran77.

II.3.A INITIALIZATION

Instructions on how to link Abaqus with the appropriate language compiler (Fortran77 or C) and a source code editor like Microsoft Visual Studio are outside the scope of this paper, however, literature exists to help with this procedure [23], [24]. If properly compiled, the Abaqus error that returns “problem during compilation” typically hints toward incorrect syntax in the subroutine code. Abaqus documentation [21] provides guidelines for the default variables contained in the subroutine and their meanings, tensor component indexing (Tables 2 and 3), conventions Abaqus follows in calculations, and an example subroutine code with accompanying theory.

Table 2. Symmetric tensor
Abaqus indexing

Index	2D case	3D case
1	σ_{11}	σ_{11}
2	σ_{22}	σ_{22}
3	σ_{33}	σ_{33}
4	σ_{12}	σ_{12}
5		σ_{23}
6		σ_{31}

Table 3. Asymmetric tensor
Abaqus indexing

Index	2D case	3D case
1	F_{11}	F_{11}
2	F_{22}	F_{22}
3	F_{33}	F_{33}
4	F_{12}	F_{12}
5	F_{21}	F_{23}
6		F_{31}
7		F_{21}
8		F_{32}
9		F_{13}

Before any user-defined input into the subroutine, Abaqus requires the subroutine to be initialized with a sequence that includes all default Abaqus-defined variables. Referring to the code in Appendix B, the sequence encompasses the lines starting and ending with:

```

SUBROUTINE VUMAT (
.
.
.
CHARACTER*80 cmname

```

The Abaqus-defined variables are named and assigned a dimension for storage throughout subroutine calls. Following this, the numerical constants (name and value), local variables, and material properties are defined. Example code appears below. The placement of the ‘!’ character (any special character or number can be used) is important—the continuation of a previous line is marked by any special character/number in the 6th character space followed by the continued “calculation” code in the 7th character space onwards (up to a maximum of 72 characters):

```

REAL*8 zero, one, two, three, four, ten, half, third, twothirds,
! deetee
PARAMETER(zero = 0.d0, one = 1.d0, two = 2.d0, three = 3.d0,
! four = 4.d0, ten = 10.d0, half = 0.5d0, third = 1.d0/3.d0,
! twothirds = 2.d0/3.d0, deetee = 4.d0*(10.d0**(-10.d0))

```

Local variables encompass all variables that appear in subroutine equations, including names assigned to material properties. They are defined the same way as numerals are named.

Abaqus-defined properties are excluded from this block. Example code is:

```
REAL*8 G, Kay, beta, k1, k2, M11, M12, M13, M21, M22, M23,  
!      clems, Je, iota, ems, tcrit, ccrit, C11, C22, C33
```

Material property names and positions are assigned using the `props()` function. The number contained in `props()` corresponds with the placeholder in Abaqus' user material properties window (Fig. 3). Example code and the corresponding properties window are pictured:

```
G      = props(1)  
Kay    = props(2)  
beta  = props(3)
```

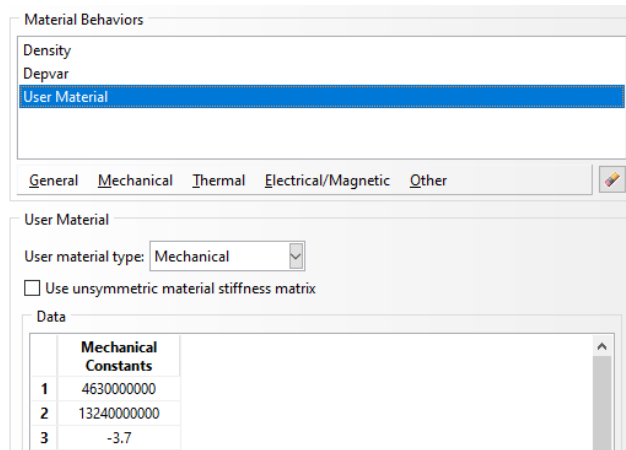


Figure 3. Abaqus user-material properties window displaying property assignments

In the final step before user coding commences, a linear elastic initialization is required by Abaqus. The purpose of this step is to establish a stable time increment to help Abaqus advance the solution. The first call to the subroutine assigns a linear elastic approximation for the material, requiring shear and bulk modulus properties to be defined. Abaqus-defined variables `totalTime`, `strainInc`, `stressOld`, and `stressNew` appear in this step. The full elastic initialization code is in Appendix B; a compact version is below:

```

IF (totalTime.EQ.0.0) THEN
DO i = 1,nblock
    trace = strainInc(i,1) + strainInc(i,2) +
!     strainInc(i,3)
    stressNew(i,1) = stressOld(i,1) +
!     two * G * strainInc(i,1) +
!     (Kay - (twothirds * G)) * trace
.
.
.
    stressNew(i,6) = stressOld(i,6) +
!     two * G * strainInc(i,6)
END DO
RETURN
END IF

```

In this sequence, `DO i = 1, nblock` commands Abaqus to run the loop for all `nblock` material points (elements). The indexing in `stressNew(i,1)` instructs Abaqus to search/update the value of component ‘1’ at element number ‘i’ (in this case, updating σ_{11}).

II.3.B SUBROUTINE BODY

The bulk of the subroutine, the user coding, is responsible for all calculations involved in the hyperelastic damage model. Local variables and Abaqus-defined variables are used to produce the stress-updating constitutive equation. Abaqus defines the constitutive model in a corotational coordinate system where the basis system rotates with the material. Therefore, it is mathematically useful to decompose the deformation gradient tensor into its constituents:

$$\mathbf{F} = \mathbf{R}\mathbf{U} = \mathbf{V}\mathbf{R} \quad (34)$$

where \mathbf{R} is the orthogonal rotation tensor, \mathbf{U} is the symmetric right stretch tensor, and \mathbf{V} is the symmetric left stretch tensor. Strictly, \mathbf{U} and \mathbf{V} are different and related by Eq. (35):

$$\mathbf{V} = \mathbf{R}\mathbf{U}\mathbf{R}^T \quad (35)$$

yet since rotation is automatically accounted for and they possess equivalent principal stretches, for this paper’s purposes they are the same. From this point onwards, stretch tensors are denoted

by \mathbf{U} to match the Abaqus convention. The corotational system essentially reduces \mathbf{F} to \mathbf{U} , transforming calculations originally in terms of \mathbf{F} :

$$\mathbf{J} = \det(\mathbf{F}) = \det(\mathbf{R}\mathbf{U}) = \det(\mathbf{U}) \quad (36)$$

$$\mathbf{b} = \mathbf{F}\mathbf{F}^T = \mathbf{R}\mathbf{U}^2\mathbf{R}^T = \mathbf{U}^2 \quad (37)$$

Combining Eq. (14) with Eq. (37) relates the stretch tensor to the modified left Cauchy strain tensor:

$$\bar{\mathbf{b}} = \mathbf{J}^{-\frac{2}{3}} \mathbf{U}^2 \quad (38)$$

the square root of which is the modified stretch tensor:

$$\bar{\mathbf{U}} = \mathbf{J}^{-\frac{1}{3}} \mathbf{U} \quad (39)$$

Applying Eqs. (36), (38), and (39) to Eq. (13) yield the ‘subroutine form’ of the corotational Cauchy stress, taking advantage of the Abaqus-defined stretchNew parameter:

$$\boldsymbol{\sigma}_{\text{co}} = \frac{G}{\det(\mathbf{U})} \left(\bar{\mathbf{U}}^2 - \frac{\text{tr}(\bar{\mathbf{U}}^2)}{3} \mathbf{I} \right) + \frac{K}{\det(\mathbf{U})\beta} \left(1 - \frac{\det(\mathbf{U})}{\beta} \right) \mathbf{I} + \frac{2k_1}{\det(\mathbf{U})} (\mathbf{m}_1 \cdot \mathbf{m}_1 - 1) \mathbf{m}_1 \otimes \mathbf{m}_1 + \frac{2k_2}{\det(\mathbf{U})} (\mathbf{m}_2 \cdot \mathbf{m}_2 - 1) \mathbf{m}_2 \otimes \mathbf{m}_2 \quad (40)$$

A snapshot of the code that calculates the isochoric and volumetric terms is presented below:

```

DO k = 1,nblock
C
C      CALCULATE J = |F| = |U|
C      -----
J =      stretchNew(k,1) *
!      ( stretchNew(k,2) * stretchNew(k,3)   -
!      stretchNew(k,5) * stretchNew(k,5) ) +
!      stretchNew(k,4) *
!      ( stretchNew(k,5) * stretchNew(k,6)   -
!      stretchNew(k,3) * stretchNew(k,4) ) +
!      stretchNew(k,6) *
!      ( stretchNew(k,4) * stretchNew(k,5)   -
!      stretchNew(k,2) * stretchNew(k,6) )
.
.
.
C
C      VOLUMETRIC CAUCHY STRESS TERM
C      -----
      fac2 = (Kay / (J * beta)) * (one - (one / (J**beta)))

```

Hand calculations and accompanying code for the undamaged anisotropic term of one fiber direction are presented below. The full outer product matrix is available in Appendix D. Outer product terms are only applied to the principal fiber directions, so only the diagonal terms in the matrix are accounted for:

$$\begin{aligned}
\mathbf{m}_1 \cdot \mathbf{m}_1 &= \mathbf{M}_1 \cdot \mathbf{C} \mathbf{M}_1 = \begin{bmatrix} M11 \\ M12 \\ M13 \end{bmatrix} \cdot \begin{bmatrix} Cxx & Cxy & Cxz \\ Cxy & Cyy & Cyz \\ Cxz & Cyz & Czz \end{bmatrix} \begin{bmatrix} M11 \\ M12 \\ M13 \end{bmatrix} \\
&= \begin{bmatrix} M11 \\ M12 \\ M13 \end{bmatrix} \cdot \begin{bmatrix} CxxM11 + CxyM12 + CxzM13 \\ CxyM11 + CyyM12 + CyzM13 \\ CxzM11 + CyzM12 + CzzM13 \end{bmatrix} \\
&= M11(CxxM11 + CxyM12 + CxzM13) + M12(CxyM11 + CyyM12 + \\
&\quad CyzM13) + M13(CxzM11 + CyzM12 + CzzM13) \tag{41}
\end{aligned}$$

$$\mathbf{m}_1 \otimes \mathbf{m}_1 = \begin{bmatrix} U1M11 + U4M12 + U6M13 \\ U4M11 + U2M12 + U5M13 \\ U6M11 + U5M12 + U3M13 \end{bmatrix} \otimes \begin{bmatrix} U1M11 + U4M12 + U6M13 \\ U4M11 + U2M12 + U5M13 \\ U6M11 + U5M12 + U3M13 \end{bmatrix} \tag{42}$$

```

m1dpm1 = M11 * (M11 * Cxx + M12 * Cxy + M13 * Cxz) +
!       M12 * (M11 * Cxy + M12 * Cyy + M13 * Cyz) +
!       M13 * (M11 * Cxz + M12 * Cyz + M13 * Czz)
mloutxx = (stretchNew(k,1) * M11 + stretchNew(k,4) * M12 +
!         stretchNew(k,6) * M13)**two
mloutyy = (stretchNew(k,4) * M11 + stretchNew(k,2) * M12 +
!         stretchNew(k,5) * M13)**two
mloutzz = (stretchNew(k,6) * M11 + stretchNew(k,5) * M12 +
!         stretchNew(k,3) * M13)**two

```

Introducing damage into the FCM is achieved by first coding damage criteria. The matrix damage criterion that calculates R^{MS} involves Eqs. (20) – (24) and demands a choice on whether to use nominal or logarithmic strain for the stretch to strain conversion. Abaqus does not directly define a strain variable, so stretch must be utilized in equations that call for strain. For three-dimensional simplicity, nominal strain is used:

$$\boldsymbol{\varepsilon} = \mathbf{U} - \mathbf{I} \quad (43)$$

Unstrained materials have axial stretches of 1 and shear stretches of zero, therefore the identity matrix subtraction fulfils the role of neutralizing the starting axial stretch value. The code block containing equivalent strain calculations for the R^{MS} numerator is outlined below:

```

exx = twothirds * (stretchNew(k,1) - one) -
!   third * (stretchNew(k,2) - one) -
!   third * (stretchNew(k,3) - one)
.
.
.
exz = two * stretchNew(k,6)
epeqold = stateOld(k,1)
epeq = twothirds * sqrt((three / two) * (exx**two + eyy**two +
!   ezz**two) + (three / four) * (exy**two + eyz**two +
!   exz**two))
stateNew(k,1) = epeq

```

This code block is the first instance of user-defined state variable usage. State variables store data for each material point, can evolve throughout the current increment's calculations, and can be called back for calculations during the next increment. The change in the equivalent strain $epeq$

used in the strain rate calculation takes advantage of this. Introducing strain rate adjustments to ϵ^{MS} (for the R^{MS} criterion) and α (for the R^{ME} criterion) requires a definition of the strain rate:

$$\dot{\epsilon}_{\text{eq}} = \frac{\Delta \epsilon_{\text{eq}}}{\Delta t} \quad (44)$$

Using state variables, finding the difference between the equivalent strain of the previous and current increment becomes trivial:

$$\text{strrate} = (\text{epeq} - \text{epeqold}) / \text{deetee}$$

A small note to the reader with regards to user-defined state variable usage: there is no limit to the number of user-defined state variables a subroutine can contain, as long as that number is defined in the ‘Depvar’ window of the Abaqus material properties interface. Both `stateOld` and `stateNew` are required for variables the user wishes to evolve throughout each iteration. If the user simply requests Abaqus to output some state variable value and monitor its development throughout the analysis, only `stateNew` is needed. User-defined state variables are plottable in Abaqus as a field output and can be contoured in the output display.

An assumption made for the FCM is that damage growth will not occur at quasi-static strain rates $\dot{\epsilon}_{\text{eq}} < 1$. To achieve this, user-defined state variables are used to call back previous-iteration values of R^{ME} and R^{MS} for use in a conditional if-else statement. If the strain rate is quasi-static, the R^{ME} and R^{MS} values for the current iteration are set to their prior iteration values. If the strain rate exceeds 1, damage growth is permitted and calculated according to Eqs. (16), (22), (23), (33), and (44). The code block below reflects this:

```

Rmsold = stateOld(k,2)
Rmeold = stateOld(k,3)
IF (strrate.LT.one) THEN
  Rms = Rmsold
  Rme = Rmeold
  lograte = zero
  emsadj = ems
  alphaadj = alpha
ELSE
  lograte = log(abs(strrate))
  emsadj = ems * (one + clems * lograte)
  Rms = epeq / emsadj
  IF (J.GT.one) THEN
    Rme = (J - one) / (Je - one)
  ELSE
    alphaadj = alpha * (one + clalpha * lograte)
    Rme = alphaadj * (one - J) * exp(J / Je)
  END IF
END IF
stateNew(k,2) = Rms
stateNew(k,3) = Rme
Rm = sqrt((Rms**two) + (Rme**two))

```

With the matrix damage criterion established, the subroutine checks if the conditions to initiate matrix damage are met (see Eq. (24)) and sets the matrix damage term accordingly:

```

IF (Rm.LT.one) THEN
  matdamCurrent = zero
ELSE
  matdamCurrent = one - exp((one - Rm) / iota)
END IF

```

To capture the physical damage response sufficiently, further assumptions must be made, expanding upon the simple relation between d^M and R^M in Eq. (24). The FCM makes the critical assumption that the GRP cannot ‘heal’ itself once damage initiates. No mention of this damage behavior appears in the LLM model by Barham et al. [12] or in the hyperelastic damage model developed by Scott et al. [16]. To ensure that the damage parameter can only accumulate irrespective of fluctuations in R^M , user-defined state variables are used to compare the matrix damage calculated for the current iteration and the matrix damage term stored from the previous

iteration. The greater damage value of the two is used for the updated stress calculations and re-saved in the “matrix damage” state variable for use for the next increment. This methodology is captured in this code block:

```
matdamOld = stateOld(k,4)
IF (matdamCurrent.GE.matdamOld) THEN
    matdamNew = matdamCurrent
ELSE
    matdamNew = matdamOld
END IF
stateNew(k,4) = matdamNew
```

It is critical that the matrix damage term is calculated before the fiber damage terms since fiber damage in compression is dependent on matrix damage history. Fiber damage criteria R^{fit} and R^{fic} depend on fiber strain dot products as well as critical tensile (t_{crit}) and compressive (c_{crit}) fiber strain properties defined in the Abaqus user-material properties window:

```
Rfit1 = (m1dpm1 - one) / tcrit
Rfit2 = (m2dpm2 - one) / tcrit
Rfic1 = (m1dpm1 - one) / ccrit
Rfic2 = (m2dpm2 - one) / ccrit
```

The piecewise conditions in Eq. (31) are captured in the code below (for brevity, only one fiber direction is included):

```
IF (Rfit1.GT.one) THEN
    fibdam1 = one
ELSE IF (Rfic1.GT.one .AND. matdamNew.EQ.zero) THEN
    fibdam1 = one - eta
ELSE IF (Rfic1.GT.one .AND. matdamNew.GT.zero) THEN
    fibdam1 = one
ELSE
    fibdam1 = zero
END IF
```

Like the matrix damage evolution, user-defined state variables are implemented to ensure accurate damage accumulation for fiber damage, detailed below:

```

fibdam1Old = stateOld(k,5)
fibdam2Old = stateOld(k,6)
IF (fibdam1.GE.fibdam1Old) THEN
    fibdam1New = fibdam1
ELSE
    fibdam1New = fibdam1Old
END IF
IF (fibdam2.GE.fibdam2Old) THEN
    fibdam2New = fibdam2
ELSE
    fibdam2New = fibdam2Old
END IF
stateNew(k,5) = fibdam1New
stateNew(k,6) = fibdam2New

```

Stress-updating equations are the final mandatory step of all VUMAT subroutine analyses.

The subroutine developed for the FCM updates stress according to Hooke's Law in Eq. (1) when all damage terms are zero. When any matrix or fiber damage initiates, the stress-updating equations are changed to reflect the hyperelastic FCM. The full code block is below:

```

Totaldam = matdamNew + fibdam1New + fibdam2New
IF (Totaldam.EQ.zero) THEN
    stressNew(k,1) = C11 * (stretchNew(k,1) - one) +
!   C12 * (stretchNew(k,2) - one) + C13 * (stretchNew(k,3) -
!   one)
    stressNew(k,2) = C12 * (stretchNew(k,1) - one) +
!   C22 * (stretchNew(k,2) - one) + C23 * (stretchNew(k,3) -
!   one)
    stressNew(k,3) = C13 * (stretchNew(k,1) - one) +
!   C23 * (stretchNew(k,2) - one) + C33 * (stretchNew(k,3) -
!   one)
    stressNew(k,4) = C66 * two * stretchNew(k,4)
    stressNew(k,5) = C55 * two * stretchNew(k,5)
    stressNew(k,6) = C44 * two * stretchNew(k,6)
ELSE
    IF (matdamNew.EQ.one .AND. J.GE.one) THEN
        Kayd = zero
    ELSE
        Kayd = Kay / ten
    END IF
    Kdterm = (Kayd / (J * beta)) * (one - (one / (J**beta)))
    stressNew(k,1) = (one - matdamNew) * facxx +
!   (one - matdamNew) * fac2 + matdamNew * Kdterm + (one -
!   fibdam1New) * fac3xx1 + (one - fibdam2New) * fac3xx2
    stressNew(k,2) = (one - matdamNew) * facyy +
!   (one - matdamNew) * fac2 + matdamNew * Kdterm + (one -
!   fibdam1New) * fac3yy1 + (one - fibdam2New) * fac3yy2
    stressNew(k,3) = (one - matdamNew) * faczz +
!   (one - matdamNew) * fac2 + matdamNew * Kdterm + (one -
!   fibdam1New) * fac3zz1 + (one - fibdam2New) * fac3zz2
    stressNew(k,4) = (one - matdamNew) * facxy
    stressNew(k,5) = (one - matdamNew) * facyz
    stressNew(k,6) = (one - matdamNew) * facxz
END IF

```

Though optional when developing a VUMAT, a specific internal energy updating sequence is included at the end of the FCM subroutine. This is solely for a better physical representation of the FCM. The equation for specific internal energy was acquired from Abaqus documentation:

$$W = \frac{1}{2} \left((\sigma_{xx}^{old} + \sigma_{xx}^{new}) \Delta \varepsilon_{xx} + (\sigma_{yy}^{old} + \sigma_{yy}^{new}) \Delta \varepsilon_{yy} + (\sigma_{zz}^{old} + \sigma_{zz}^{new}) \Delta \varepsilon_{zz} + 2 \left((\sigma_{xy}^{old} + \sigma_{xy}^{new}) \Delta \varepsilon_{xy} + (\sigma_{yz}^{old} + \sigma_{yz}^{new}) \Delta \varepsilon_{yz} + (\sigma_{xz}^{old} + \sigma_{xz}^{new}) \Delta \varepsilon_{xz} \right) \right) \quad (45)$$

$$IE^{new} = IE^{old} + \frac{W}{\rho} \quad (46)$$

Its corresponding code is below:

```
uliniso = half*((stressOld(k,1)+stressNew(k,1))*strainInc(k,1)+
! (stressOld(k,2)+stressNew(k,2))*strainInc(k,2) +
! (stressOld(k,3)+stressNew(k,3))*strainInc(k,3) +
! two * ( (stressOld(k,4) + stressNew(k,4))*
! strainInc(k,4) + (stressOld(k,5) + stressNew(k,5))*
! strainInc(k,5) + (stressOld(k,6) + stressNew(k,6))*
! strainInc(k,6) ) )
C
enerInternNew(k) = enerInternOld(k) + uliniso / density(k)
```

In addition to the complete FCM VUMAT code in Appendix B, a complete flow chart of the code logic is available in Appendix C.

CHAPTER III

EXPERIMENTAL BENCHMARKS AND SIMULATIONS

III.1 PLATE IMPACT TEST

The plate impact shock compression experiments conducted by Tsai et al. [11] used an 82.5 mm single-stage gas gun housed at the Case Western Reserve University to fire a flyer plate at a GRP target, creating a normal oblique impact. A schematic of the setup is shown in Fig. 4. The experimental details are given by Tsai et al. No attempt is made to repeat the details in the current computational modeling work.

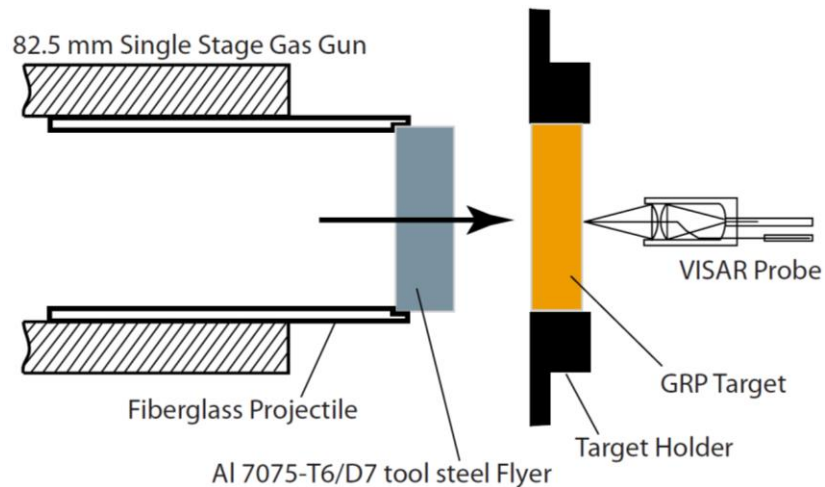


Figure 4. Plate impact test experimental schematic [11]

The flyer plates for all test shots were either Al 7075-T6 Aluminum or D7 Tool Steel of 75 mm diameter. It should be noted that the flyer plates remain elastic at all reported velocities and therefore, the alloy compositions of either steel or aluminum influence the VISAR signals (the measured time histories of the particle velocity). No exact flyer plate thickness was specified, rather they were sufficiently thick so that the release wave from the back free surface of the flyer

arrived at the impact surface much later than the GRP release wave. The GRP samples were made of woven 0°/90° S2 glass fiber bundles in a Cycom 4102 polyester structural resin. Each lamina measured 54 mm width by 54 mm height by 0.68 mm thickness. The total thickness of the GRP laminates varied between 2.94 mm and 20.2 mm, to develop a broader understanding of compressive shock wave evolution. On each GRP target, the rear surface was thinly (60-125 nm) coated with aluminum to facilitate the use of the VISAR probe. VISAR measurements were conducted directly onto the aluminum coating.

III.2 PLATE IMPACT BENCHMARK DATA

For FCM model calibration, the two tests of focus were LT30 and LT48. Both used a 6.8 mm thick GRP but varied in flyer material and flyer velocity and therefore possess distinctly different particle velocity profiles. Table 4 summarizes the results of both tests using data provided by Tsai et al., while Fig. 5 depicts the VISAR data for the free surface particle velocity profiles of high (LT48), intermediate (LT31), and low-velocity (LT30) tests. The tabulated particle velocity value for LT48 did not match the VISAR data, so the VISAR-measured particle velocity estimate is parenthesized.

Table 4. Plate impact experimental results [11]

Shot No.	Flyer Material	Impact Velocity (m/s)	GRP thickness (mm)	Free surface particle velocity (m/s)
LT30	Al 7075-T6	111.69	6.75	171.12
LT31	Al 7075-T6	312.7	6.55	456.26
LT48	D7 Tool Steel	417.96	6.76	807.16 (~780)

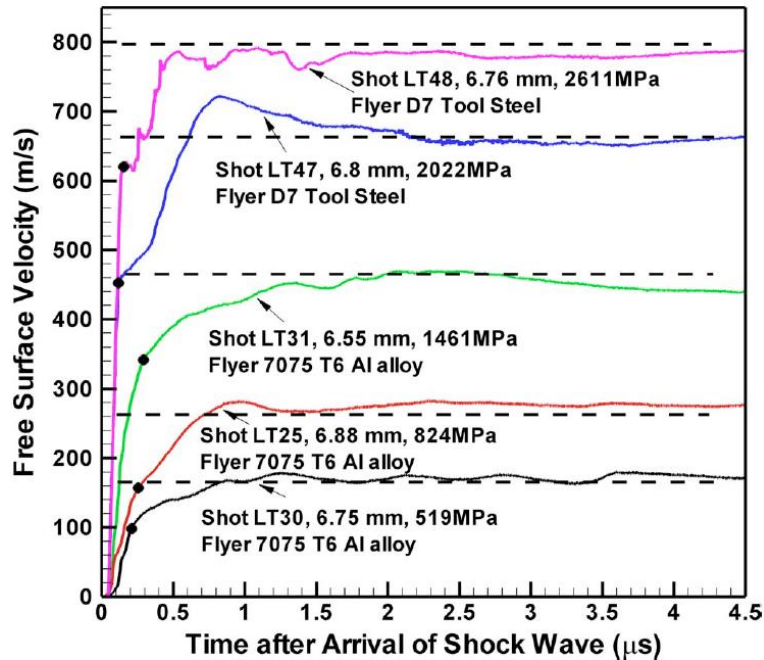


Figure 5. Selected experimental free surface particle velocity VISAR data [11]

The features of the velocity profiles pertinent to the FCM calibration were the rise time, linear-nonlinear transition velocity, velocity evolution after damage initiation, the peak velocity amplitude, and the late-time oscillations. The black markers added to each profile in Fig. 5 signify the transition point between the linear and nonlinear velocity profile response. Tsai et al. [11] noted that these markers did not coincide with the HEL of the composite, as it would with metals and crystalline ceramics. Instead, their position was likely caused by the viscoelastic behavior of the GRP matrix layers. For experiments with impact stress less than 1.5 GPa the shock front was not observed, but in experiments with impact stress greater than 2 GPa the shock front was clearly evident. Barker et al. [25] proposed the idea of a “critical amplitude” which represents the shock stress above which a clear shock front develops. For the GRP used by Tsai et al., the “critical amplitude” was estimated to lie between 1.5 GPa and 2 GPa. Furthermore, the slope of the shock front was observed to increase with increasing impact stress.

Tsai and Prakash [26] observed late-time oscillations in the shock response of elastic-viscoelastic bilaminates, deducing the oscillation frequency was tied to the density of the laminate interfaces. Though present in test LT30, late-time oscillations in this GRP were generally absent. Tsai et al. [11] understood this to be due to the impedance mismatch between the S2 glass layers and the matrix layers causing complex wave interference patterns. No conjecture was made on why LT30 produced such oscillations.

In addition to their analysis of free surface particle velocity profiles, Tsai et al. [11] established a Hugoniot curve by calculating Hugoniot stress and Hugoniot strain. The Rankine-Hugoniot relationships for stress and strain are:

$$\sigma_H = \rho_0 U_s u_p \quad (47)$$

$$\epsilon_H = \frac{u_p}{U_s} \quad (48)$$

where ρ_0 is the material initial density, U_s is the shock velocity calculated from some equation of state, and u_p is the particle velocity. A linear equation of state satisfies most materials and is used by Tsai et al. to govern the relationship between shock velocity and particle velocity:

$$U_s = C_0 + S u_p \quad (49)$$

where C_0 is the sound velocity in the material at zero pressure and ‘S’ is an empirical parameter. Using Eqs. (47) – (49) and an experimentally-determined value for ‘S’, Tsai et al. deduced shock velocities, Hugoniot stress, and Hugoniot strain values for all plate impact tests. Table 5 summarizes these results for LT30 and LT48:

Table 5. Shock velocity, Hugoniot Stress, and Hugoniot strain data for the GRP [11]

Shot No.	Free surface particle velocity (m/s)	Calculated Shock Velocity (km/s)	Hugoniot Stress (GPa)	Hugoniot Strain (%)
LT30	171.12	3.285	0.551	2.260
LT31	312.7	3.509	1.568	6.501
LT48	679.69	3.453	2.308	9.802

Discrepancies appear in the tabulated free surface particle velocity values for tests LT47, LT48, and LT49 throughout the Tsai et al. paper, so for calibration purposes, only the experimental particle velocity profile was considered.

III.3 BALLISTIC PENETRATION TESTS

The ballistic penetration tests conducted by Prifti et al. [14] subjected monolithic GRP laminates to a single fragment impact. Experimental parameters varied in their testing were fragment mass, strike velocity, and GRP thickness. No fragment geometry was provided, so they were assumed cylindrical. Only one sized FSP was used in the simulations as the simulation's primary purpose was to apply and validate the implementation of the FCM as a hyperelastic CDM model. The selected FSP was 207 grain (13.4134 grams), 12.7 mm caliber, and made of D7 Tool Steel. Calculating the thickness of the fragment was achieved by finding the necessary fragment volume given its material density and mass (Eq. (50)), then applying a geometry equation (Eq. (51)) given its caliber. Applying Eqs. (50) and (51) yielded an FSP thickness of 13.489 mm.

$$V = \frac{m}{\rho} \quad (50)$$

$$t = \frac{V}{\pi r^2} \quad (51)$$

The fragment was launched at 0-degree oblique impact out of 203.2 mm long rifled barrels with a 1/15 twist. Projectile yaw was observed to not exceed 1.5° for any test shot. These details are given for the sake of completion; the firing mechanism of the FSP was not present in the model simulations. Fragment velocities ranged from 359.664 m/s to 1252.423 m/s, purposefully below the limit velocity of the GRP target such that every test produced partial penetration.

All but one GRP target had an impact surface area of 504 mm x 504 mm, with the exception being one test run with a 584.2 mm x 584.2 mm area. The GRP laminate thicknesses ranged from

41.402 mm to 74.93 mm. The GRP target was supported by a rigid steel frame with a 457.2 mm diameter circular opening. The GRP was centered on the circular opening and clamped to the steel frame at all four corners of the GRP. A 457.2 mm x 457.2 mm x 0.5 mm 2024-T6 Aluminum plate was sandwiched between the back face of the GRP and the front face of the steel frame to measure the maximum transient displacement of the GRP back surface.

In addition to the tests performed by Prifti et al. [14] to gather DOP and rear surface displacement data, Rajendran et al. [15] conducted tests to produce stress profiles for low-velocity impacts at different through-thickness depths. The GRP used was dimensionally identical to the Prifti et al. experiments, while the FSP used was 20 mm caliber with 7.5 mm thickness. The FSP velocity was 246 m/s. The relevant test run sandwiched two 6.35 mm x 6.35 mm manganin strain gauges between GRP laminates 9.88 mm (Plate 1), 9.42 mm (Plate 2), and 25.4 mm (Plate 3) thick, illustrated in Fig. 6.

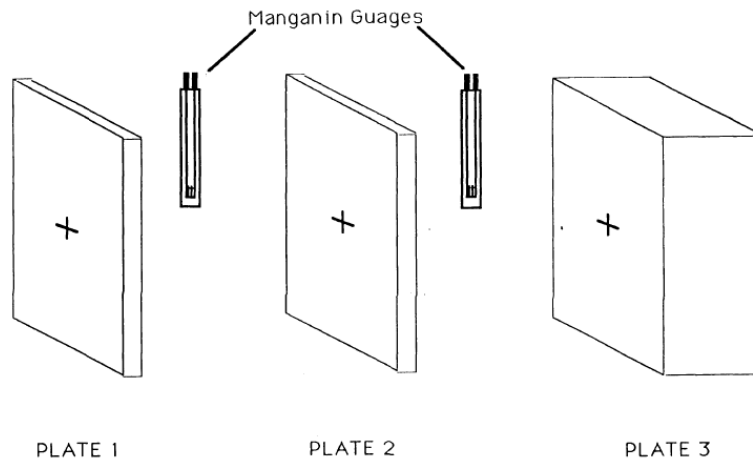


Figure 6. Ballistic penetration stress measurement setup [15]

III.4 BALLISTIC PENETRATION BENCHMARK RESULTS

Prifti et al. [14] utilized Computed tomography (CT) inspection post-impact to analyze the damage extent within the GRP. Scans were taken of the impact surface plane of the GRP target in uniform 2 mm slices along the thickness direction. DOP data was obtained using the expression:

$$DOP = \frac{1}{2}(t - 2n) + 2m + 1 \quad (52)$$

where ‘t’ is the total GRP laminate thickness in mm, ‘n’ is the total number of imaging slices, and ‘m’ is the slice number in which penetration reached its maximum.

For this thesis, only tests run on GRP laminate thicknesses of 44mm were used for the comparison to the FCM model. Table 6 and Fig. 7 summarize the experimental DOP and maximum rear surface displacement findings:

Table 6. DOP and related data for 44 mm thick GRP targets [14]

Test Number	Fragment Mass (grams)	Strike Velocity (m/s)	Depth of Penetration (mm)	Rear Surface Max. Displacement (mm)
T44-93-1	13.4	582.8	8.6	4.8
T44-93-2	13.4	617.2	8.6	4.0
T44-93-3	13.4	921.1	24.6	8.7
T44-93-4	13.4	897.9	26.6	9.5
T44-93-5	13.4	1200.3	36.6	16.7
T44-93-6	13.4	1206.4	38.6	17.5

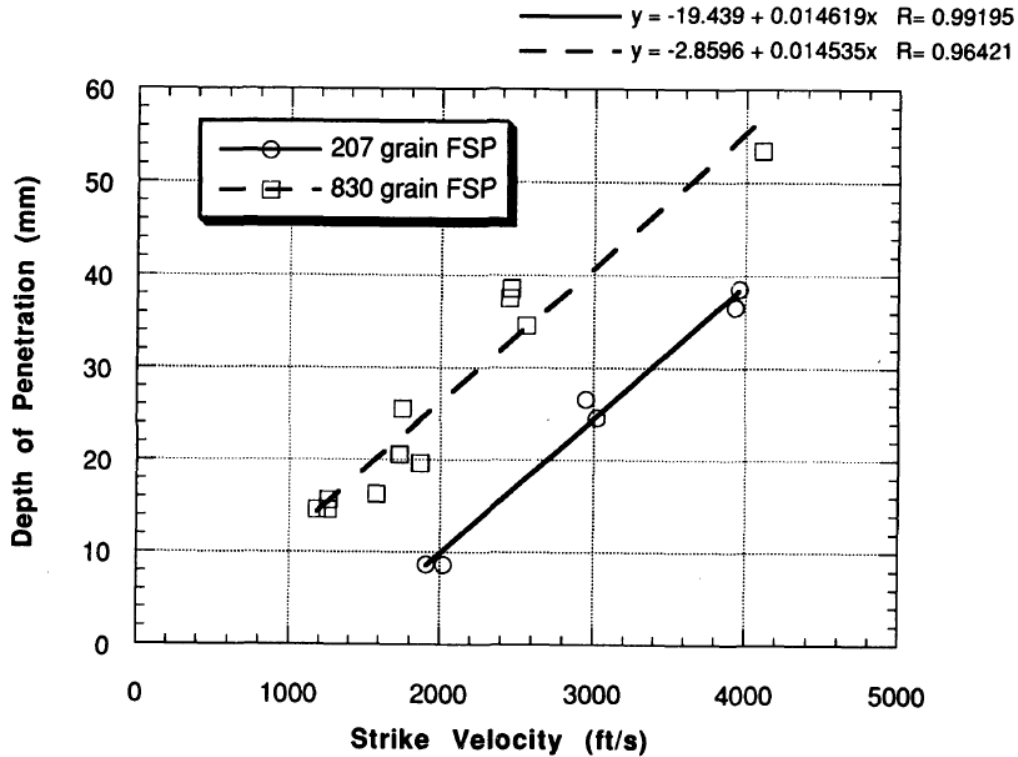


Figure 7. Effect of fragment mass and strike velocity on DOP [14]

Stress profiles were obtained by Rajendran et al. [15] at approximately 9 mm (Top Gauge) and 20 mm (Bottom Gauge) depths and are depicted in Fig. 8.

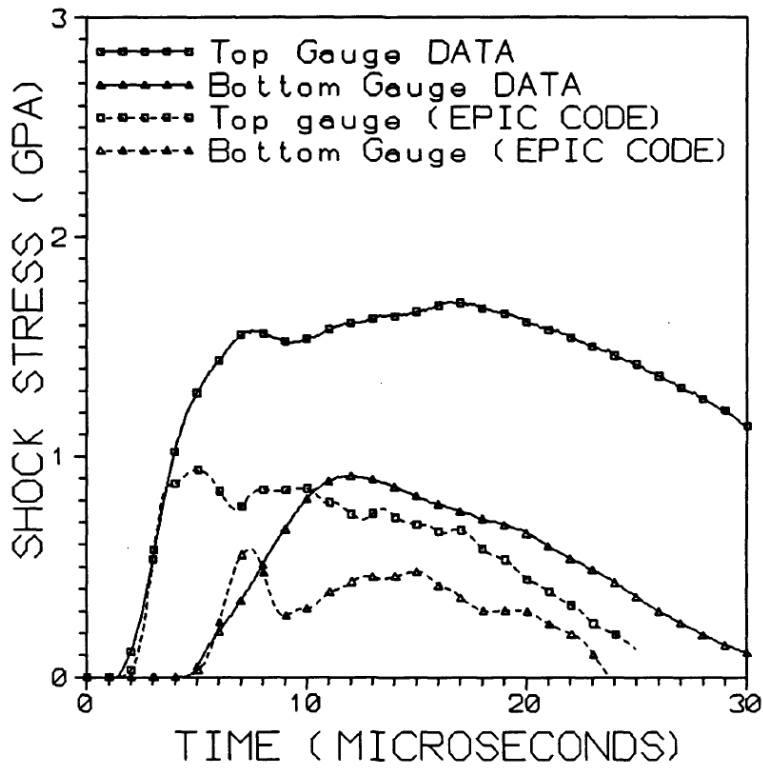


Figure 8. Stress profiles at 9 mm and 20 mm depths for a 246 m/s 20 mm caliber FSP impact

CHAPTER IV

ABAQUS SIMULATIONS

Two simulations were developed in Abaqus for this paper: the plate impact test and the ballistic penetration test. For the sake of completion, this section details the model features, conditions, and parameters used to obtain the results presented in the next chapter.

IV.1 PLATE IMPACT SIMULATION

The FCM model assumed the GRP as a continuum, so no effort was made to model individual plies. For computational simplicity, the plate impact setup was modeled initially as a single row of cubic (hexahedral) elements, representative of the 3D interiors of the GRP and flyer plate. It was deemed unnecessary for the GRP and the flyer plate to match the exact experimental geometries and dimensions since the plate impact model implementation served only as a proof-of-concept and to aid model calibration. Given the experimental thickness of the GRP was 6.8 mm, an element size of 0.1 mm x 0.1 mm x 0.1 mm was initially chosen, resulting in a row of 68 elements. Following the suggestion by Scott et al. [16], the flyer plate thickness was set to 25.4 mm. This was done to ensure the release waves from the back surface of the flyer would arrive at the GRP well after the time window of interest. Good computational technique demands a consistent element size for the GRP and the flyer plate. As a result, the flyer plate was represented by a 254-element row. At the commencement of the simulation, the contact faces of the GRP and flyer were together; the interface matched node-to-node to encourage a clean contact response. To model the uniaxial strain capabilities of the plate impact test, “roller” boundary conditions were applied to the whole model, which restricted movement to only permissible in the shock direction

and with no rotation allowed. In this specific model, the shock propagated along the z-axis, and the fibers were oriented in the x-y plane.

Preliminary analyses suggested that better results could be achieved by using a finer mesh size and different mesh geometries. A comparison of results for an array of mesh configurations is presented in the sensitivity study. The best quality velocity profiles were attained using cubic 0.05 mm x 0.05 mm x 0.05 mm elements, so this was chosen instead of the original 0.1 mm x 0.1 mm x 0.1 mm element size. The overall dimensions of the GRP and flyer were kept the same. Table 7 summarizes the mesh geometries and element amounts. Furthermore, a trade-off between velocity profile quality and computational time led to the decision to use a 0.4 ns time step, meaning 15,000 increments were used for the analysis. The maximum time window of interest was 6 μ s, which was 4 μ s after the rear surface velocity profiles commenced.

Table 7. Abaqus plate impact model mesh details

Flyer Plate				GRP			
Total Dimension (mm)	Element Dimension (mm)	Elements	Nodes	Total Dimension (mm)	Element dimension (mm)	Elements	Nodes
0.1 x 0.1 x 25.4	0.05 x 0.05 x 0.05	2032	4581	0.1 x 0.1 x 6.8	0.05 x 0.05 x 0.05	544	1233

Correct definitions of user-defined material properties and state variables were an integral step in building an accurate model. The VUMAT subroutine called for 30 material properties and 6 state variables, all tabulated in Table 8. Abaqus does not provide units, so all dimensions and values used throughout the model were in terms of SI units. Boldface properties were calibrated using the plate impact simulations and are a focus of the sensitivity study in the Results and Discussion chapter. Underlined properties were arbitrarily set but could not be calibrated using the plate impact simulations since they were never required in the analysis.

Table 8. Abaqus user-defined material properties

Definition	Property No.	State Variable	State variable number
G	1	ϵ_{eq}	1
K	2	R^{MS}	2
β	3	R^{ME}	3
k1	4	d^M	4
k2	5	d_1^f	5
M11	6	d_2^f	6
M12	7		
M13	8		
M21	9		
M22	10		
M23	11		
c1ems	12		
Jec	13		
<u>Jet</u>	<u>14</u>		
iota	15		
ems	16		
tcrit	17		
ccrit	18		
C11	19		
C22	20		
C33	21		
C44	22		
C55	23		
C66	24		
C12	25		
C13	26		
C23	27		
<u>eta</u>	<u>28</u>		
alpha	29		
c1alpha	30		

IV.2 BALLISTIC PENETRATION SIMULATION

The model built to simulate FSP penetration tests simplified the setup Prifti et al. [14] used for their experiments. Unlike the “representative” Abaqus model for plate impact testing, the fragment and GRP plate dimensions matched the penetration experiments exactly. Like the plate

impact simulations, the GRP was modeled as a continuum, so the effects of ply de-bonding and individual ply deterioration were not accounted for. The support offered by the steel frame was incorporated as a fixed boundary condition for all four thickness sides of the GRP. A boundary condition restricting the FSP to only travel in the direction normal to the GRP impact face was also employed. Since the GRP was the sole focus of this thesis, the thin aluminum back plate was not included. The model parameters used for the penetration tests were the values calibrated for the high-velocity plate impact test. This was because all fragment strikes exceeded the highest velocity flyer plate test.

The simulations involved highly-strained elements and consequently required methods to control element distortion. Without such methods, the analyses aborted early due to the Abaqus error “excessively distorted elements”. To alleviate these issues, conversion to spherical particles was used. This technique is advantageous over “element deletion” since the particles retain some resistance to deformation beyond finite element distortion levels [27]. Furthermore, particle conversion eliminated the need for artificial viscous damping, which is typically used to help prevent element inversion. Particle conversions were programmed in the “Element Type” window to activate when principal strains in an element reached or exceeded 1. One particle was produced per element. One obstacle encountered in simulations was a diminishing resistance to the FSP travel due to particle conversion. At impact velocities of approximately 900 m/s and above for the small caliber FSP, too many elements in the FSP path converted to particles (due to complex damage propagations). This in turn meant the GRP structure no longer provided any resistance to the FSP, which would continue along its path for perpetuity, albeit at a much lower velocity. These scenarios make determining an accurate DOP or rear surface maximum displacement impossible, therefore results for tests where this issue arose were not reported. This issue was more severe for

simulations tested using “element deletion”, which validated the decision to employ particle conversion as an element distortion control.

For computational ease, variable mesh sizes were used on the GRP impact face by creating “partitions” resembling a target. The mesh size was gradually increased in concentric circular regions at increasing distances from the fragment impact location. This was done to focus the computational detail on the areas close to penetration impact, while not wasting computational resources on areas of little interest. The smallest partition was the same area as the FSP, to encourage node-to-node alignment at the impact face. To satisfy Abaqus’ requirements for particle conversion, the mesh size could not be too fine, or too concentrated in a particular region. Balancing computational detail with particle conversion requirements motivated the element size choice. The element size and corresponding region are summarized in Table 9 and illustrated in Fig. 9.

Table 9. Element sizes for GRP penetration simulation

Element size (mm)	Target area diameter (mm)
4 x 4 x 4	FSP
4 x 4 x 4	30
4 x 4 x 4	50
8 x 8 x 4	70
22 x 22 x 4	90
22 x 22 x 4	Rest of GRP face

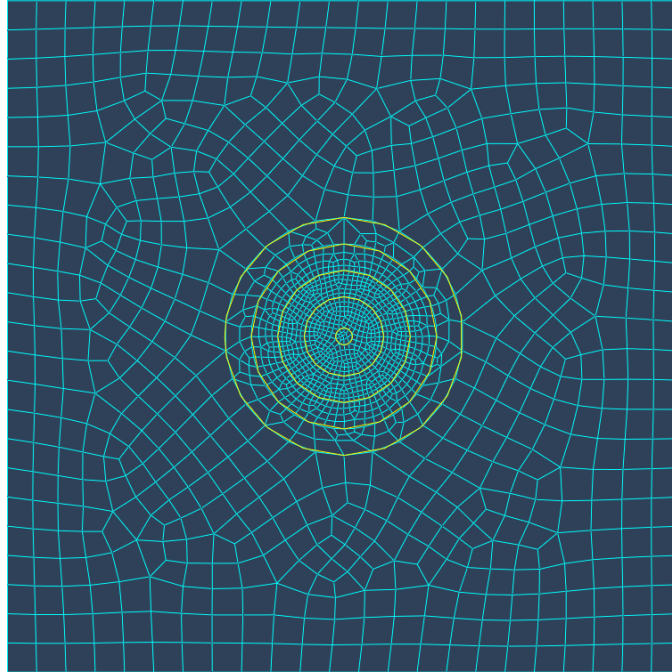


Figure 9. Mesh size variation on the GRP impact face

The mesh seeding in the thickness direction had to remain constant to satisfy Abaqus's mesh compatibility requirements. Element thicknesses were set to 4 mm to satisfy particle conversion requirements and to create cubic elements to resemble what was used for plate impact simulations. The simulations encountered errors relating to a "too high concentration" of particles if element thicknesses below 4 mm were used. This could have been overcome if the whole GRP used the same size cubic elements, however, due this was not an option due to computational expense.

CHAPTER V

RESULTS AND DISCUSSION

The current work seeks the answer to two questions: 1) can the developed hyperelastic CDM-based computational model (the FCM) accurately predict the shock response of GRP behavior under an ideal one-dimensional strain environment, and if so, 2) how applicable is this model to ballistic penetration scenarios to predict DOP, rear surface displacement, shock stress propagation, and fiber damage evolution? To answer question 1, a sensitivity study was performed to evaluate the influence of damage model parameters on the salient features observed in measured velocity profiles (VISAR signals) in plate impact experiments. Mostly, the matrix damage influenced the VISAR signal features under compressive loading; however, the fiber damage had a considerable influence on the GRP response to FSP penetration processes. Therefore, it is important to investigate and model the fiber damage in GRP to address question 2.

V.1 PLATE IMPACT RESULTS

A key stage in establishing the validity of the FCM was its calibration. The test LT48 particle velocity profile obtained by Tsai et al. [11] was the data by which empirical parameters in the hyperelastic damage model were tuned. This specific plate impact test, performed at the highest velocity of 417.96 m/s, was selected because the VISAR signal revealed various salient nonlinear features. Also, this velocity level was thought to compare most favorably to the higher velocity FSP penetration tests. The VISAR data for LT48 also showed unique features just above the elastic-elastic cracking (EEC) or HEL-like bifurcation point. The lower velocity profiles did not

show a prominent EEC, instead, the particle velocity profile ramped in a nonlinear manner to the peak velocity. The sensitivity studies were necessary to interpret the salient features observed in all impact velocities. For this purpose, the effects of different parameters and their values on the shock stress histories in GRP at various locations and the shape of simulated free surface velocity time histories (or profiles) were investigated through Abaqus simulations.

Damage initiation and evolution as the shock wave propagated through the GRP greatly influenced the velocity profiles, especially in the non-linear portion. Consequently, the sensitivity studies focused on establishing a set of parameters that produced velocity profiles that matched qualitatively, and if possible, quantitatively, the VISAR signals reported by Tsai et al. [11]. The FCM parameters of focus were β , c_1^{ems} , J_e^c , ι , α , and c_1^α . Furthermore, the influence of element size on the salient features in the velocity profiles was analyzed. The sensitivity study provided useful insight into how these empirical parameters interacted within the hyperelastic damage model and helped foster a greater understanding of the GRP response to shock impact.

V.1.A ELEMENT SIZE

It is well known that damage models are inherently mesh-dependent and are consequently vulnerable to convergence issues related to mesh resolution. This is especially true for finite element representations of localized plastic deformation, as well as weakly strain rate dependent deformation processes, such as in the GRP and other brittle materials. A review paper by Murakami and Liu [28] covered the reasons for mesh dependency in CDM models implemented using the finite element method (FEM). They noted that in brittle materials, in particular, material instabilities may cause bifurcation and strain localizations that are difficult to capture accurately without correct mesh sizes. Their paper detailed several regularization methods to overcome mesh dependencies, such as employing a minimum admissible mesh size or using mesh-dependent

material properties. In-depth explanations of these techniques are outside the scope of this thesis, however, shortcomings of these methods, in particular, are clear; determining the mesh size that conforms to material properties and material discontinuities is difficult and using a mesh-dependent material property departs from the property's physically-determined nature. For this thesis, capturing the true physical response of the GRP was emphasized, so no mechanical properties were altered from their true values.

In the simulations, the mesh dependency was associated with moduli degradation (softening) in discrete elements. The Abaqus simulations represented the GRP as a 6.8mm thick plate, while physically the GRP consisted of ten stacked 0.68mm plies. If each ply was segmented into two elements in the thickness direction, damage to one element applies an instantaneous degradation to half the thickness of the ply. In this instance, a too coarse mesh may over-generalize stiffness changes, and apply such changes to regions that would not physically encounter the same degradation. On the other hand, a finer mesh, such as 20 elements per ply in the thickness direction, dampens the contribution of individual elements. This localizes damage changes better than the coarse mesh but may underestimate the area affected by damage in a particular element. A fiber breakage in one element should propagate this loss of integrity to the whole extent of the fiber, however, if that fiber spanned multiple elements, the elements without the breakage may still treat the fiber as unbroken. Thus, a balance must be struck in the level of element discretization present. This motivated the element-size sensitivity study, such that the FCM could optimally model the GRP response to shock impacts.

To minimize model inaccuracies caused by poor mesh choice, 8 different mesh sizes and geometries were considered in the sensitivity study. The finest cubic element size was 0.02 mm x 0.02 mm x 0.2 mm, while the finest volume element tested was 0.025 mm tall x 0.025 mm wide x

0.01 mm thick. At finer sizes, it became apparent that numerical instabilities were starting to factor, and the analyses were moving further from the solution. The study concluded that out of the sizes tested, cubic 0.05 mm x 0.05 mm x 0.05 mm elements were most appropriate for the plate impact simulations. Expected strains never exceeded 13% in compression, therefore cubic elements were of sufficient geometry and did not excessively distort. The “representative” nature of the plate impact simulations meant a relatively low number of elements were used. Therefore, computational time was never a concern, and mesh geometries were kept the same for both the GRP and the 4x larger flyer plate. Using consistent mesh sizes ensuring that the nodes at the impact face on the GRP and the flyer matched exactly, encouraged a clean contact response. Fig. 10 compares six of the tested element geometries for test LT48, each with a different thickness.

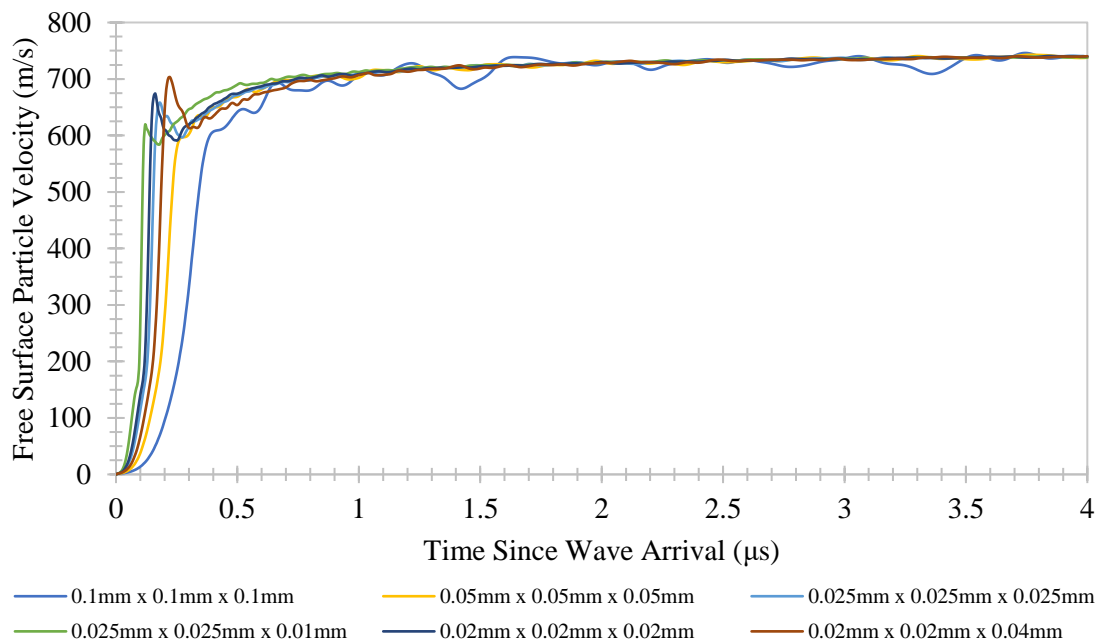


Figure 10. Element size particle velocity profile comparisons

Several observations were made during the element size adjustments. As the thickness of the elements decreased, the arrival time of the shockwave increased, suggesting shock wave propagation was in some cases penalized by the fineness of the mesh. The opposite case was also

true; using a too coarse mesh propagated the shock wave too quickly as the discrete jumps between elements were too large. For the tested element geometries, the correlation between thickness and shock wave arrival time is depicted in Table 10. Matching the arrival time to the experimentally-determined 1.978 μs [11] was one reason the cubic 0.05 mm element was chosen.

Table 10. Element thickness effects on shock wave arrival time

Element Thickness (mm)	Shock Wave Arrival Time (μs)
0.10	1.87
0.05	1.97
0.04	2.00
0.025	2.02
0.02	2.03
0.01	2.06

In addition to shock wave arrival time, the point of EEC initiation and development of the nonlinearity in the velocity profile until the peak particle velocity was reached were important in element size choice. The velocity profiles for finer mesh sizes were characterized by steeper initial rises, a more pronounced EEC transition point, and a smoother tapering up to the peak velocity. The coarser element sizes possessed a longer rise time yet achieved a more accurate representation of the oscillations in the transition between the EEC initiation and the peak velocity. These findings further motivated the choice of the 0.05 mm cubic element.

V.1.B OGDEN PARAMETER

The Ogden parameter β appears only in the volumetric term of the hyperelastic constitutive equation (recall Eq. (13) in the FCM and is an arbitrary empirical coefficient.

$$\boldsymbol{\sigma} = \frac{G}{J} \left(\bar{\mathbf{b}} - \frac{\text{tr}(\bar{\mathbf{b}})}{3} \mathbf{I} \right) + \frac{K}{J\beta} (1 - J^{-\beta}) \mathbf{I} + \frac{2k_1}{J} (\mathbf{m}_1 \cdot \mathbf{m}_1 - 1) \mathbf{m}_1 \otimes \mathbf{m}_1 + \frac{2k_2}{J} (\mathbf{m}_2 \cdot \mathbf{m}_2 - 1) \mathbf{m}_2 \otimes \mathbf{m}_2 \quad (13)$$

The effect of β on the wave propagation was studied through simulations with and without damage. To deduce the value for β in the FCM, undamaged simulations of the elastic and hyperelastic constituent models of the FCM were run separately. The hyperelastic, β -dependent model was tuned to match the salient features of the elastic model velocity profile using different β . To find values for β , every integer between 6 and -6 was tested, then once a value closely matched the velocity profile results obtained by the elastic FCM, increments of 0.1 were used to converge to an acceptable β . Fig. 11 depicts the effect of β changes on the undamaged hyperelastic model:

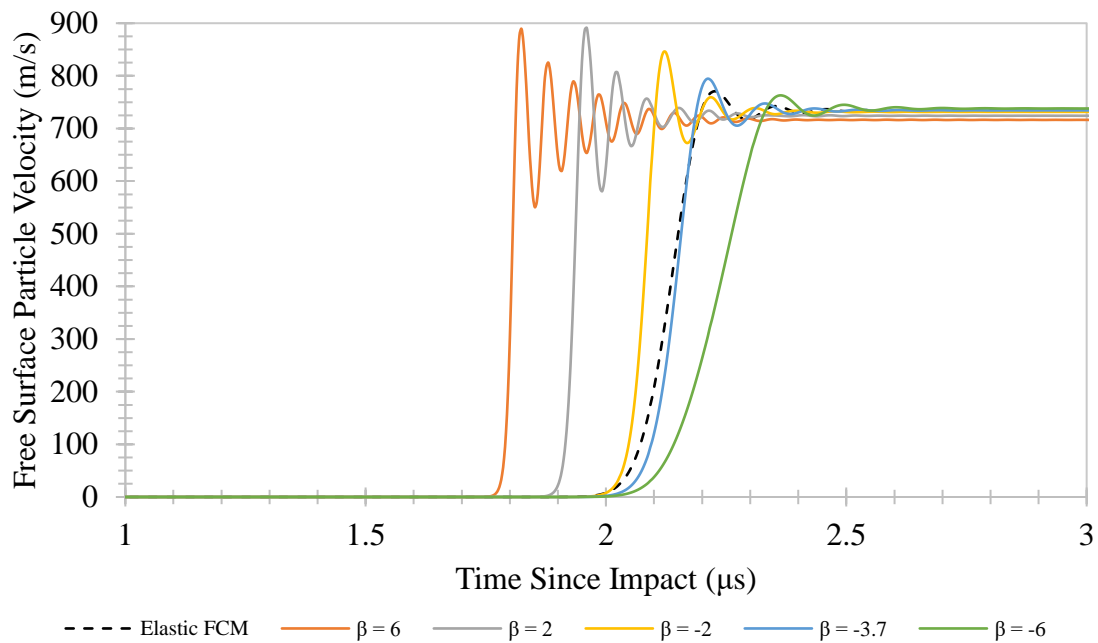


Figure 11. β effect on the undamaged hyperelastic model

Since the value of β influences the volumetric strain (2nd term in Eq. (13)), the shock wave speed changes with this parameter. The overshoot and oscillations were characteristic of how numerical methods used for finite element analysis handled function discontinuities, so no efforts were made to mitigate this. The effect of β on shock wave speed required further investigation, and it was found that the hyperelastic constitutive model yielded a nonlinear, β -dependent bulk modulus K .

$$C_L = \sqrt{\frac{K + \frac{4}{3}G}{\rho}} \quad (53)$$

where C_L is the shock velocity.

Fig. 12 illustrates the variation of pressure with strain for test LT48 at a point 1/4 the GRP thickness away from the impact face. The gradient of the pressure (P) – volumetric strain (e_v) curves in Fig. 12 is the effective bulk modulus of GRP. The increase in wave speed is directly associated with the increasing slope for larger β values, reflecting the arrival time differences in Fig. 11. For comparison, P vs. e_v (or ϵ_{33}) is plotted for various β values. It should be noted that in the uniaxial strain plate impact scenario, volumetric strain is equivalent to strain in the shock direction ϵ_{33} . The shape of the curve for $\beta = 6$ shows a typical concave-up response as in a typical equation of state. However, the shape becomes concave down for smaller β values, especially for the negative values.

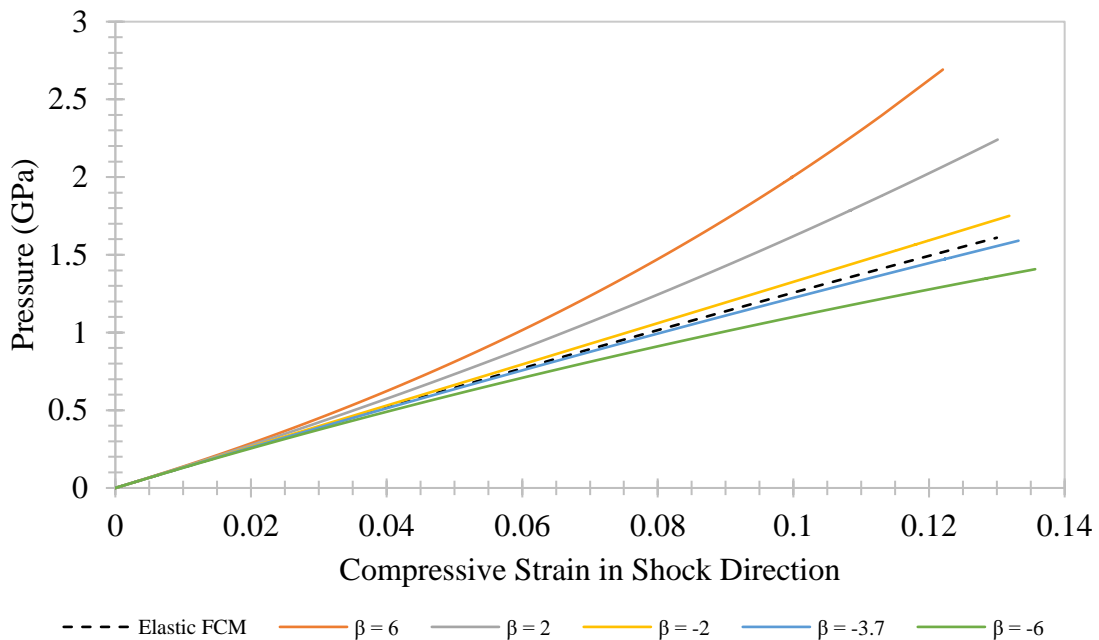


Figure 12. Pressure and strain response to β changes

The dotted line in Fig. 12 is for a simple elastic response based on the elastic stiffness matrix in Table 1. Through iteration, $\beta = -3.7$ was found to produce the response that best matched the shock wave arrival time, rise time, and the peak particle velocity observed in the elastic FCM.

To investigate further how the volumetric term in the hyperelastic stress-strain relationship is influenced by the slope (bulk modulus) of the Pressure vs. Compressive Strain curves for various β values, Fig. 13 was constructed using the gradient of the curves in Fig. 12. Note that the slight reduction in K in the elastic case in Fig. 13 is due to a numerical artifact of artificial viscosity.

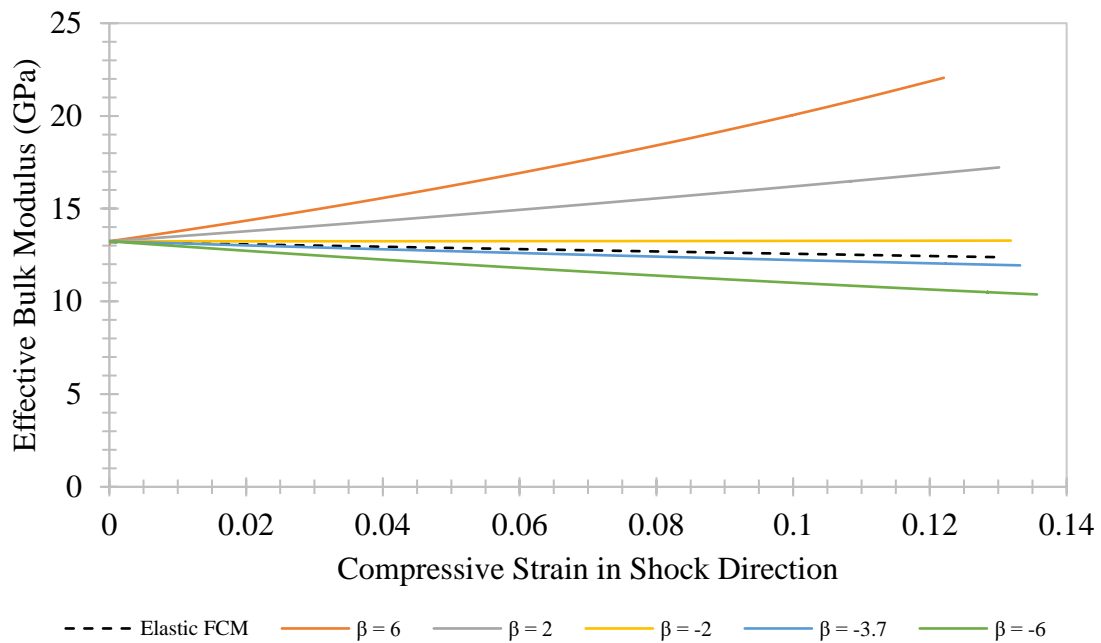


Figure 13. Bulk modulus evolution for different β values

These numerical exercises demonstrated that the hyperelastic constitutive equations are sensitive to β and the shape of the pressure-volume curves can vary from convex to concave depending on the β values as shown in Figs. 12 and 13. It should also be noted that the total stress-strain curve would include the first (volume-preserving) term of the hyperelastic constitutive

equation that does not contain β . The value of -3.7 is used in all FCM simulations of both plate impact and ballistic tests.

V.1.C MATRIX SHEAR DAMAGE STRAIN RATE DEPENDENCY

As mentioned earlier in section II.2.B, the strain rate effect on damage evolution is introduced through Eq. (33). The c_1 constant, in general, is a weighting term assumed to be different for different failure modes. For instance, it is termed as $c_{1,ems}$ for matrix shear cracking. The variable or “var” in Eq. (33) corresponding to shear cracking is the critical matrix shear strain ϵ^{MS} . The ϵ^{MS} term dictated the development of shear modulus damage in the GRP matrix. Thus, the strain rate effect on ϵ^{MS} became important in ensuring the EEC transition point in the particle velocity profile occurred at the correct velocity.

Figs. 14 & 15 illustrate the effects of $c_{1,ems}$ in terms of the velocity profiles and the matrix shear damage criterion respectively. Data for the matrix shear damage criterion was taken at an element 1/4 the thickness of the GRP away from the impact face. Increases in the velocities of the EEC transition were clearly evident in Fig. 14 and corresponded with increases in $c_{1,ems}$. Over the range of $c_{1,ems}$ values tested, the arrival time of the shock wave and rise time of the velocity profile varied slightly. This was due to the contribution of shear damage to the overall matrix damage, which resulted in small changes to the shear and bulk moduli and ultimately the shock velocity and shock stress.

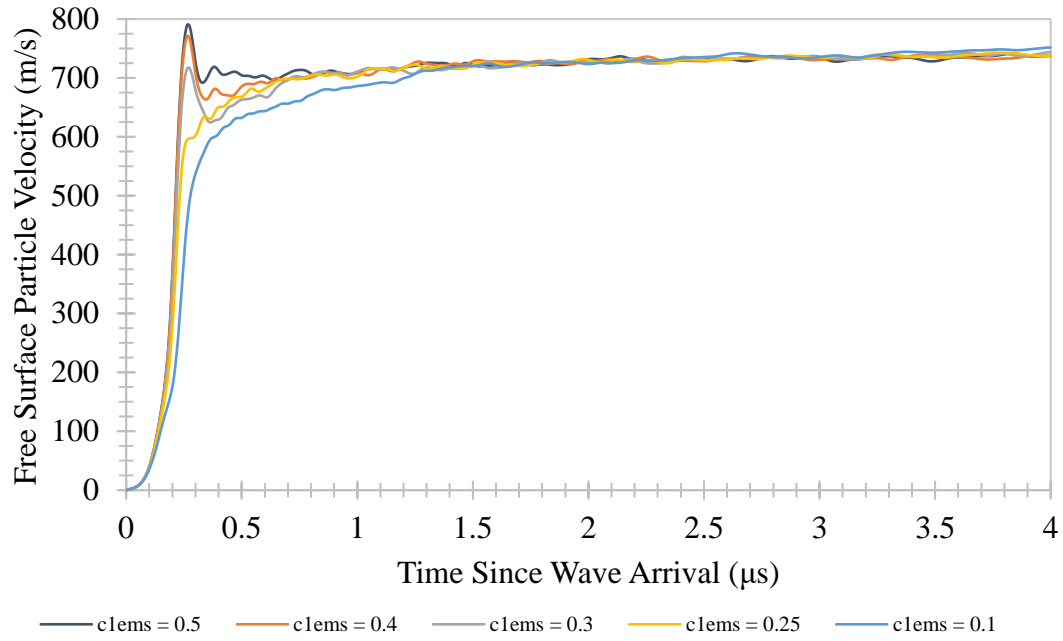


Figure 14. Matrix shear damage strain rate effect on velocity profiles

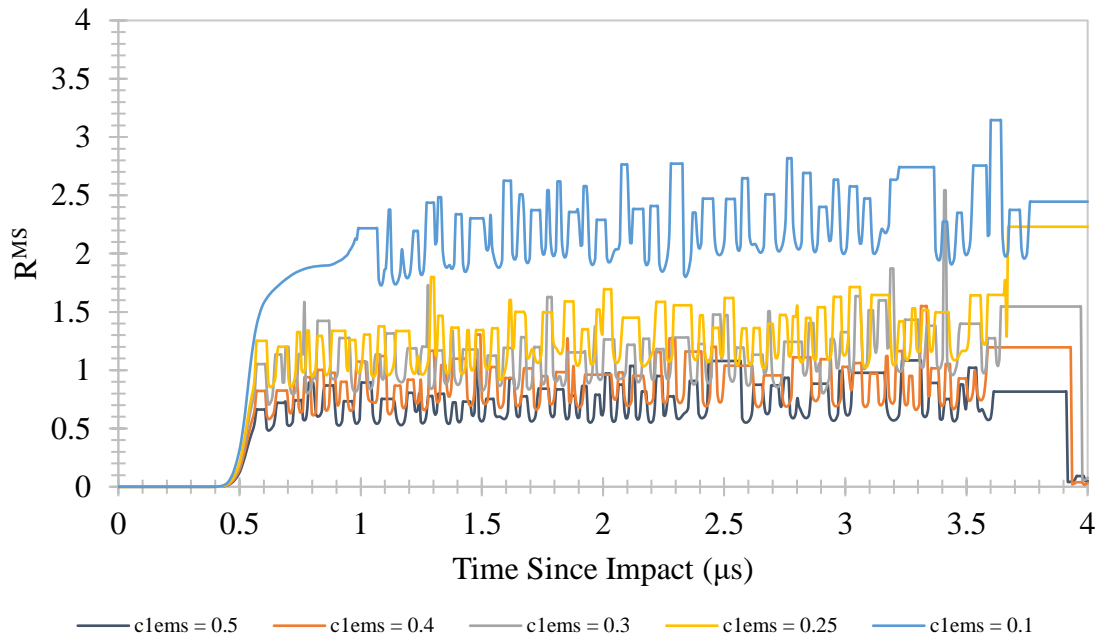


Figure 15. Matrix shear damage criterion response to strain rate weighting

V.1.D COMPRESSIVE MATRIX BULK DAMAGE

Multiple user-defined parameters were used in the FCM representation of bulk modulus degradation. To reflect damage growth in compression due to bulking and the eventual damage relaxation due to lateral confinement effects, Eq. (22) was developed.

$$R^{ME} = \alpha(1 - J)e^{\frac{J}{J_e^c}} \quad (22)$$

The characteristics of this equation were discussed earlier in Section II.2.B. Further insight into this equation is provided here. The assumptions in the above equation are that 1) the brittle matrix (epoxy) cracks under compression through the “wing crack” mechanisms described earlier in Section II.2.B, and 2) as J decreases from 1 to 0 for increasing shock stresses, the bulk damage, after reaching maximum at certain velocity levels, decreases due to increasing lateral confinement since the damage mechanism changes from splitting to faulting. The parameters J_e^c , α , and $c_{1,\alpha}$ were jointly used to describe bulk modulus degradation under compressive loading. To keep the bulk damage criterion R^{ME} within an acceptable range for the model, J_e^c and α were carefully coupled since the exponential term created an extremely volatile equation. These two parameters were the “blunter” tools for bulk damage tuning, while $c_{1,\alpha}$ enabled “finer” tuning.

Fig. 16 displays an array of bulk damage criterion responses to changes in α with a constant J_e^c . Note that the initial spike is reminiscent of Eq. (22) as shown earlier in Fig. 2. By design, increases in α led to linear increases in R^{ME} . Strain rate effects on α (like for the ϵ^{MS} term) led to increases in α and promoted greater matrix bulk degradation (seen by the rising peaks in Fig. 16).

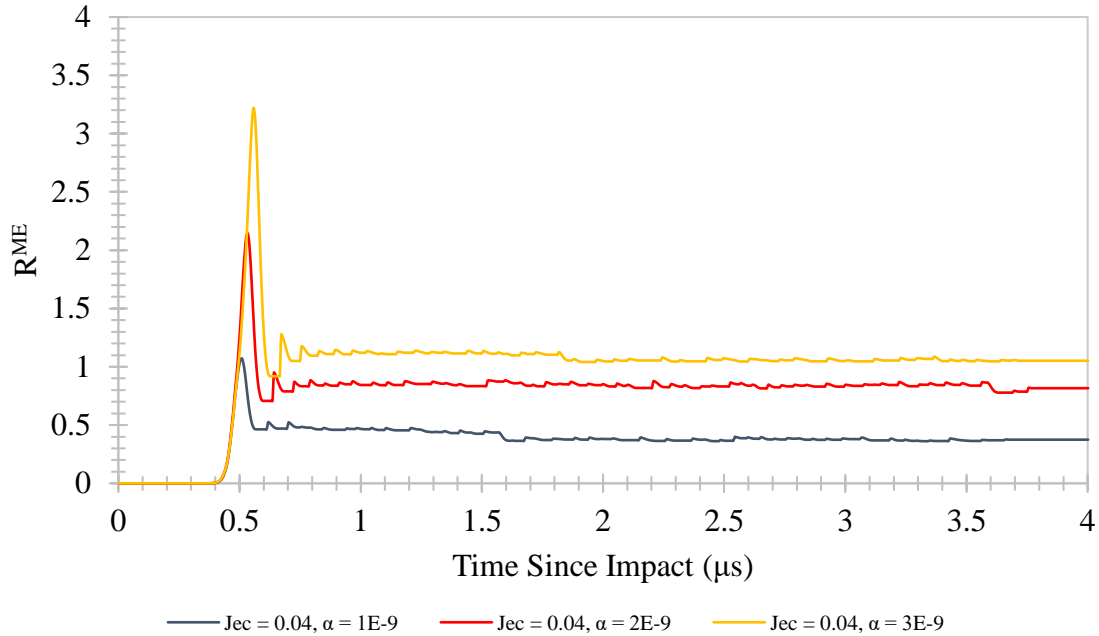


Figure 16. Matrix bulk damage response to α changes

Fig. 17 depicts changes in the bulk damage criterion in response to changes in J_e^c , with α selected to approximate the same R^{ME} peaks. The key features of this graph are the changes in the “settled” R^{ME} values and the differences of magnitude in α required to match R^{ME} peaks. When tuning the FCM, J_e^c values between 0.03 and 0.1 were, as these were the strains within the range established by the low-velocity test LT30 and the high-velocity test LT48. By setting J_e^c in this range, LT30 remained in the bulking stage, while LT48 progressed through the bulking stage and into the lateral confinement stage. The extent to which R^{ME} diminished after its peak (due to lateral confinement) was dictated by how low J_e^c was, i.e., how quickly the R^{ME} function peaked. Quicker peaks of R^{ME} were characterized by sharper drops, when the maximum strain of test LT48 was reached, lateral confinement effects were at their greatest (relative to the other tested values). Also noteworthy is the magnitude changes of α needed to counteract the effect of J_e^c on the exponent. This relationship illustrates why J_e^c , α , and $c_{1,\alpha}$ were considered “coupled”.

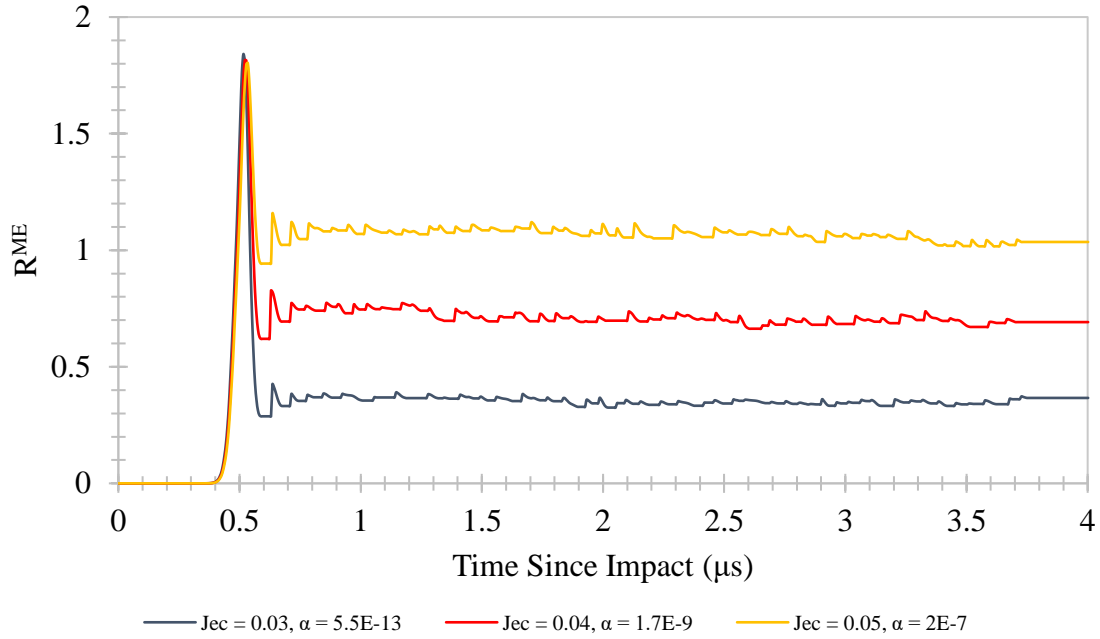


Figure 17. J_e^c effects on matrix bulk damage

Ultimately, the goal of tuning J_e^c , α , and $c_{1,\alpha}$, and in turn, the evolution of R^{ME} , was to achieve the most accurate reproduction of the particle velocity profile of test LT48. All J_e^c and α configurations present in Figs. 16 & 17 appear in Fig. 18 to reinforce the effect of R^{ME} on particle velocity profiles. One of the obstacles encountered when tuning these parameters was ensuring that there was enough bulk damage to recreate an accurate damage progression, but not too much causing the initial rise to kink too early. In all examples seen in Fig. 18 except the dark blue plot, a kink occurred before 100 m/s, which was caused by excessive peaks in the R^{ME} plot. The plots using values taken from Fig. 17 were almost coincident. After performing this study, values of 0.04 for J_e^c , $1E-9$ for α and 0.001 for $c_{1,\alpha}$ were chosen.

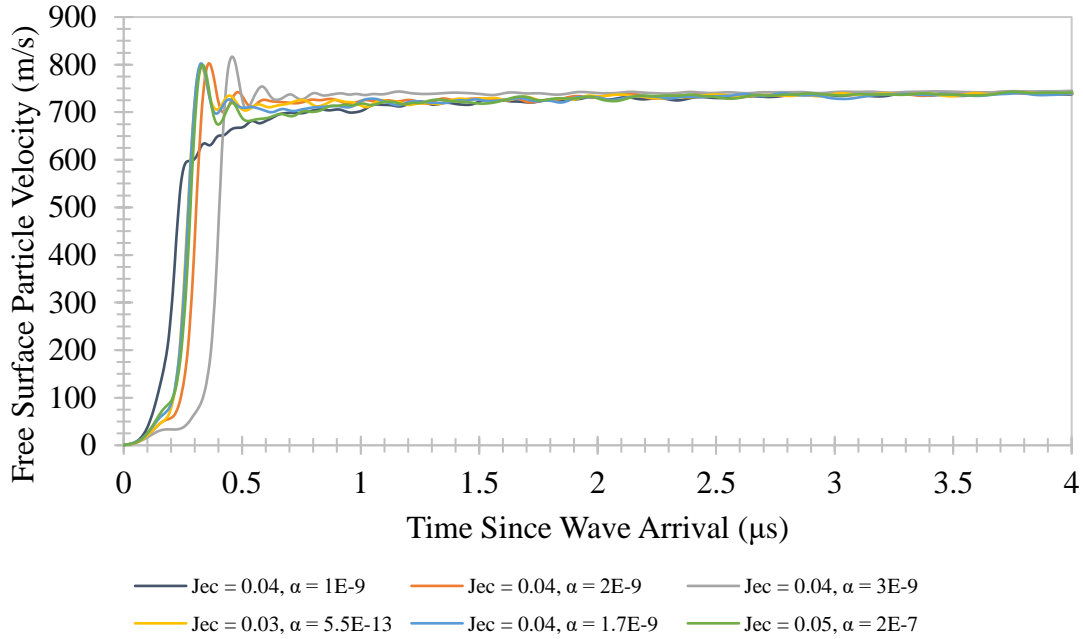


Figure 18. Collection of J_e^c and α combinations and their effects on particle velocity profiles

V.1.E MATRIX DAMAGE DAMPING

The general matrix damage damping parameter ι was an effective tool in dictating elastic-plastic transition velocity, and the behavior of the velocity profile once the transition was surpassed. Instead of impacting R^{MS} or R^{ME} individually, ι affected the contribution of the coupled damage criterion R^M (recall Eq. (24)).

$$d^m = 1 - \exp\left(\frac{1 - R^M}{\iota}\right) \quad (24)$$

As a result, ι amplified the behaviors of all previously mentioned matrix damage parameters.

A comparison of particle velocity profiles with changes in ι is displayed in Fig. 19. Throughout the calibration, ι values from 2 through 40 were tested, with the final value set as 10. This was contingent on the other user-defined parameters used. An observation gathered from Fig. 19 is that the lower the ι value, the matrix damage not only increases but in greater proportions. The velocity profile difference between $\iota = 2$ and $\iota = 6$ is much greater than the difference between

$\tau = 20$ and $\tau = 30$. This behavior matches the expectation given the location of τ in the denominator in Eq. (24).

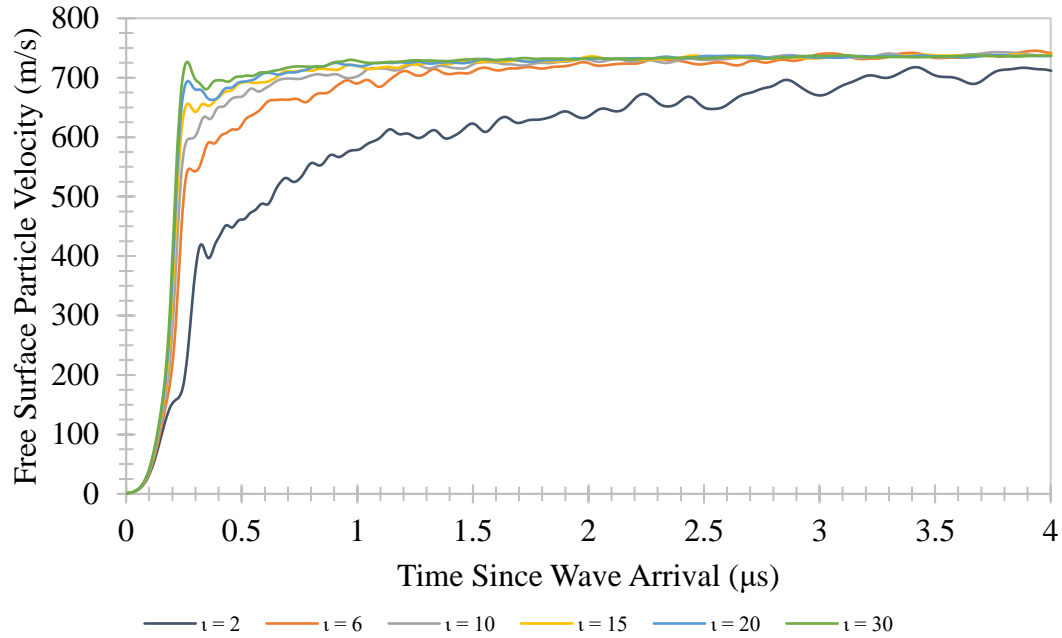


Figure 19. τ damping effect on particle velocity profiles

V.1.F ELASTIC UNDAMAGED MODELS

To establish a baseline check for the applicability of the hyperelastic model that constitutes the damage-enabled FCM, undamaged runs of the LLM hyperelastic model were compared to undamaged runs of the FCM (the elastic model). All material properties and model parameters used for the FCM are presented in Table 11.

Table 11. Abaqus simulation user-material properties and parameters

Property	Value
G	4.63E9
K	13.24E9
β	-3.7
k1	86.9E9
k2	86.9E9
M11	1
M12	0
M13	0
M21	0
M22	1
M23	0
c1ems	0.25
Jec	0.04
Jet	2
iota	10
ems	0.0215
tcrit	0.057
ccrit	-0.00395
C11	31.55E9
C22	31.55E9
C33	20.12E9
C44	4.63E9
C55	4.63E9
C66	4.94E9
C12	15.86E9
C13	9.75E9
C23	9.75E9
eta	0.8
alpha	1E-9
c1alpha	0.001

Properties pertinent to the undamaged hyperelastic model are highlighted in grey, and properties used for the elastic FCM model are highlighted in yellow. Tsai et al. [11] reported values for G, K, and all C_{ij} elastic constants; G from the C_{44} and C_{55} values, and K was calculated from the ultrasonically measured 2.6 km/s bulk wave speed. ϵ^{MS} was taken from the matrix properties used

for Scott's thesis [29]. The critical tensile fiber strain 'tcrit' was taken from a Matweb database [30], and 'ccrit' was estimated using a buckling equation given in Eq. (54).

$$\sigma_{\text{buckling}} = \frac{\pi^2 E}{\left(\frac{l}{r}\right)^2} \quad (54)$$

No slenderness ratio was given for the individual fibers (only dimensions for the bundles were provided) so a ratio of 50 was assumed arbitrarily, which after applying Eq. (54) yielded a buckling strength of approximately 343 MPa. Further application of Hooke's Law yielded the critical compressive strain value used.

Fig. 20 offers a comparison between both the undamaged hyperelastic and undamaged elastic-FCM models, and the experimental velocity profiles of Tsai et al. [11] for high-velocity (LT48, 417.96 m/s), intermediate-velocity (LT31, 312.7 m/s), and low-velocity (LT30, 111.69 m/s) tests. The GRP thicknesses for these three tests ranged between 6.55 mm and 6.76 mm. The hyperelastic and elastic-FCM undamaged runs showed great agreement with each other in terms of peak velocity (within 1.5 m/s) for the three tested velocities. The peak velocity for the models underestimated the experimental values by 5.8%, 3.5%, and 0.9% for LT48, LT30, and LT31 respectively. These margins were deemed acceptable enough to proceed. Sluggish rise times in the models compared to the sharpness in LT48 were suspected to be a limitation of how the finite element method treats sharp discontinuities, as mentioned in the Ogden Parameter section of the sensitivity study. Reductions in oscillations at the velocity rise-plateau transition point were possible if finer meshes were used, however, as stated in the sensitivity study, the mesh size was chosen with practical, damage-enabled modeling in mind. Even in the finest mesh size used, these oscillations could not be fully eliminated.

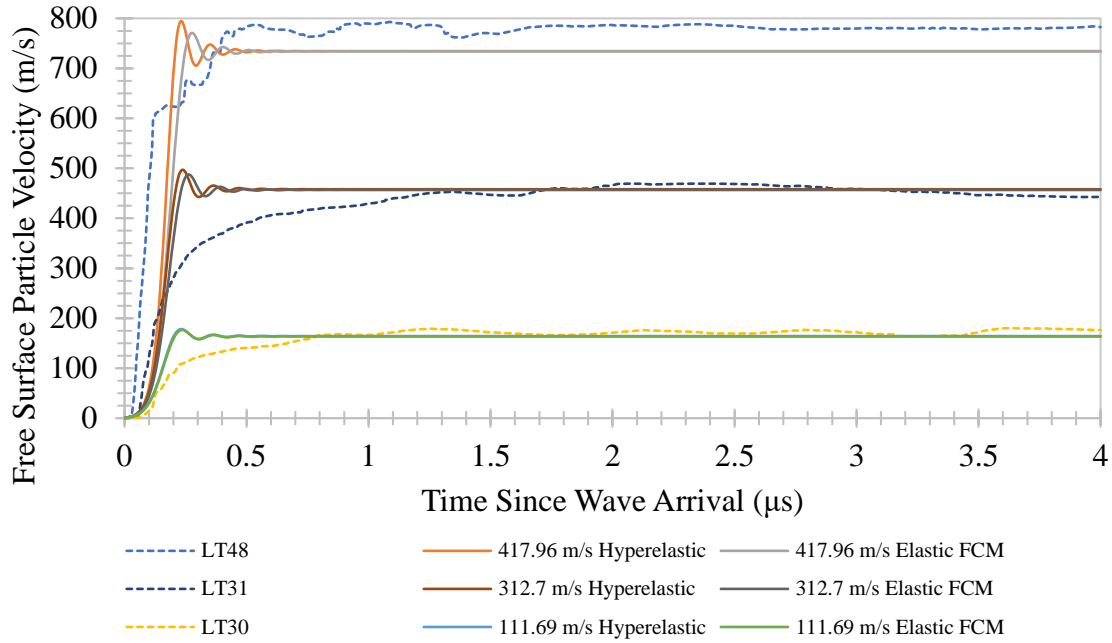


Figure 20. Undamaged elastic model comparison to experimental data [11]

Shock stress and strain values in Table 12 show the undamaged models had good agreement with the Hugoniot estimations by Tsai et al. for the low (LV) and intermediate (MV) velocity tests, and good agreement with the stress estimation for the high-velocity (HV) test.

Table 12. Model stress and strain comparison to Hugoniot values

Model Type	Stress (GPa)	Strain (%)
LV Hyperelastic LLM	0.51	2.61
LV Elastic FCM	0.51	2.56
LV Hugoniot	0.55	2.26
MV Hyperelastic LLM	1.42	7.26
MV Elastic FCM	1.43	7.12
MV Hugoniot	1.57	6.50
HV Hyperelastic LLM	2.29	11.51
HV Elastic FCM	2.30	11.44
HV Hugoniot	2.31	9.80

V.1.G DAMAGE-CAPTURING MODELS

The enhanced capability of the FCM captures both the elastic response of the GRP and the plastic response once damage initiates. The damage modes captured in the FCM were matrix

damage and fiber damage, however, in the plate impact simulations, uniaxial strain in the shock direction meant fiber damage perpendicular to the shock direction was neglected. The contributions of fiber strength and damage will be thoroughly explored in the ballistic penetration simulations. As stated in Chapter II, delamination damage was not considered for this model as the GRP was modeled as a continuum, and further work needed to be done to deduce a satisfactory physically-representative delamination damage criterion. As noted by Scott [29] and Scott et al. [16], delamination damage played a major role in their simulations, so the FCM is somewhat limited in its ability to fully capture GRP damage development in shock loadings.

To test the validity of the FCM, particle velocity profiles were compared to tests LT48, LT31, and LT30, encompassing a range of impact velocities. Fig. 21 displays the simulated particle velocities, where the user-defined parameters for the FCM were chosen to optimize the high-velocity profile.

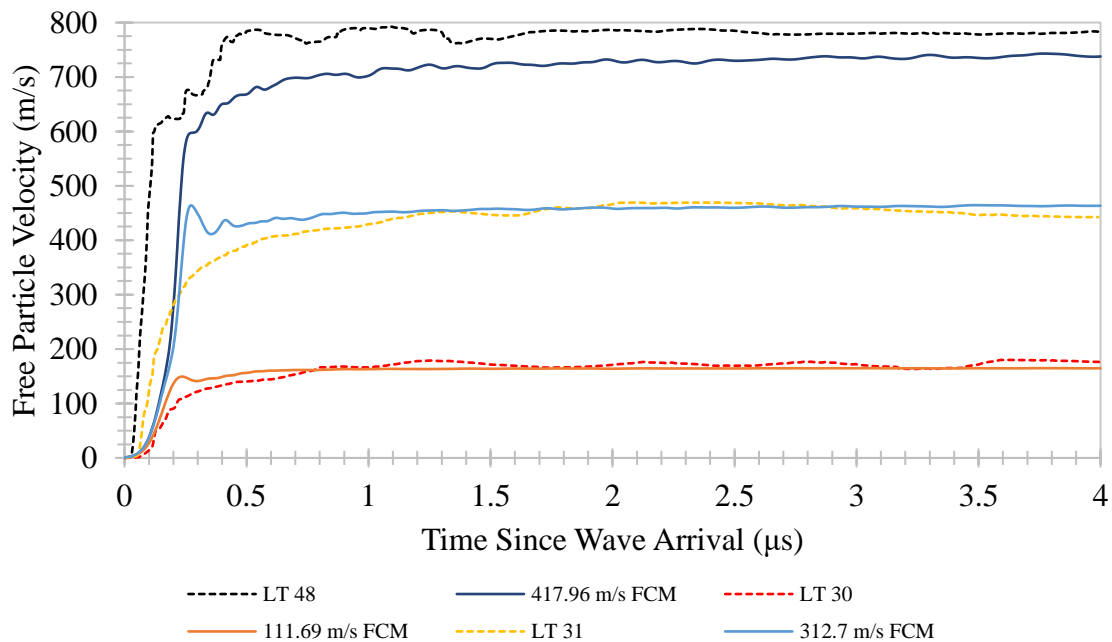


Figure 21. FCM prediction for free surface particle velocity at low, intermediate, and high-velocity plate impacts

Given the complexity of the GRP architecture, the inherent variation possible in the VISAR data, and the multitude of user-defined parameters that required calibrating, the FCM predictions match the VISAR data reasonably well. For all tests, the peak velocities agreed with the elastic Hugoniot established by the Rankine-Hugoniot conditions and showed excellent agreement with the peak velocity predictions of Scott et al. [16]. As they were in the elastic undamaged runs, the rise times remained slower than the experimental profiles. Though the HEL-like bifurcation mark for the high-velocity test matches the experimental prediction, the intermediate and lower velocity tests fail to capture this sharp transition point. The level of damage necessary to match the profile shape after the transition point for the high-velocity test was too low to adequately capture the tapered velocity profile seen for the intermediate and low-velocity profiles. Fig. 22 illustrates how the greater damage needed to optimize the lower-velocity profile was not a valid option for the high-velocity test. In Fig. 22, “HV Ideal” used the FCM with parameters tuned towards test LT48, while “LV Ideal” uses parameters optimized towards test LT30. The high-velocity FCM profile in Fig. 21 compares favorably to the delamination-free profile obtained by Scott [29] in his thesis, characterized by a less pronounced kink at the elastic-inelastic transition point and a lower peak velocity than what was experimentally obtained. This further indicated the usefulness of a delamination damage mode when modeling GRP behavior to shock loadings. Though matrix microcracking/pulverization occurred in the GRP, the matrix and fibers were held together due to the compressive loading generated from the plate impact. Since the simulated peak velocities matched the elastic Hugoniot predictions given by the Rankine-Hugoniot conditions, it was concluded that nonlinearities in the velocity profiles were the result of microcracking-induced elastic deformation.

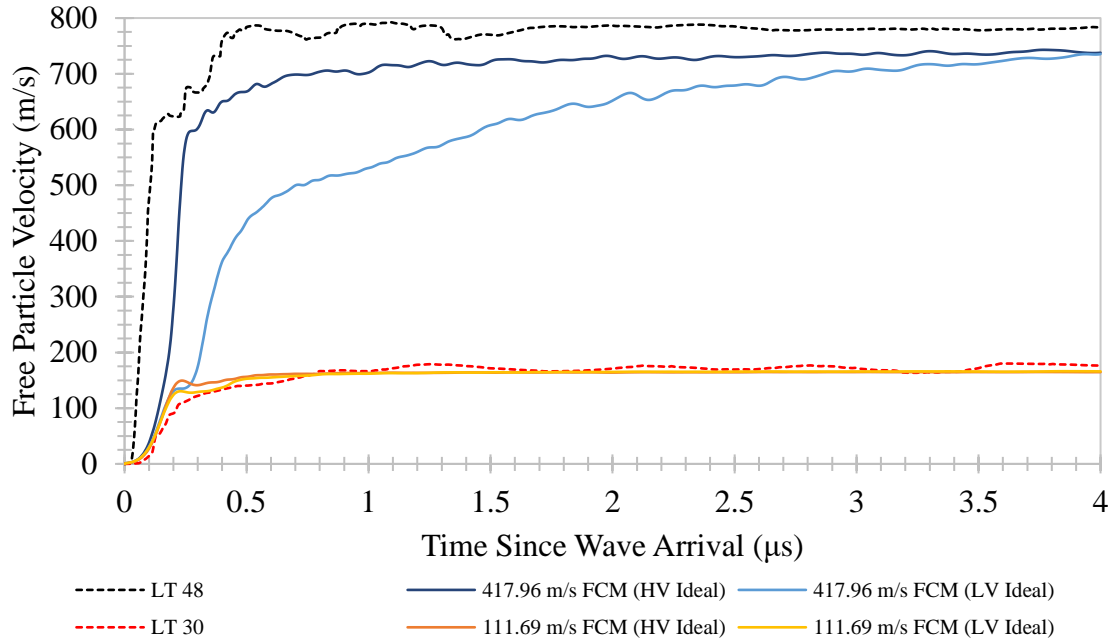


Figure 22. Velocity profile comparison between the FCM calibrated to high-velocity and low-velocity tests

To better understand shock wave propagation through the GRP and explain the velocity profile features seen in Fig. 23, shock stress and damage evolution were investigated for the high-velocity 417.96 m/s impact. Figs. 23 & 24 capture the compressive longitudinal shock stress and matrix damage time history for three different locations (1/4, 1/2, and 3/4 of the GRP thickness away from the impact face). It was observed that as measurements were taken further away from the impact face, the shock stresses at which nonlinearity commenced (highlighted by the three leftmost marks in Fig. 23) gradually reduced. Shock stress will deteriorate in response to matrix damage accumulation, therefore, the decrease in the shock stresses at which nonlinearity commenced possibly indicated that the shock stress at a particular location was affected by prior matrix damage accumulation. By inspecting the calculated matrix damage at the chosen locations, the 3/4 profile should intuitively initiate nonlinearity at higher shock stress than the 1/4 location, owing to its lower damage. However, the opposite is the case, giving rise to this hypothesis. Similar speculation was made in Scott's thesis [29] where it was proposed that the aggregation of prior

matrix damage influenced the timing of particle velocity profile kinks, to which shock stress has a direct relation.

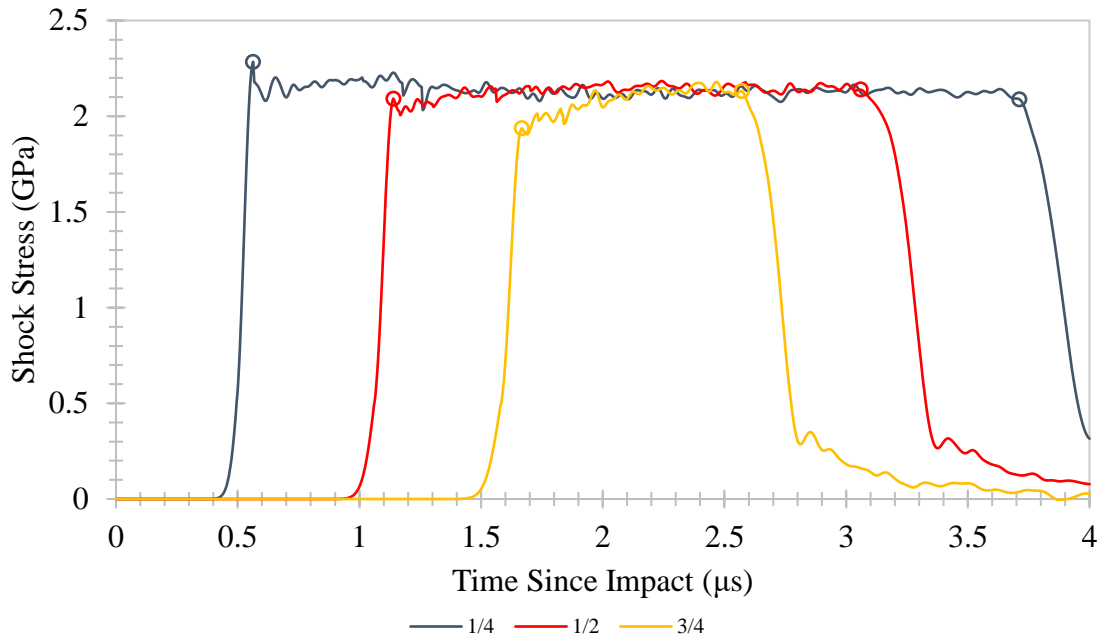


Figure 23. GRP shock stress history at different distances from the impact surface

Analyzing the matrix damage evolution in Fig. 24 confirmed the trend previously mentioned, that as matrix damage accumulated, the shock stress reduced. This is due to the reduction of G and K moduli in the hyperelastic constitutive formulation. At the 1/4 location, where damage accumulation was highest out of the points tested, the shock stress was seen to trend generally negatively between the initial point of damage initiation (circled on Fig. 23) and the final stress point before unloading. At the 1/2 location, the shock stress trended generally level between the two circled marks, and at the 3/4 location, the shock stress trended mildly upwards. Larger deviations from the elastic shock stress profiles were seen at locations closer to the impact face. In addition, the matrix damage evolution explained the varying abruptness of the shock stress reduction at different distances from the impact face. The quicker ramping of matrix damage (seen quickest at the 1/4 mark and slowest at the 3/4 mark) resulted in larger shock stress reduction at

the points of nonlinearity onset. Furthermore, the sharpest damage rise in all three locations, from approximately half the peak value until the peak value, was observed to be caused by a numerical artifact involving how Abaqus called the matrix damage state variable from the previous iteration. Consequently, these spikes did not originate from growth in the matrix damage criteria, which presents an issue that further research efforts are needed to investigate. Generally, the matrix damage present in the FCM simulations was significantly less than the damage reported by Scott [29]. This was likely due to the inclusion of delamination damage in Scott's model, which would have led to vastly different model parameter choices than those selected for the FCM.

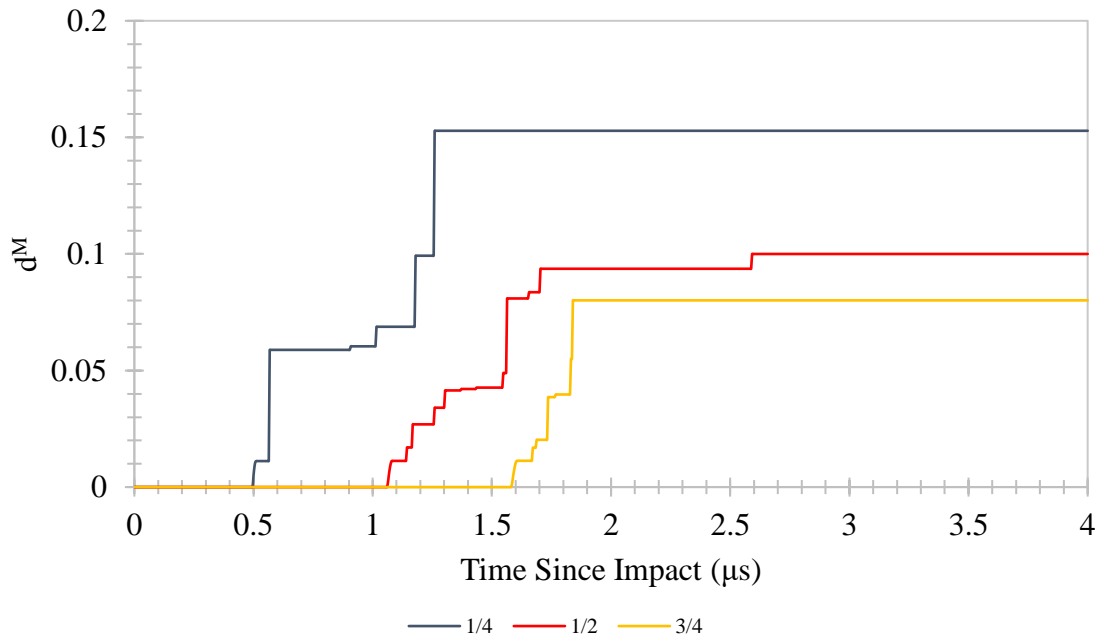


Figure 24. Matrix damage evolution at different distances from the impact surface

To investigate the changes in damage growth rate at the arrival of the wavefront throughout the GRP, contributions of the matrix damage constituents R^{MS} and R^{ME} are compared in Fig. 25. In all locations, the bulk expansion damage instantaneously spiked, peaked at compressive strain J_e^c , then quickly receded as the effects of lateral confinement became apparent. As seen in Fig. 24, the first spike in matrix damage in all locations is relatively equal regardless of location. However,

when the GRP was in compression and compressive strain remained greater than J_e^c , the bulk expansion damage effects were minor compared to the influence of matrix shear damage. For all locations, Fig. 25 shows shear damage exceeded bulk damage after the initial bulk damage spike, indicating all matrix damage growth was the result of shear cracking. At the 1/4 location, the R^{MS} values obtained by the FCM were significantly less than what was reported by Scott et al. [16]. This supports the speculation that greater matrix damage was required to obtain velocity profile matches in their models due to the inclusion of delamination.

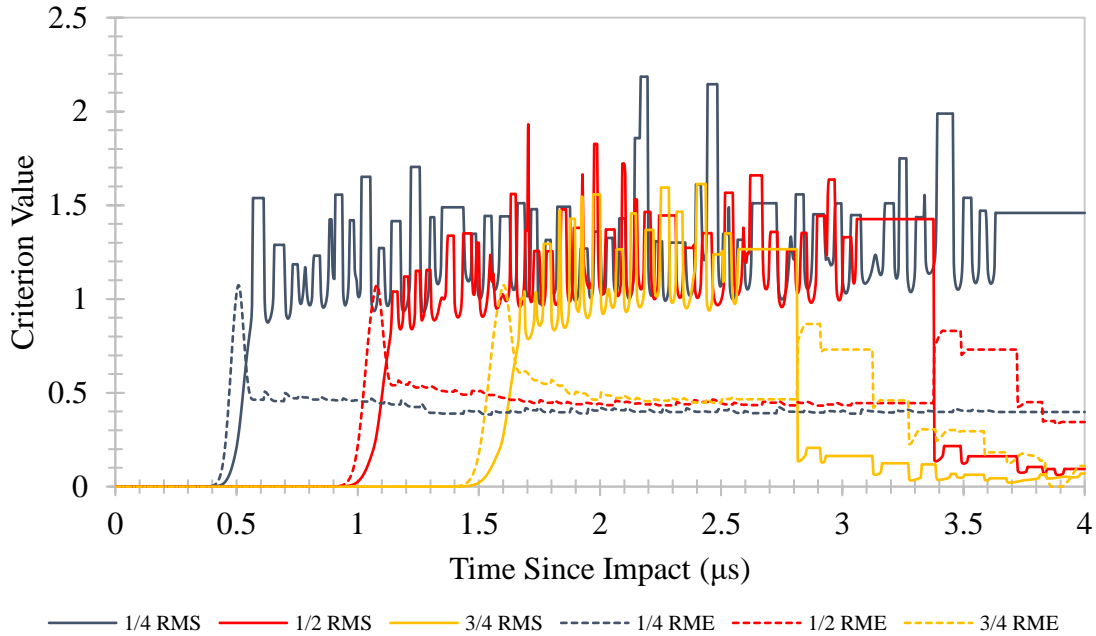


Figure 25. Contributions of shear and bulk matrix damage criteria comparison

Scott et al. [16] observed a gradual increase in lateral shock stress after $2.5 \mu s$ in their simulations, owing to the faster degradation of G relative to K . This behavior could be explained by the relation between lateral and longitudinal shock stress, given by Eq. (54), for an isotropic elastic matrix:

$$\sigma_{lat} = \left(\frac{3K - 2G}{3K + 4G} \right) \sigma_{long} \quad (55)$$

As the ratio G/K approached zero, i.e., G damaged greater and faster than K , σ_{lat} approached σ_{long} . The decoupled nature of their bulk and shear damage contributions enabled G and K to degrade independently of each other. The model used in Fig. 26 was created by decoupling the damage terms in the FCM and modifying damage parameters for the sake of illustration. Denoted by the labels on the graph, such that feature 1 corresponds with feature 1A and so on, there was a clear correlation between sharp growths in G damage and spikes in lateral shock stress. Since the K damage remained largely constant, when G damage increased the ratio G/K decreased, and the prediction from Eq. (55) was validated.

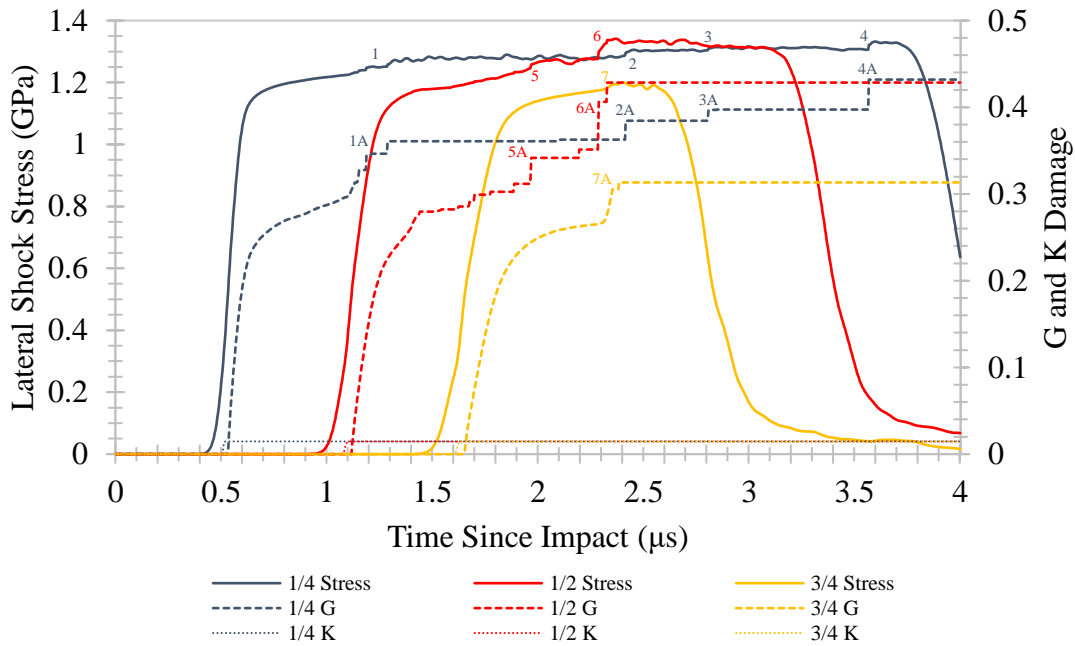


Figure 26. Decoupled damage effect on lateral shock stress

However, due to the coupling of bulk and shear damage as “matrix damage” in the FCM, G and K degraded together. Thus, the G/K ratio remained constant, and lateral shock stress growth was not observed in the present study’s simulations, as seen in Fig. 27. The profile of the lateral shock stress exactly matched the longitudinal shock stress, just at a lower magnitude.

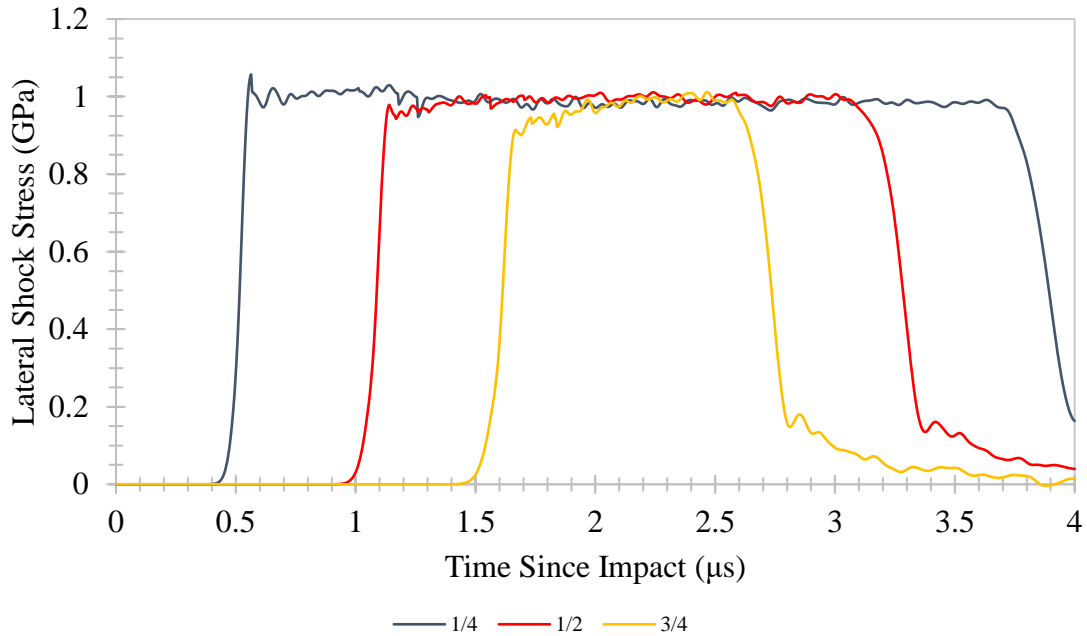


Figure 27. GRP lateral shock stress at different distances from the impact surface

Fig. 28 plots stress against volumetric strain to visualize the degradation of the Hugoniot slope. The theoretical Hugoniot was calculated by Eq. (56) and found to be 19.41 GPa. Calculated from the graph, the intact moduli FCM Hugoniot was 18.55 GPa and degraded to 14.82 GPa as the GRP unloaded.

$$K + \frac{4}{3}G \tag{56}$$

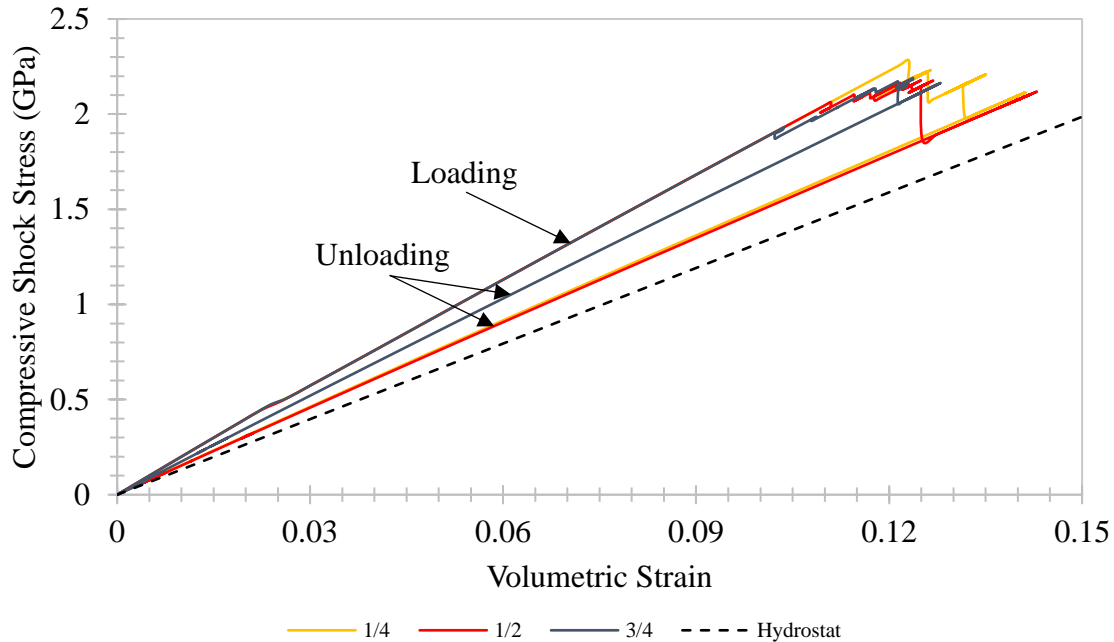


Figure 28. Compressive shock stress evolution in terms of volumetric strain

V.2 BALLISTIC PENETRATION RESULTS

Modeling efforts in this thesis culminated in analyses that explored the evolution of shock and damage propagation in GRP subjected to FSP impacts. These simulations introduced triaxial stress and strain states, which enabled a full representation of the capability of the FCM through the addition of fiber contributions and matrix bulk damage in tension. This section outlines the results obtained using the currently developed FCM while providing insight into how physical phenomena are reflected in data. As a novel effort in this field of hyperelastic CDM-based computational modeling of FRP ballistic impacts, these results act as a preliminary indication of the capability of this model. Future improvements and recommendations that became apparent will be detailed in the following chapter.

V.2.A TENSILE BULK DAMAGE

For the sake of completion, not model calibration, isolating the effect of the tensile bulk damage growth parameter J_e^t was attempted using FSP penetration simulations. The GRP

remained in compression for the time window of interest in plate impact simulations, so this parameter was redundant and not involved in particle velocity profile calibration. The effect of this parameter was analyzed with regard to its effect on projectile DOP. Bulk damage growth in tension is governed by Eq. (22), which indicates that as J_e^t approaches 1 (for $J_e^t > 1$), the bulk damage effect enlarges.

$$R^{ME} = \frac{J - 1}{J_e^t - 1} \quad (22)$$

An array of J_e^t values were trialed for an 800 m/s FSP penetration simulation, the DOP results of which are depicted in Fig. 29. The DOP was not sensitive to changes in J_e^t , however, the behavior of the particle once it reached its maximum depth varied slightly. The issue described in Section III.5.B was apparent in the $J_e^t = 10$ sample, which can be seen by the constant rate of displacement increase after approximately 28 μ s.

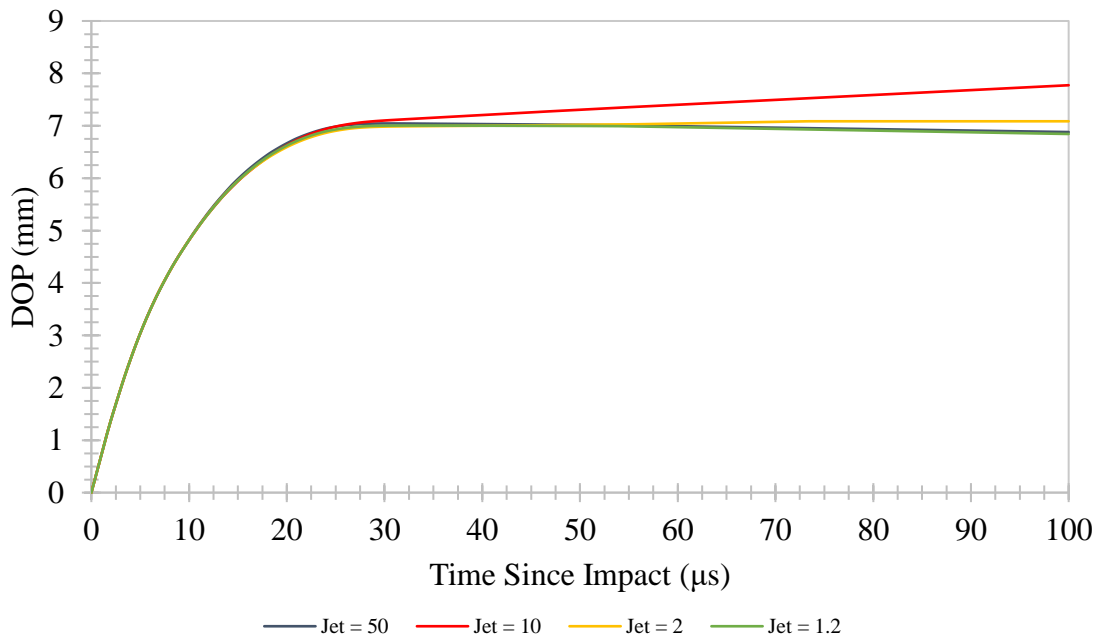


Figure 29. DOP response to J_e^t changes

Intuitively, the DOP should increase as J_e^t decreases, however, this was not observed. The convolution of damage progression in the GRP in the penetration simulations greatly complicated

the isolation of the effect of J_e^t . The complexity of the GRP structure and the behavior of highly-deformed elements meant changes in J_e^t led to unpredictable results and was unsuitable for calibration with regards to DOP matching. J_e^t was arbitrarily set to 2 for the simulations.

V.2.B FIBER BUCKLING STIFFNESS

The buckled fiber stiffness η is, like J_e^t , a user-defined model parameter only applicable to penetration simulations. The uniaxial strain environment created by the plate impact simulations ensured no fiber contributions were possible, thereby making η redundant. For the sake of completion, the effects of η were analyzed with regard to the DOP of an 800 m/s velocity FSP. The results in Fig. 30 did not indicate a clear trend, further suggesting that the complexity of the GRP response and interaction between damage modes made it extremely difficult to capture the effect of one particular parameter. For penetration simulations, η was arbitrarily chosen as 0.8, however, as a physically representative parameter, perhaps future experimental works can determine material-dependent values for η or a strain-dependent evolution of η .

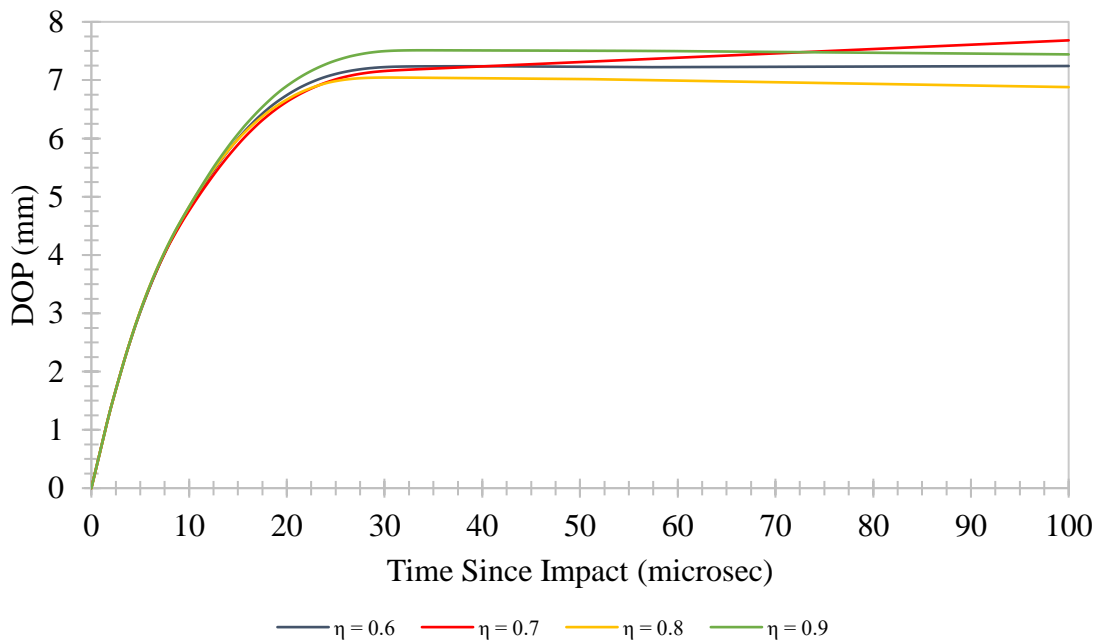


Figure 30. DOP responses to η changes

V.2.C DOP AND REAR BULGE ANALYSIS

One of the preliminary comparisons made with existing experimental data [14] was projectile DOP. This test indicator reflected how accurately GRP degradation was captured in terms of the rate and extent of degradation in the compressive strength of the GRP. As stated in Section III.5.B, issues were encountered with excessive particle conversion occurring in the through-thickness of the GRP for higher-velocity simulations (900 m/s and above) causing projectile perforation when it should not. This issue was likely contributed to by a too coarse discretization of the GRP elements in the thickness direction. Element thicknesses of 4 mm are likely to have over-generalized the extent of damage, limiting the ability of the simulation to correctly localize damage and instead over-allocating it through the GRP thickness. For this reason, simulations were performed on FSP velocities at 100 m/s increments from 400 m/s to 800 in addition to the experimental velocities the FCM did not encounter the perforation issue with. Fig. 31 displays the FCM comparison to experimental DOP results for both FSP calibers.

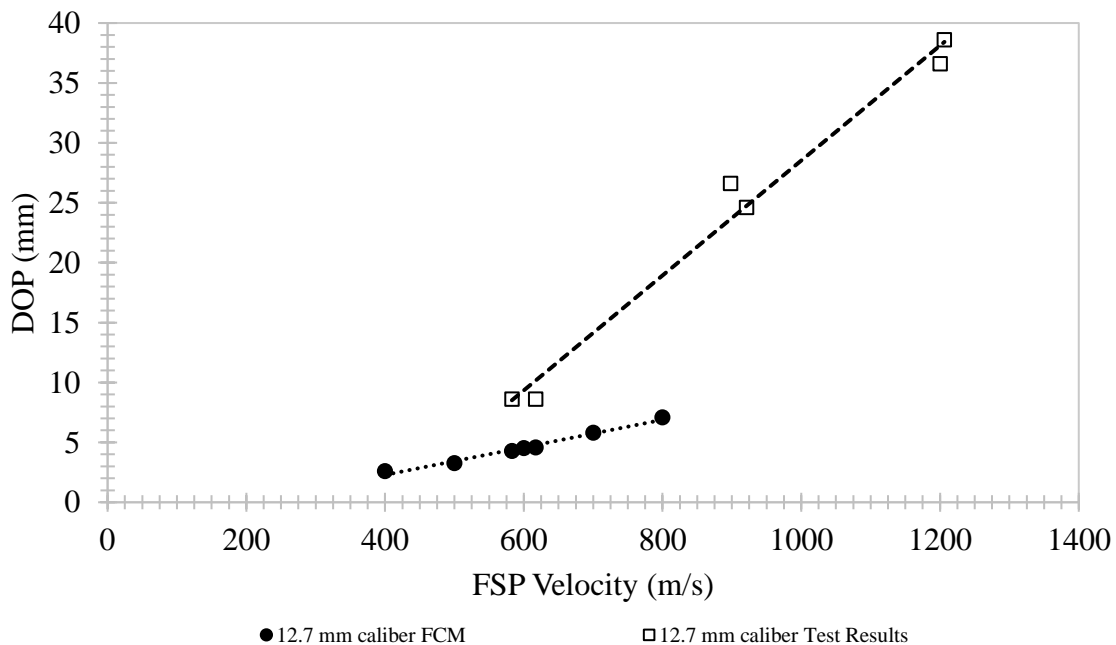


Figure 31. DOP comparison between FCM and experimental test data [14]

FCM results vastly underestimated the experimental DOP, suggesting matrix and fiber degradation parameters did not create enough moduli degradation given the encountered stresses and strains. Following the speculation made regarding the greater presence of matrix damage in Scott's [29] work facilitated by the inclusion of delamination, both greater matrix degradation and an added delamination degradation mode would help lessen the discrepancy between the FCM predictions and experimental findings. Furthermore, the linear trendline slopes of both FCM simulations are significantly less than the experimental results. This is perhaps due to insufficient strain rate dependency, which if increased should increase damage, and hence DOP, by greater amounts as impact velocities increase. As a side note, it is important to separate inadequate GRP damage from the excessive deterioration of the GRP element quality. The author believes that these can be addressed independently, the GRP damage through model parameter selection and the element quality through better computational technique.

A GRP response feature accompanying the DOP was the maximum rear surface displacement, or "bulge height". The extent of the rear surface bulge provided insight into how the FCM transferred the shock loading through the GRP thickness. Fig. 32 compares the FCM to experimental data for the maximum rear surface displacement for the same simulated velocities as the DOP results. The bulge measurements were taken just before observing element deterioration at the rear surface, which led to nodal displacements that were reflective of the numerical artifact as opposed to the actual GRP response. This was typically between 35 and 50 μ s after impact. The rear surface displacement results led to many of the same conclusions as the DOP results, notably that the compressive strength of the GRP did not degrade enough, leading to underestimation of the bulge height compared to experimental data. In addition, the deterioration of the quality of the elements on the rear surface likely led to premature measurement. It was observed that the GRP

had a profound deformation response to the shock impact approximately 50 μ s after the tested 800 m/s impact, which was too late to be captured by the bulge measurements. This delayed deformation will be elaborated on later in this section.

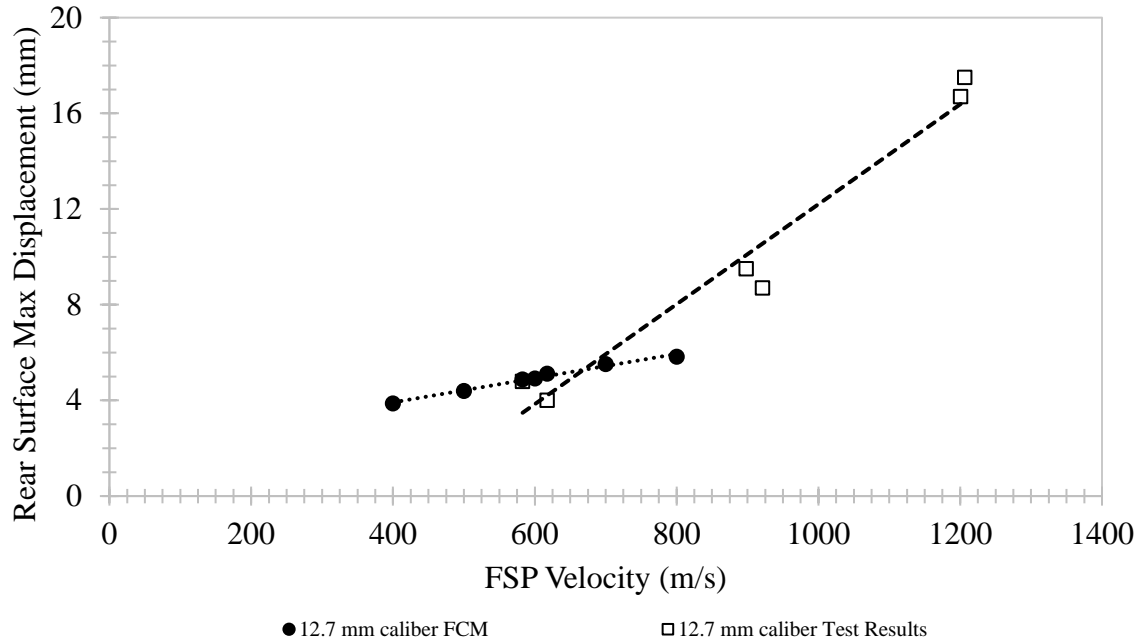


Figure 32. Rear surface displacement comparison between FCM and experimental data [14]

V.2.D STRESS ANALYSIS

To further verify the simulated propagation of shock stress through the GRP, stress profiles were captured at approximately 8 mm and 20 mm depths in the path of the FSP and compared to stress results obtained by Rajendran et al. [15]. Fig. 33 displays the shock stress profiles for a 246 m/s 20 mm caliber, 7.5 mm thick FSP impact at elements at 8-12 mm depth and 16-20 mm depth. Data for four elements, with a footprint of approximately 8 mm x 8 mm centered on the FSP path at the listed depths, were averaged to produce the profile at a given depth seen in the graph. This element averaging attempted to recreate the 6.35 mm x 6.35 mm strain gauge surface.

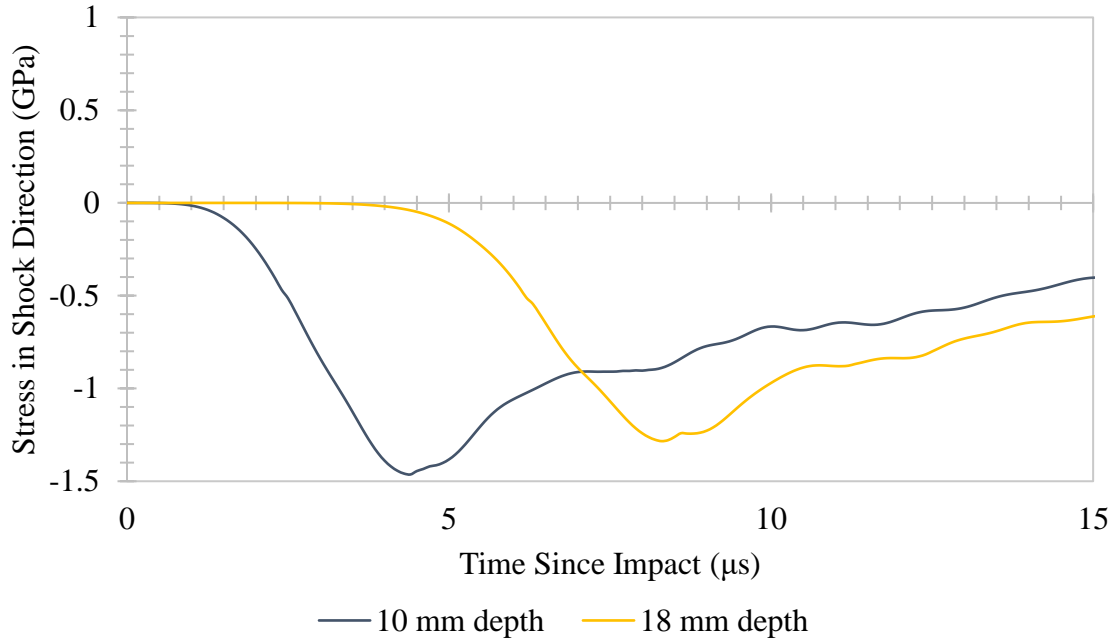


Figure 33. Stress in shock direction evolution at different GRP depths

The profiles obtained in the simulations were analyzed with a focus on theoretical compressive and tensile wave arrival times, peak longitudinal shock stress, and stress attenuation behavior. The theoretical arrival times obtained using the GRP longitudinal wave speed of 3.2 mm/ μ s reported by Tsai et al. [11], and Abaqus predicted arrival times are summarized in Table 13.

Table 13. Compressive and tensile wave arrival times [11]

Approx. Depth (mm)	Compressive Wave		Tensile Wave	
	Theoretical	Abaqus	Theoretical	Abaqus
10	3.13	0.9	4.4	4.3
18	5.63	3.5	6.4	8.3

At both depths, the compressive wave arrival times in Abaqus simulations were quicker than expected. This was understood to be due to a too coarse mesh discretization speeding up the wave propagation. The compressive stress unloading was caused by the arrival of spherical tensile waves originating from the edge of the impact face of the FSP at the time of impact. Since these waves radiate from a location further away from the measured elements, the theoretical arrival times of the spherical tensile waves are later than the compressive waves. A better experimental agreement

was shown in the simulations. In addition to wave arrival time analysis, a comparison of peak compressive stresses with strain gauge measurements from Rajendran et al. [15] is presented in Table 14. Both simulated stress results fell within the range of the strain gauge values, and compressive stress attenuation behavior was observed, albeit significantly less than the experimental data. The low attenuation was attributed to inadequate GRP damage, which did not allow the GRP to dissipate enough shock stress through the creation of deformation.

Table 14. Peak compressive shock stress comparison [15]

Approx. Depth (mm)	Experimental (GPa)	Simulated (GPa)
10	1.7	1.29
18	0.9	1.23

To gather information about the GRP response in the shock direction and laterally, data was taken at GRP depths of 5 mm, 10 mm, 20 mm, and 30 mm from the impact surface. Two element sets were created, one in the pathway of the FSP (the “centered” element set) and one 30 mm radially distant from the FSP center (the “radial” element set) located on the x-axis. Figs. 34 and 35 compare stress in the shock direction at the “centered” and “radial” element sets.

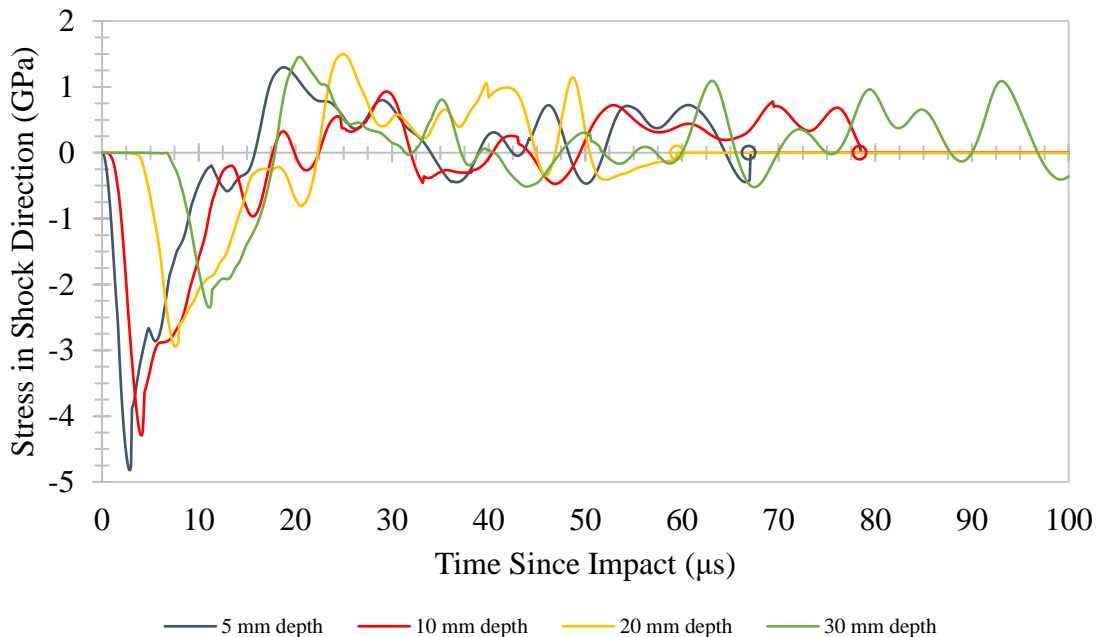


Figure 34. "Centered" element set shock stress time history

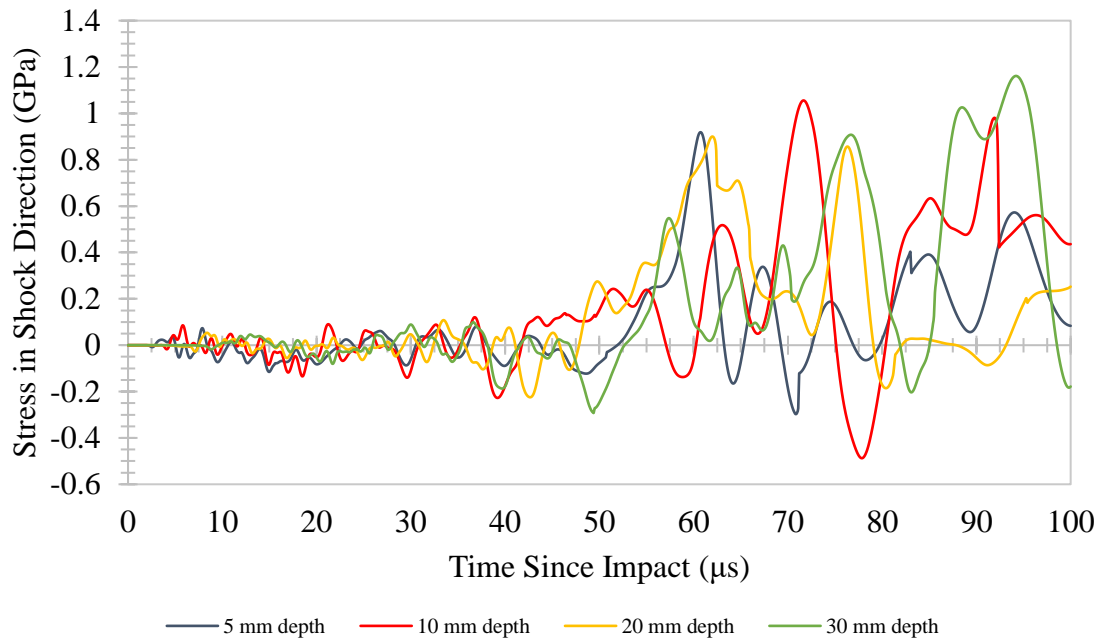


Figure 35. "Radial" element set shock stress time history

As expected, initially the compressive shock stress was large in the “centered” elements in the direct path of the shock wave, while the “radial” elements were further away from the compressive shock wave initiation site and hence subjected to much lower stress levels. The dissipation of stress due to the travel distance to the “radial” elements was clear. Compressive stress attenuation was evident in the “centered” element plots by the reduction in stress peaks during the first 11 μs. In the “radial” elements, a period of ringing consisting of four reverberations through the GRP thickness precedes a period of steady-state penetration response after approximately 50 μs. During the ringing period, the stresses and strains from the initial shock equilibrate, as observed in the “centered” elements. This initial influx of energy dissipated as strains and deformation were developed. Profound growth and tensile stress oscillation characterized the “radial” element response after 50 μs, while in the “centered” elements, particle conversion commenced after 60 μs (see marked circles in Fig. 34) at the 20 mm depth, followed by 67 μs at 5 mm depth, and 78 μs at

10 mm depth. The absence of stress spikes preceding these moments indicated that these three elements likely eroded due to gradual large deformation in the surrounding elements.

Analyzing lateral stress propagation yielded insight into the stress response involved in triggering fiber failure. Figs. 36 and 37 depict lateral stress (along the x-axis) evolution in the two studied element sets. The magnitude of lateral stress present in the “centered” elements is almost double that seen in the “radial” elements, illustrating the effect of travel distance through material on the dissipation of the stress wave as it creates deformation. Furthermore, the 10 mm depth for the “centered” set was a region of tensile wave concentration, suggesting the tensile wave origination was an ideal distance away from the 10 mm element to produce some superposition effect.

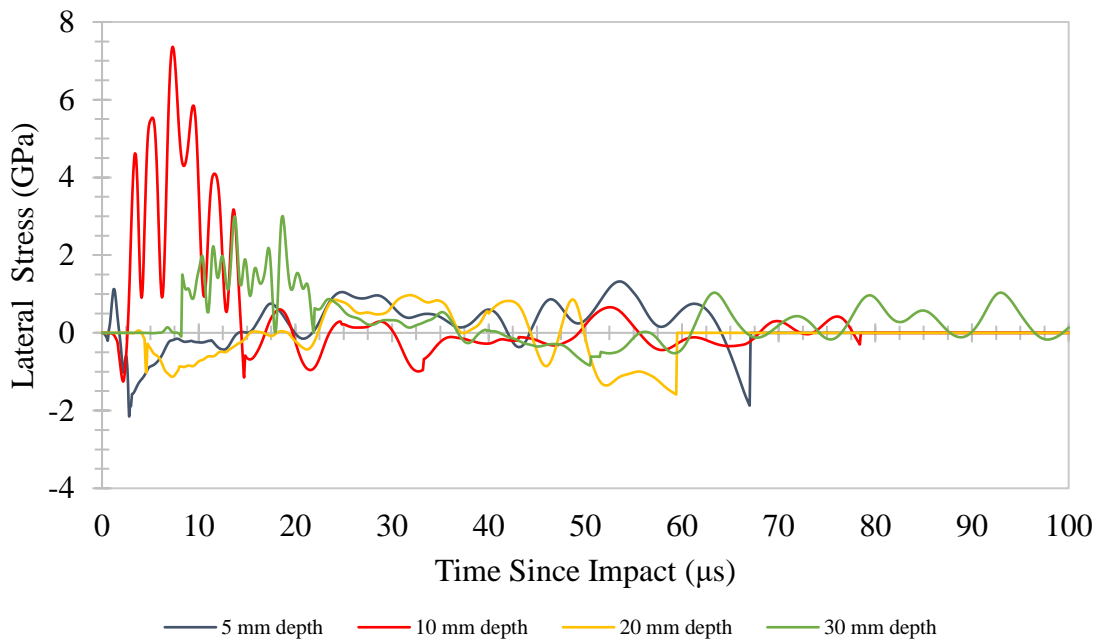


Figure 36. "Centered" element set lateral stress time history

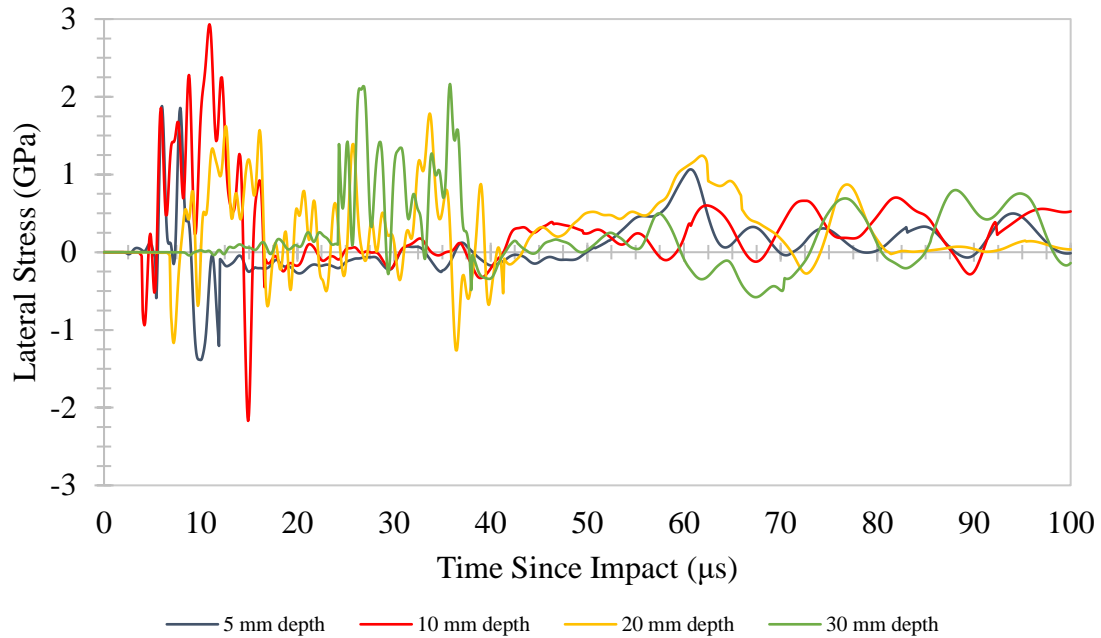


Figure 37. "Radial" element set lateral stress time history

V.2.E STRAIN ANALYSIS

Strain developments in the shock direction for the “centered” and “radial” element sets accompany the stress results in Figs. 34 and 35. It was discovered that the strain condition that triggered the particle conversion was the maximum absolute principal logarithmic strain, plotted in Fig. 38. This graph represents the largest value when the absolute values of all principal logarithmic strains are compared. Particle conversion was observed to initiate slightly prematurely; the Abaqus condition required a “maximum absolute principal strain” (Abaqus documentation does not mention if this meant nominal or logarithmic) of 1 to initiate, yet the maximum logarithmic strains in the observed elements were between 0.947 and 0.993 when the conversion was triggered. This is believed to be the result of numerical artifacts during analysis.

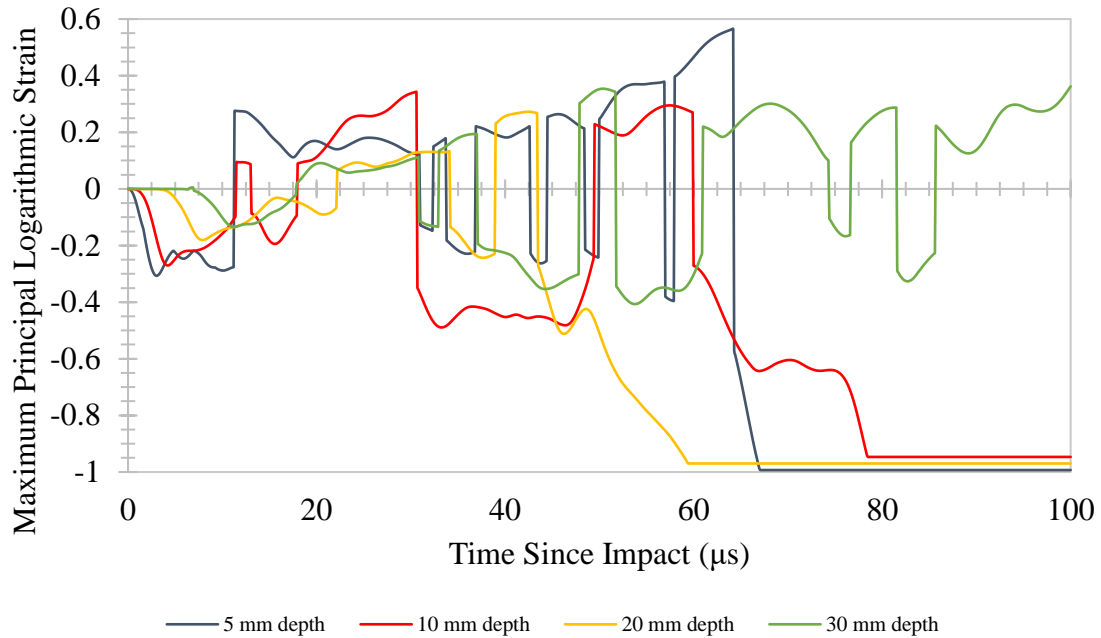


Figure 38. "Centered" element set maximum principal logarithmic strain time history

For a better physical representation, the shock direction nominal strain evolution is given in Fig. 39 for the “centered” elements and Fig. 40 for the “radial” elements. Fig. 39 shows that approximately 60% compression triggered particle conversion at the 5 mm and 20 mm depth “centered” elements. This reinforced the speculation of premature particle conversion causing perforation in the GRP since there was still 40% more compression available for elements to provide stiffness and resistance to FSP travel. The strain behavior in Fig. 39 resembles the stress history in Fig. 34 for the first 50 μs, after which the steady-state penetration state caused large deformation and eventual element erosion. There was no clear relation between element depth and the type of strain growth (tensile or compressive) after 50 μs, indicating the complex structure of the GRP contributed to chaotic deformation behavior. Shock direction strains in the “radial” elements were low until the 50 μs stage, indicating the elements away from the direct path of the FSP were minimally deformed. Like in the “centered” elements, no trend was observed relating

element depth to the type or magnitude of strain once the steady-state penetration stage commenced.

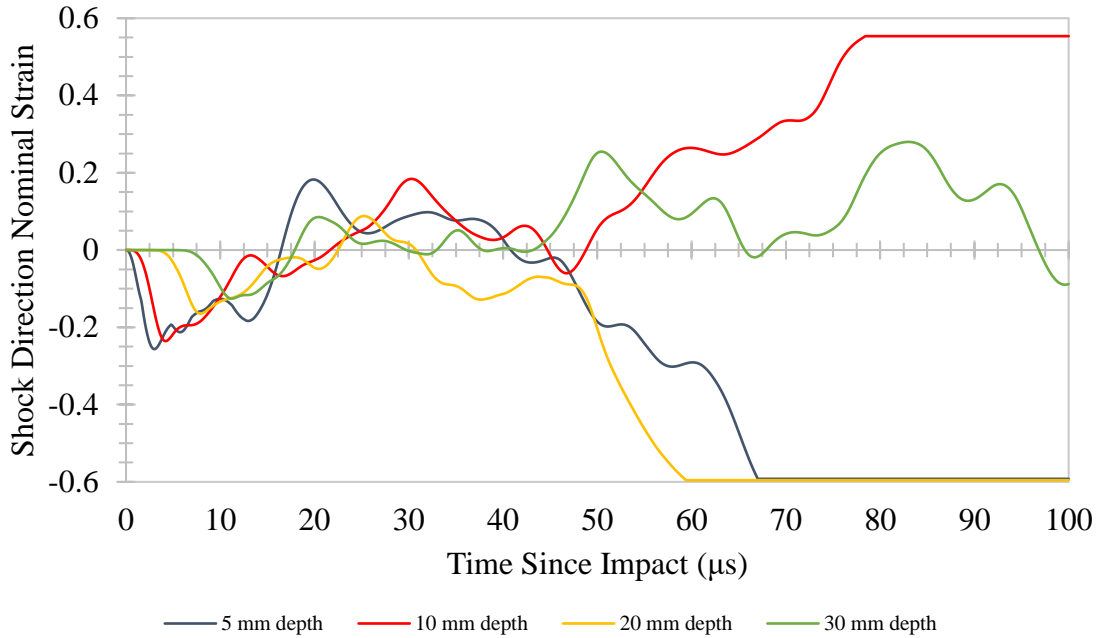


Figure 39. "Centered" element set nominal strain in shock direction time history

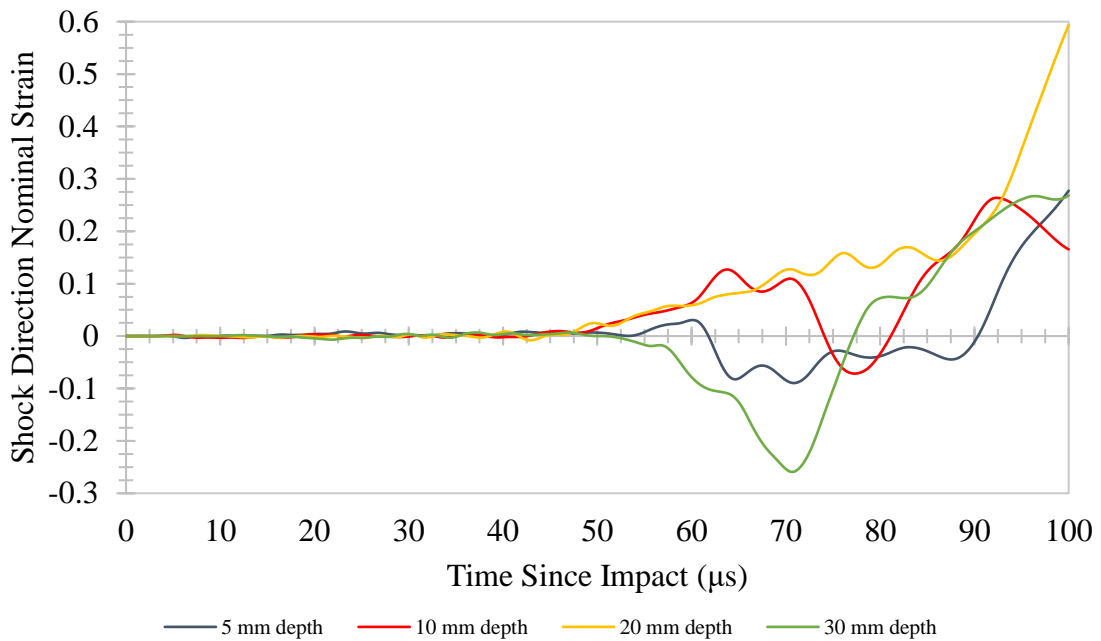


Figure 40. "Radial" element set nominal strain in shock direction time history

The “absolute value” nature of the threshold strain meant critical strains were different depending on if the strain was compressive or tensile. As an example, if the maximum absolute principal logarithmic strain threshold was set to 1, the critical nominal compressive strain according to Eq. (57) is -0.63, while the critical nominal tensile strain is 1.72.

$$\epsilon_{\text{nom}} = e^{\epsilon_{\text{log}}} - 1 \quad (57)$$

Adjustment of the threshold maximum absolute principal strain for particle conversion was attempted to raise the compression strain threshold to 99%, however, doing so sacrificed element integrity in tension (permitting tensile strains up to 9800%) and worse results were obtained (Fig. 41). Developing reasoning for the observed inconsistency of strain levels when particle conversion occurred in Fig. 41 (and minorly in Fig. 38) is left for future work to better understand how to harness the Abaqus particle conversion feature.

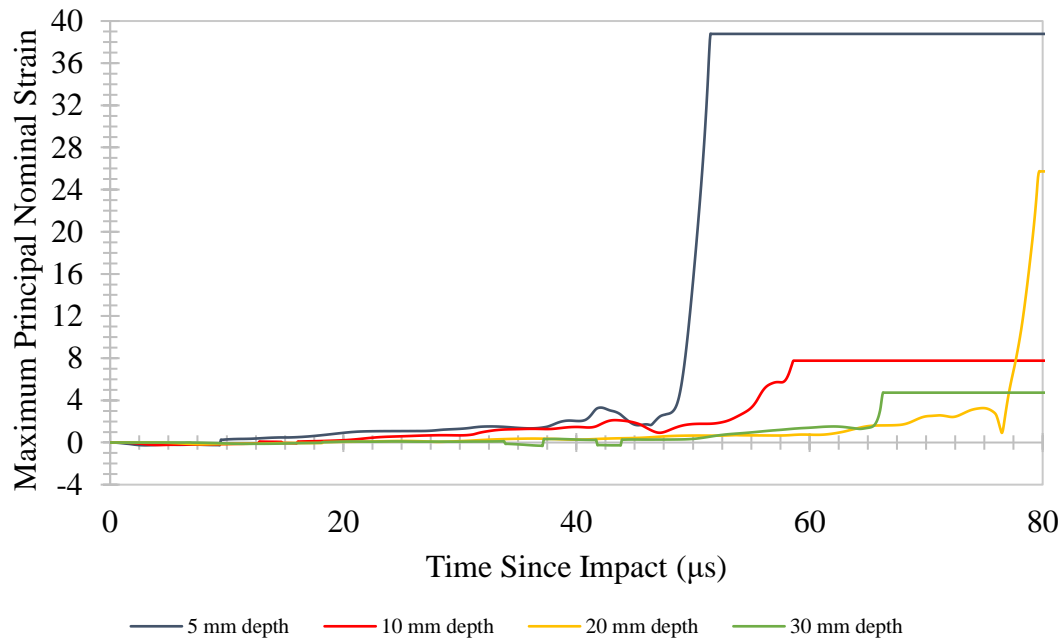


Figure 41. "Centered" element set maximum principal nominal strain with particle conversion threshold = 4.6

Analysis of lateral strain on the “centered” and “radial” element sets was key to interpreting the formation and development of fiber damage. Compared to the strain profiles in Figs. 39 and

40, the signs of the lateral (x-direction) strains in Figs. 42 and 43 were mostly reversed at each depth once the period of large deformation arrived at 50 μs , which makes physical sense if elements are examined through the lens of the Poisson's effect; longitudinal compression should correspond with transverse tension and vice versa. Higher lateral strains in both tension and compression for the "centered" elements suggest fiber damage is likely higher in this location compared to the "radial" elements. This is confirmed later in this section.

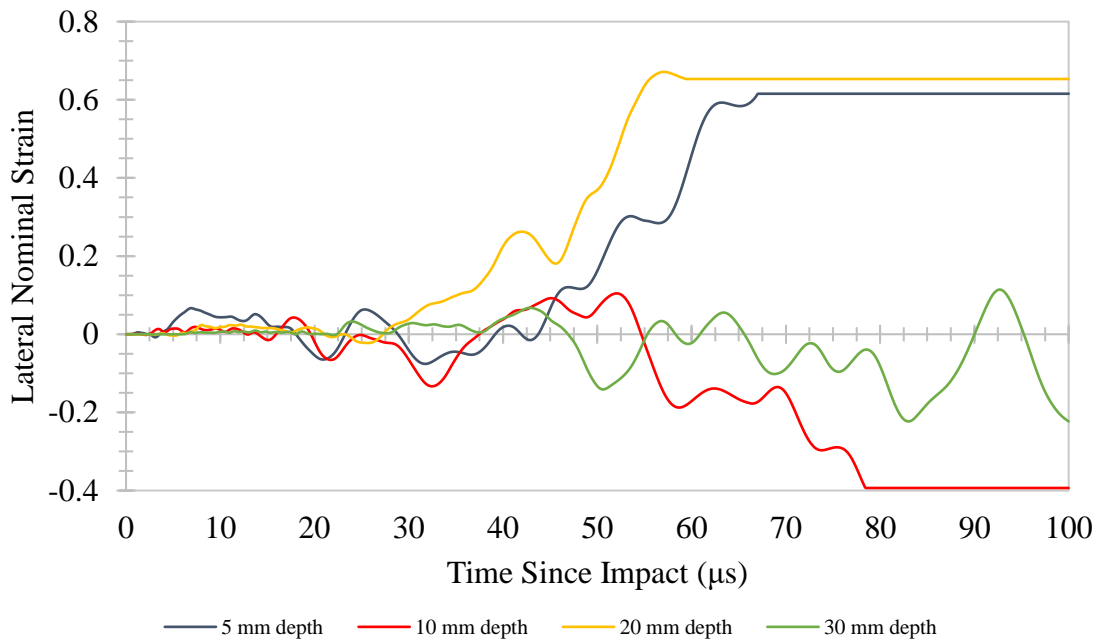


Figure 42. "Centered" element set lateral (x-direction) nominal strain time history

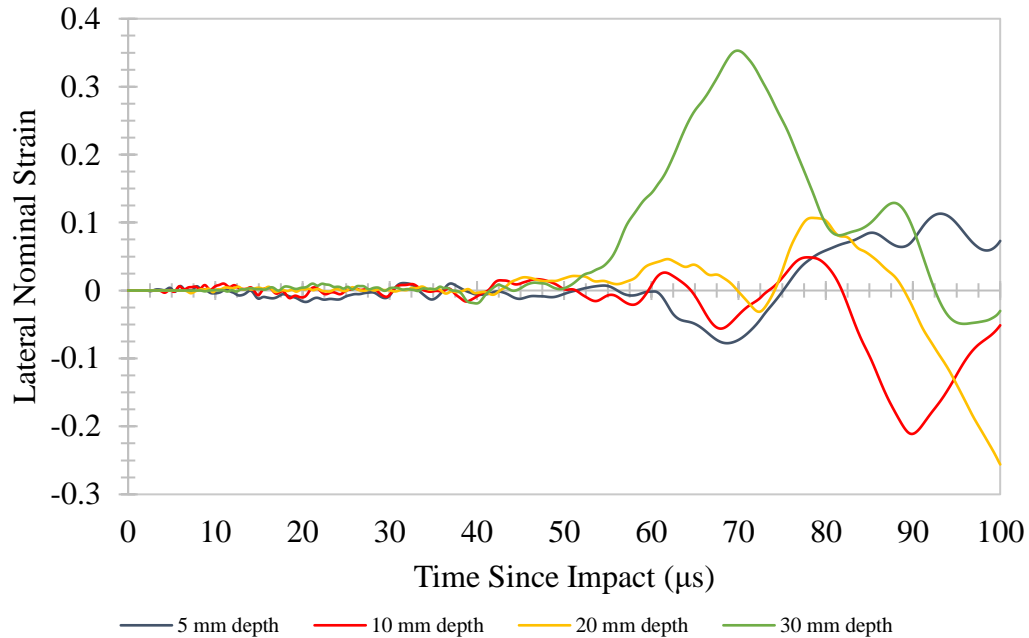


Figure 43. "Radial" element set lateral (x-direction) nominal strain time history

V.2.F FIBER AND MATRIX DAMAGE

It was necessary to first understand the stress and strain response throughout the GRP before analyzing how and when damage developed since the fiber and matrix damage criteria used in the FCM were both dependent on strain. Fiber and matrix damage were analyzed together in the “centered” and “radial” sets to 1) confirm the VUMAT code captured the criteria and conditions defined in the FCM, and 2) observe what the dominant damage modes are and how they evolve at different locations throughout the GRP thickness and laterally distant from impact. Figs. 44 and 45 illustrate the fiber damage and matrix damage progression over time and confirm the implementation of the relations outlined in Eq. (31).

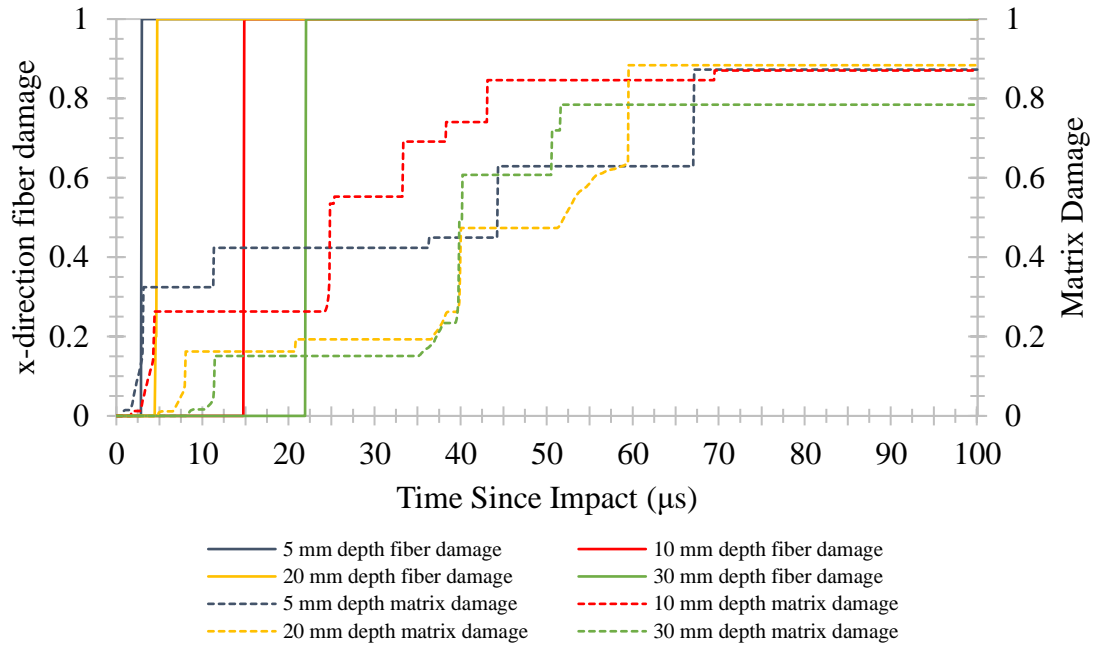


Figure 44. "Centered" element set fiber and matrix damage time history

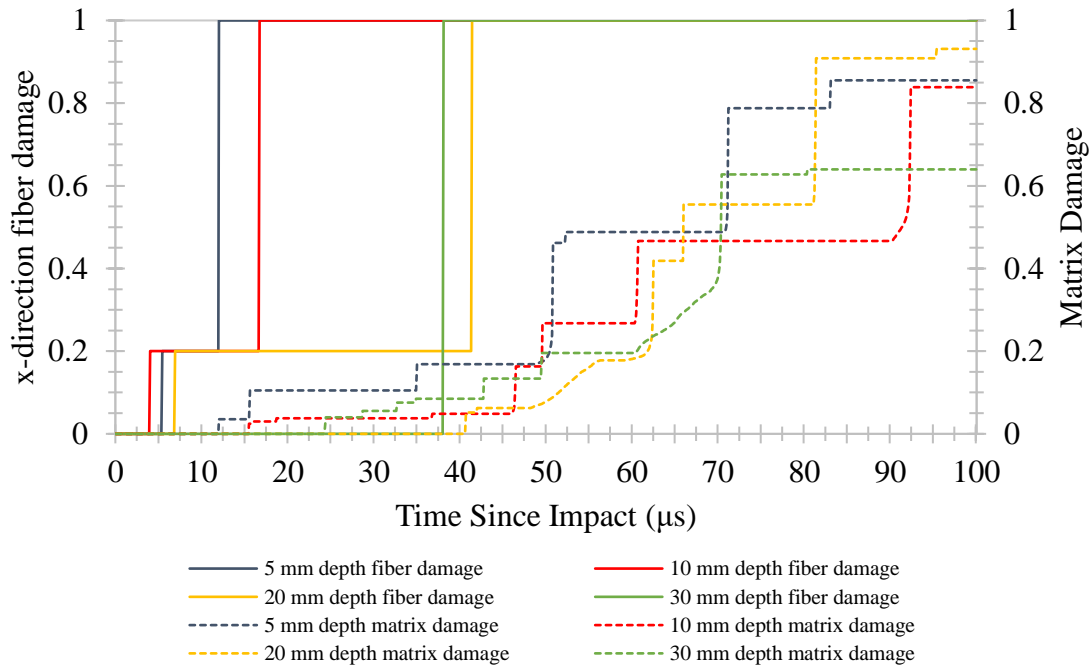


Figure 45. "Radial" element set fiber and matrix damage time history

While the matrix damage initiated sooner closer to the impact surface, this was not observed for fiber damage onset. Instantaneous non-zero matrix damage at all elements in the “centered” set ensured that once the critical fiber compressive strain was exceeded, the x-axis oriented fibers

suffered an instantaneous total failure. This was the fiber damage initiation mechanism observed in both “centered” and “radial” element sets, meaning the lateral propagation of the compressive shock wave was most responsible for fiber damage onset. This behavior was not intuitive and indicated that perhaps the allocated critical fiber compressive strain was too little (the assumed fiber slenderness ratio was too high). Reinforcing this, Table 15 summarizes the times at which the fiber damage criteria R^{fit} and R^{fic} exceeded 1.

Table 15. Fiber damage onsets determined from R^{fit} and R^{fic}

Depth (mm)	"Centered" Element Set		"Radial" Element Set	
	Tensile Damage Onset Time (μ s)	Compressive Damage Onset Time (μ s)	Tensile Damage Onset Time (μ s)	Compressive Damage Onset Time (μ s)
5	4.9	2.9	53.2	4.0
10	16.9	14.8	45.9	5.4
20	29.4	4.5	45.5	6.9
30	23.5	22.0	51.9	38.1

A visual illustration of the fiber damage and matrix damage growth within the GRP was extracted from Abaqus results through the means of contour plots. Figs. 46 and 47 depict matrix damage and fiber damage (in the x-direction) respectively, at different through-thicknesses and at different elapsed times. Matrix damage was observed to be more isotropic as the middle of the GRP thickness was approached, and most anisotropic on the front and rear surfaces. The widest extent of damage was also present on the rear surface due to the spherical propagation of tensile waves emanating from the impact area. Fiber damage in the x-direction was more prominent along the x-axis compared to the y-axis, which was expected due to the domination of the compressive shock wave causing compressive failure in the x-direction and less tensile failure in the y-direction.

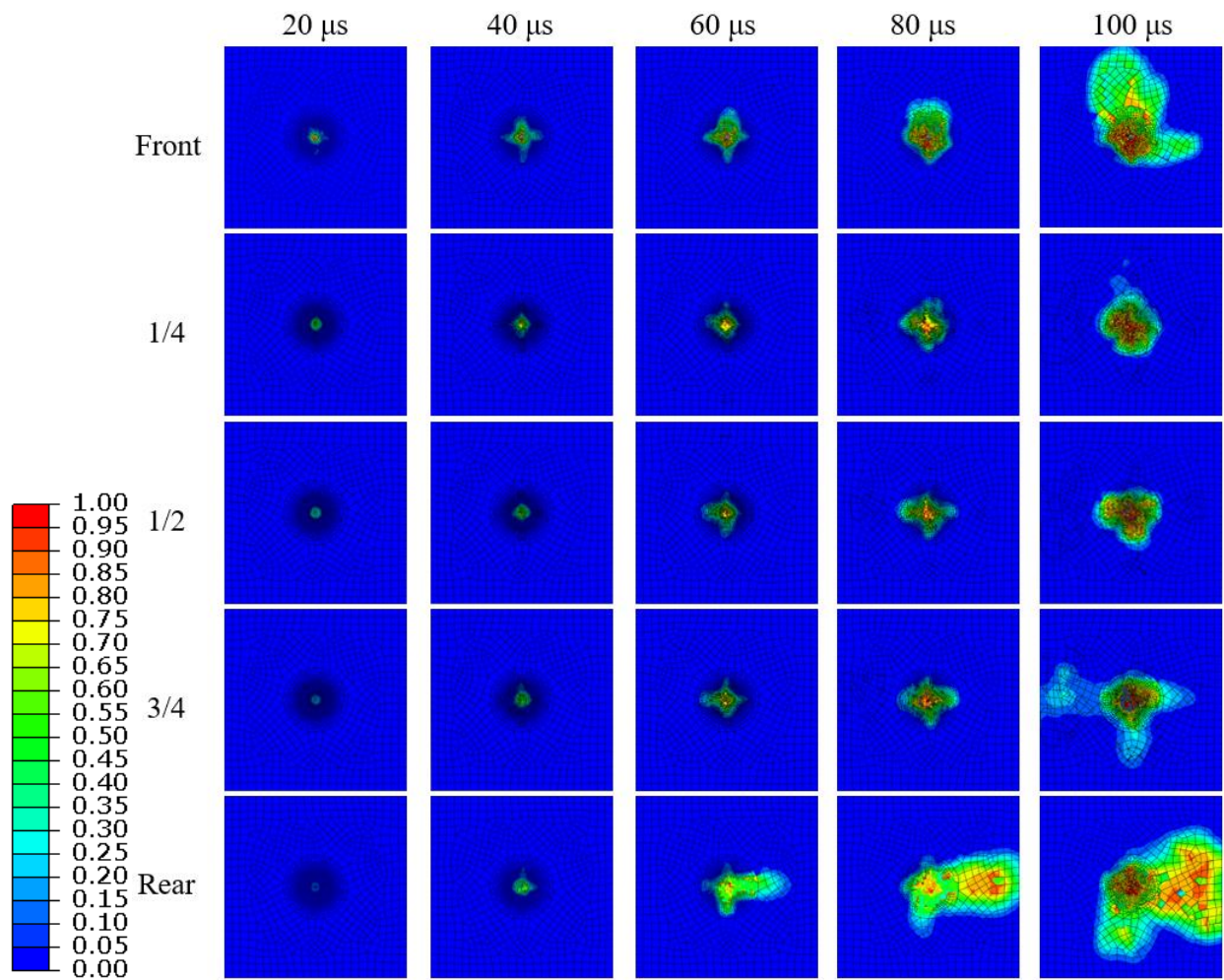


Figure 46. Matrix damage progression contours: rows represent the position on or through the GRP thickness, columns represent time stamps

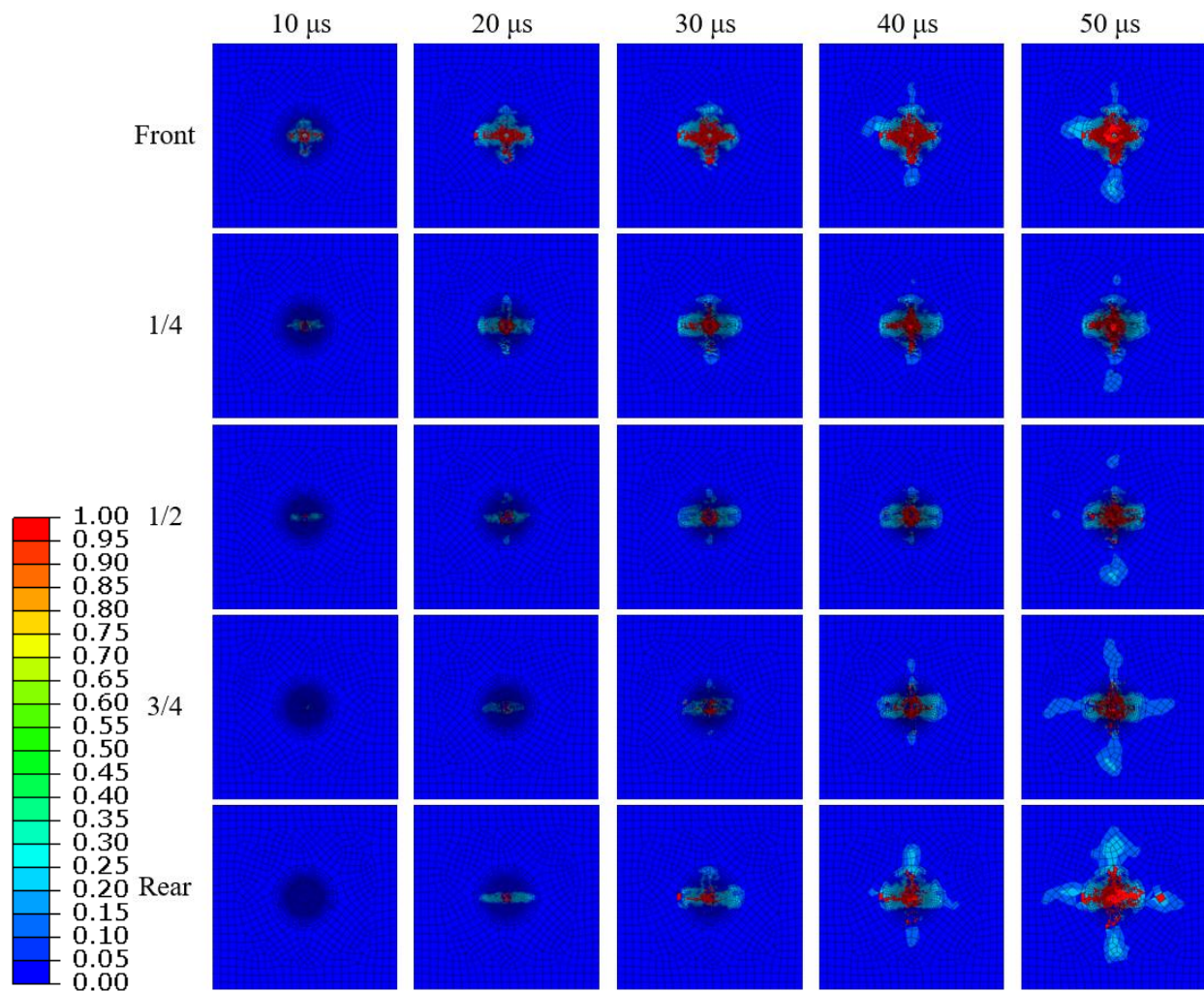


Figure 47. Fiber damage progression contours: rows represent the position on or through the GRP thickness, columns represent time stamps

CHAPTER VI

SUMMARY

A continuum damage mechanics-based constitutive equation derived from an empirical Helmholtz free energy expression from open literature was implemented in the commercially available Abaqus finite element software through a VUMAT subroutine. This model, referred to as the FCM, was suitable for describing anisotropic effects due to fiber orientations in a GRP. The nonlinear elastic stress-strain response was obtained from the gradients of the Helmholtz free energy function. Damage initiation due to matrix microcracking under both tension and compression loading was modeled using a simple critical strain-based criterion. The critical strains at damage initiation were considered to be material properties. The FCM described three types of critical strain conditions to initiate fiber damage in the x- and y- directions: buckling, breakage under tension, and breakage under compression. Since the Abaqus simulation considered a solid GRP without any ply interfaces, a delamination failure mode was not modeled in the present work.

The validation and verification of the model implementation in Abaqus considered simulations of two different shock and impact experimental configurations: a thick metal plate impacting a thin GRP plate and a projectile penetration into a thick GRP target. A VISAR apparatus measured free surface particle velocity in the plate impact test, while computational tomography scans were used to visualize depth of penetration (DOP) in the ballistic test. In addition to the DOP data, rear surface displacement (bulging), and internal stress measurements of the thick GRP plate were also utilized in the model validation.

In the determination of model parameters, wherever possible, the critical strains for various failure modes were estimated or calibrated using experimental data from open literature. The model constants that lacked experimentally-determined values were calibrated by trial and error by matching Abaqus FCM results with VISAR-measured particle velocity profiles [11]. For all calibrated parameters, an extensive sensitivity study was performed to evaluate the influence of such parameters on the time evolution of stress/strain and free surface velocity. The best possible matching was obtained using data from Test LT48 in which a 25.4 mm thick D7 Tool Steel flyer impacted a thin 6.8 mm GRP at 418 m/s. Using the calibrated set of constants, the velocity profiles from Test LT30 (112 m/s) and Test LT31 (313 m/s) were compared both qualitatively and quantitatively with the Abaqus-obtained FCM profiles. The observed salient features, such as the initial ramping of the velocity, peak velocity, and the elastic-elastic-cracking (EEC) bifurcation points in the three experimental profiles compared well.

To further validate the Abaqus VUMAT implementation of the FCM, an earnest attempt was made to predict the DOP and the bulging in the ballistic penetration test for various projectile (FSP) velocities using the same set of model parameters determined from the shock wave experiments. The effect on DOP results due to numerical artifacts such as unoptimized mesh size, restrictions enforced by particle conversion, and element erosion, was studied through Abaqus simulations of the ballistic tests at different velocities. While matrix damage was the sole contributor to plate impact shock wave propagation results, fiber damage was an important factor, as expected, in influencing the DOP and the free surface motion in the ballistic tests. Matrix failure was dominant in both the impact and rear surfaces of the GRP, as well as the region in the path of

FSP travel during the characteristic time (less than 10 μs) of shock wave propagations. However, after about 4 to 5 reverberations of the initial shock and release waves through the GRP thickness (~ 44 mm), a steady-state penetration of the FSP was reached during characteristic times above 50 μs . In general, the matrix damage parameters in the model were found to be too strict to enable adequate damage growth, a consequence of which was too shallow DOP and rear surface displacement. Fibers about 2 FSP diameters radially away from the central line of penetration were observed to break due to compressive stresses overloading the fibers without an intact matrix to provide adequate support. This was counter to what was expected and was deduced to be the result of a too-strict assumed critical compressive fiber strain. Like matrix damage, fiber damage was concentrated around the impact and free surfaces of the GRP, and clearly propagated along the x- and y-axis fiber directions.

The Abaqus solutions to the ballistic configuration were greatly influenced by both model parameters and numerical artifacts inherent to finite element codes. The current work revealed that the DOP results were only minorly sensitive to the fiber/matrix damage parameters. The influence of mesh size and particle conversion clouded and restrained the modeling efforts.

All analyses and simulations performed represented the current capabilities of the FCM, however, multiple areas with room for development became apparent while the model was being built and tested. Future inclusion of a delamination damage criterion should be a critical step in progressing the model to become as physically representative as possible, while also enabling relaxation of the matrix damage parameters to facilitate greater damage growth. Furthermore, developing a strain-dependent expression for the buckled fiber stiffness η would improve the

realism of the currently-employed criterion. Extensive efforts also need to be made towards learning how to harness the Abaqus particle conversion feature (or other element distortion control methods), as well as in mesh size optimization and state variable understanding, to minimize the influence of numerical artifacts when obtaining results. Unfortunately, to accurately model the penetration resistance of GRP, the mesh resolution would require uniform mesh of the order of fiber bundle diameter throughout the GRP target, leading to over hundreds of millions of elements. It is possible to perform scalable high-performance computing of the depth of penetration process by a projectile into a thick GRP in supercomputers.

BIBLIOGRAPHY

BIBLIOGRAPHY

- [1] J.-K. Kim and M.-L. Sham, "Impact and delamination failure of woven-fabric composites," *Composites Science and Technology*, vol. 60, no. 5, pp. 745–761, Apr. 2000, doi: 10.1016/S0266-3538(99)00166-9.
- [2] N. Razali, M. T. H. Sultan, F. Mustapha, N. Yidris, and M. R. Ishak, "Impact Damage on Composite Structures – A Review," p. 13.
- [3] G. A. O. Davies, D. Hitchings, and G. Zhou, "Impact damage and residual strengths of woven fabric glass/polyester laminates," *Composites Part A: Applied Science and Manufacturing*, vol. 27, no. 12, pp. 1147–1156, 1996, doi: 10.1016/1359-835X(96)00083-8.
- [4] A. W. Abdel-Ghany, I. Taha, and S. J. Ebeid, "Failure Prediction of Fiber Reinforced Polymer Pipes using FEA," vol. 4, no. 2, p. 6, 2016.
- [5] C. Soutis, N. A. Fleck, and P. A. Smith, "Failure Prediction Technique for Compression Loaded Carbon Fibre-Epoxy Laminate with Open Holes:," *Journal of Composite Materials*, Jul. 2016, doi: 10.1177/002199839102501106.
- [6] M. Altin Karataş and H. Gökkaya, "A review on machinability of carbon fiber reinforced polymer (CFRP) and glass fiber reinforced polymer (GFRP) composite materials," *Defence Technology*, vol. 14, no. 4, pp. 318–326, Aug. 2018, doi: 10.1016/j.dt.2018.02.001.
- [7] A. M. Abrão, P. E. Faria, J. C. C. Rubio, P. Reis, and J. P. Davim, "Drilling of fiber reinforced plastics: A review," *Journal of Materials Processing Technology*, vol. 186, no. 1, pp. 1–7, May 2007, doi: 10.1016/j.jmatprotec.2006.11.146.
- [8] L. Signor, E. Lescoute, D. Loison, T. de Resseguier, and A. Dragon, "Experimental study of dynamic fragmentation of shockloaded metals below and above melting," *EPJ Web of Conferences*, vol. 6, Jul. 2010, doi: 10.1051/epjconf/20100639012.
- [9] A. D. Resnyansky, "Establishment of a VISAR Measurement System for Material Model Validation in DSTO," p. 38.
- [10] M. Elamin and J. Varga, "Plate impact method for shock physics testing," *MSEIJ*, vol. 4, no. 1, 2020, doi: 10.15406/mseij.2020.04.00123.
- [11] L. Tsai, F. Yuan, V. Prakash, and D. P. Dandekar, "Shock compression behavior of a S2-glass fiber reinforced polymer composite," *Journal of Applied Physics*, vol. 105, no. 9, p. 093526, May 2009, doi: 10.1063/1.3124622.
- [12] M. I. Barham, M. J. King, G. Mseis, and D. R. Faux, "Hyperelastic Fiber-Reinforced Composite Model with Damage." Lawrence Livermore National Laboratory, 2013.
- [13] "ALE3D | Weapons and Complex Integration." <https://wci.llnl.gov/simulation/computer-codes/ale3d> (accessed Apr. 07, 2022).
- [14] J. Prifti, E. DeLuca, W. Bethoney, and S.-C. Chou, "Dynamic Response of S-2 Glass Reinforced Plastic Structural Armor," ARMY RESEARCH LAB WATERTOWN MA MATERIALS DIRECTORATE, Dec. 1993. Accessed: Mar. 09, 2022. [Online]. Available: <https://apps.dtic.mil/sti/citations/ADA273868>

- [15] A. Rajendran, D. Kokidko, B. Durant, S.-C. Chou, and E. DeLuca, “Dynamic Response of S-2 Glass Reinforced Plastic Structural Armor,” ARMY RESEARCH LAB WATERTOWN MA MATERIALS DIRECTORATE, Dec. 1993. Accessed: Mar. 09, 2022. [Online]. Available: <https://apps.dtic.mil/sti/citations/ADA273868>
- [16] N. R. Scott, A. Rajendran, M. Nelms, and V. Prakash, “A New Woven Composite Constitutive Model Validated by Shock Wave Experiments,” *Journal of Applied Physics*, p. 32.
- [17] S. Lee and G. Ravichandran, “An investigation of cracking in brittle solids under dynamic compression using photoelasticity,” *Optics and Lasers in Engineering*, vol. 40, no. 4, pp. 341–352, Oct. 2003, doi: 10.1016/S0143-8166(02)00201-4.
- [18] H. Horii and S. Nemat-Nasser, “Compression-induced microcrack growth in brittle solids: Axial splitting and shear failure,” *J. Geophys. Res.*, vol. 90, no. B4, p. 3105, 1985, doi: 10.1029/JB090iB04p03105.
- [19] H. Horii and S. Nemat-Nasser, “Brittle failure in compression: splitting faulting and brittle-ductile transition,” *Philosophical Transactions of the Royal Society of London. Series A, Mathematical and Physical Sciences*, vol. 319, no. 1549, pp. 337–374, Sep. 1986, doi: 10.1098/rsta.1986.0101.
- [20] T. W. Hohenberger, R. J. Windslow, N. M. Pugno, and J. J. C. Busfield, “A CONSTITUTIVE MODEL FOR BOTH LOW AND HIGH STRAIN NONLINEARITIES IN HIGHLY FILLED ELASTOMERS AND IMPLEMENTATION WITH USER-DEFINED MATERIAL SUBROUTINES IN ABAQUS,” *Rubber Chemistry and Technology*, vol. 92, no. 4, pp. 653–686, Oct. 2019, doi: 10.5254/rct.19.80387.
- [21] “VUMAT.” <https://abaqus-docs.mit.edu/2017/English/SIMACAESUBRefMap/simasub-c-vumat.htm> (accessed Mar. 06, 2022).
- [22] J. Bergström, “10 - User Material Subroutines,” in *Mechanics of Solid Polymers*, J. Bergström, Ed. William Andrew Publishing, 2015, pp. 447–454. doi: 10.1016/B978-0-323-31150-2.00010-8.
- [23] V. Crespo Cuevas, *Linking ABAQUS 2019 and Intel oneAPI Base Toolkit (FORTRAN Compiler)*. 2021. doi: 10.13140/RG.2.2.21568.05126.
- [24] T. T. K. Dat, *Linking Abaqus 2020 & Intel Fortran Compiler 19.1 (2020) & Visual Studio 2019 in Windows 10 x64*. 2020. doi: 10.13140/RG.2.2.33539.32800.
- [25] L. M. Barker, C. D. Lundergan, P. J. Chen, and M. E. Gurtin, “Nonlinear Viscoelasticity and the Evolution of Stress Waves in Laminated Composites: A Comparison of Theory and Experiment,” *Journal of Applied Mechanics*, vol. 41, no. 4, pp. 1025–1030, Dec. 1974, doi: 10.1115/1.3423427.
- [26] L. Tsai and V. Prakash, “Structure of weak shock waves in 2-D layered material systems,” *International Journal of Solids and Structures*, vol. 42, no. 2, pp. 727–750, Jan. 2005, doi: 10.1016/j.ijsolstr.2004.06.030.
- [27] “Finite element conversion to SPH particles.” <https://abaqus-docs.mit.edu/2017/English/SIMACAEANLRefMap/simaanl-c-sphconversion.htm> (accessed Apr. 10, 2022).
- [28] S. Murakami and Y. Liu, “LOCAL APPROACH OF FRACTURE BASED ON CONTINUUM DAMAGE MECHANICS AND THE RELATED PROBLEMS,” *Journal of the Society of Materials Science, Japan*, vol. 45, no. 9Appendix, pp. 131–142, 1996, doi: 10.2472/jsms.45.9Appendix_131.

- [29] N. R. Scott, “Computational Modeling Of Shock Wave Propagation In A Layered Composites,” p. 84.
- [30] “S-2 Glass® Fiber.”
<https://www.matweb.com/search/DataSheet.aspx?MatGUID=881df8cd9bde4344820202eb6d1e7a39&ckck=1> (accessed Mar. 30, 2022).

APPENDIX

APPENDIX A

$$\Psi_{\text{iso}} = \frac{G}{2} \left(I_1 J^{\frac{2}{3}} - 3 \right)$$

$$J = \det \left(\mathbf{C}^{\frac{1}{2}} \right) = I_3^{\frac{1}{2}}$$

$$\therefore \Psi_{\text{iso}} = \frac{G}{2} \left(I_1 I_3^{\frac{1}{3}} - 3 \right)$$

$$\frac{\partial I_1}{\partial \mathbf{C}} = \mathbf{I}, \quad \frac{\partial I_3}{\partial \mathbf{C}} = I_3 \mathbf{C}^{-1}$$

$$\therefore \frac{\partial \Psi_{\text{iso}}}{\partial I_1} = \frac{\partial}{\partial I_1} \left(\frac{G}{2} \left(I_1 I_3^{\frac{1}{3}} - 3 \right) \right) = \frac{G}{2} I_3^{\frac{1}{3}}$$

$$\therefore \frac{\partial \Psi_{\text{iso}}}{\partial I_3} = \frac{G}{2} I_1 \left(-\frac{1}{3} \right) I_3^{-\frac{4}{3}}$$

$$\therefore \mathbf{S}_{\text{iso}} = 2 \left(\frac{G}{2} I_3^{\frac{1}{3}} \right) (\mathbf{I}) + 2 \left(-\frac{G}{6} I_1 I_3^{-\frac{4}{3}} \right) (I_3 \mathbf{C}^{-1}) = G I_3^{\frac{1}{3}} \left(\mathbf{I} - \frac{I_1}{3} \mathbf{C}^{-1} \right) = \frac{G}{J^{\frac{2}{3}}} \left(\mathbf{I} - \frac{I_1}{3} \mathbf{C}^{-1} \right)$$

$$\Psi_{\text{vol}} = \frac{K}{\beta^2} (\beta \ln(J) + J^{-\beta} - 1)$$

$$I_3 = J^2$$

$$\begin{aligned} \therefore \mathbf{S}_{\text{vol}} &= 2 \frac{K}{\beta^2} \frac{\partial}{\partial \mathbf{C}} \left(\beta \ln \left(I_3^{\frac{1}{2}} \right) + I_3^{\frac{\beta}{2}} - 1 \right) = 2 \frac{K}{\beta^2} \left(\frac{\beta}{2} \left(\frac{1}{I_3} \right) (I_3 \mathbf{C}^{-1}) - \frac{\beta}{2} \left(I_3^{\frac{\beta}{2}-1} \right) (I_3 \mathbf{C}^{-1}) \right) \\ &= \frac{K}{\beta} \left(\mathbf{C}^{-1} - I_3^{\frac{\beta}{2}} \mathbf{C}^{-1} \right) = \frac{K}{\beta} (1 - J^{-\beta}) \mathbf{C}^{-1} \end{aligned}$$

$$\Psi_{\text{aniso}} = \frac{k_1}{2} (I_4 - 1)^2$$

$$\therefore \mathbf{S}_{\text{aniso}} = 2 \frac{\partial}{\partial \mathbf{C}} \left(\frac{k_1}{2} (I_4 - 1)^2 \right) = 2 \left(k_1 (I_4 - 1) \frac{\partial I_4}{\partial \mathbf{C}} \right) = 2k_1 (\mathbf{M}_1 \cdot \mathbf{C} \mathbf{M}_1 - 1) \mathbf{M}_1 \otimes \mathbf{M}_1$$

APPENDIX B

```

C
SUBROUTINE VUMAT(
!     nblock, ndir, nshr, nstatev, nfieldv, nprops, lanneal,
!     stepTime, totalTime, dt, cmname, coordMp, charLength,
!     props, density, strainInc, relSpinInc,
!     tempOld, stretchOld, defgradOld, fieldOld,
!     stressOld, stateOld, enerInternOld, enerInelasOld,
!     tempNew, stretchNew, defgradNew, fieldNew,
!     stressNew, stateNew, enerInternNew, enerInelasNew )
C
INCLUDE 'vaba_param.inc'
C
DIMENSION props(nprops), density(nblock), coordMp(nblock,*),
!     charLength(nblock), strainInc(nblock,ndir+nshr),
!     relSpinInc(nblock,nshr), tempOld(nblock),
!     stretchOld(nblock,ndir+nshr),
!     defgradOld(nblock,ndir+nshr),
!     fieldOld(nblock,nfieldv), stressOld(nblock,ndir+nshr),
!     stateOld(nblock,nstatev), enerInternOld(nblock),
!     enerInelasOld(nblock), tempNew(nblock),
!     stretchNew(nblock,ndir+nshr),
!     defgradNew(nblock,ndir+nshr),
!     fieldNew(nblock,nfieldv),
!     stressNew(nblock,ndir+nshr), stateNew(nblock,nstatev),
!     enerInternNew(nblock), enerInelasNew(nblock)
C
CHARACTER*80 cmname
C
NUMBER DEFINITIONS
C
-----
REAL*8 zero, one, two, three, four, ten, half, third, twothirds,
!     deetee
PARAMETER(zero = 0.d0, one = 1.d0, two = 2.d0, three = 3.d0,
!     four = 4.d0, ten = 10.d0, half = 0.5d0, third = 1.d0/3.d0,
!     twothirds = 2.d0/3.d0, deetee = 1.d0*(10.d0**(-9.d0))
C
LOCAL VARIABLES
C
-----
REAL*8 G, Kay, beta, k1, k2, M11, M12, M13, M21, M22, M23,
!     clems, Jec, Jet, iota, ems, tcrit, ccrit, C11, C22, C33,
!     C44, C55, C66, C12, C13, C23, eta, alpha, clalpha, trace,
!     J, Cxx, Cyy, Czz, Cxy, Cyz, Cxz, Ubarxx, Ubaryy, Ubarzz,
!     Ubarxy, Ubaryz, Ubarxz, Ubar2xx, Ubar2yy, Ubar2zz, Ubar2xy,
!     Ubar2yz, Ubar2xz, I1, p0, Gfac, facxx, facyy, faczz, facxy,
!     facyz, facxz, fac2, m1dpm1, m2dpm2, mloutxx, mloutyy,
!     mloutzz, m2outxx, m2outyy, m2outzz, fac3xx1, fac3xx2,
!     fac3yy1, fac3yy2, fac3zz1, fac3zz2, exx, eyy, ezz, exy,
!     eyz, exz, epeqold, epeq, strrate, Rmeold, Rmsold, Rms, Rme,

```

```

!      lograte, emsadj, alphaadj, Rm, matdamCurrent, matdamOld,
!      matdamNew, Rfit1, Rfit2, Rfic1, Rfic2, fibdam1, fibdam2,
!      fibdam1Old, fibdam2Old, fibdam1New, fibdam2New, Totaldam,
!      Kayd, Kdterm, uliniso, active, inactive
C
C      MATERIAL PROPERTIES
C      -----
G      = props(1)
Kay    = props(2)
beta   = props(3)
k1     = props(4)
k2     = props(5)
M11    = props(6)
M12    = props(7)
M13    = props(8)
M21    = props(9)
M22    = props(10)
M23    = props(11)
clems  = props(12)
Jec    = props(13)
Jet    = props(14)
iota   = props(15)
ems    = props(16)
tcrit  = props(17)
ccrit  = props(18)
C11    = props(19)
C22    = props(20)
C33    = props(21)
C44    = props(22)
C55    = props(23)
C66    = props(24)
C12    = props(25)
C13    = props(26)
C23    = props(27)
eta    = props(28)
alpha  = props(29)
clalpha= props(30)
C
C      *****
C      ----- INITIALIZE MATERIAL AS LINEARLY ELASTIC -----
C      *****
C
IF (totalTime.EQ.0.0) THEN
DO i = 1,nblock
      trace = strainInc(i,1) + strainInc(i,2) +
!          strainInc(i,3)
      stressNew(i,1) = stressOld(i,1) +
!          two * G * strainInc(i,1) +
!          (Kay - (twothirds * G)) * trace
      stressNew(i,2) = stressOld(i,2) +
!          two * G * strainInc(i,2) +
!          (Kay - (twothirds * G)) * trace
      stressNew(i,3) = stressOld(i,3) +
!          two * G * strainInc(i,3) +
!          (Kay - (twothirds * G)) * trace
      stressNew(i,4) = stressOld(i,4) +
!          two * G * strainInc(i,4)

```

```

                stressNew(i,5) = stressOld(i,5) +
!                two * G * strainInc(i,5)
                stressNew(i,6) = stressOld(i,6) +
!                two * G * strainInc(i,6)
END DO
RETURN
END IF

C
C *****
C ----- START LOOP FOR USER CALCULATIONS -----
C *****
C
DO k = 1,nblock

C
C   CALCULATE J = |F| = |U|
C   -----
C   J =   stretchNew(k,1) *
!       ( stretchNew(k,2) * stretchNew(k,3)   -
!       stretchNew(k,5) * stretchNew(k,5) ) +
!       stretchNew(k,4) *
!       ( stretchNew(k,5) * stretchNew(k,6)   -
!       stretchNew(k,3) * stretchNew(k,4) ) +
!       stretchNew(k,6) *
!       ( stretchNew(k,4) * stretchNew(k,5)   -
!       stretchNew(k,2) * stretchNew(k,6) )

C
C   CALCULATE RIGHT CAUCHY TENSOR, C = U*U
C   -----
C   Cxx = stretchNew(k,1) * stretchNew(k,1) +
!       stretchNew(k,4) * stretchNew(k,4) +
!       stretchNew(k,6) * stretchNew(k,6)
C   Cyy = stretchNew(k,2) * stretchNew(k,2) +
!       stretchNew(k,4) * stretchNew(k,4) +
!       stretchNew(k,5) * stretchNew(k,5)
C   Czz = stretchNew(k,3) * stretchNew(k,3) +
!       stretchNew(k,6) * stretchNew(k,6) +
!       stretchNew(k,5) * stretchNew(k,5)
C   Cxy = stretchNew(k,1) * stretchNew(k,4) +
!       stretchNew(k,4) * stretchNew(k,2) +
!       stretchNew(k,6) * stretchNew(k,5)
C   Cyz = stretchNew(k,4) * stretchNew(k,6) +
!       stretchNew(k,2) * stretchNew(k,5) +
!       stretchNew(k,5) * stretchNew(k,3)
C   Cxz = stretchNew(k,1) * stretchNew(k,6) +
!       stretchNew(k,4) * stretchNew(k,5) +
!       stretchNew(k,6) * stretchNew(k,3)

C
C   CALCULATE MODIFIED STRETCH TENSOR, Ubar = U/(J^1/3)
C   -----
C   Ubarxx = stretchNew(k,1) / (J**third)
C   Ubaryy = stretchNew(k,2) / (J**third)
C   Ubarzz = stretchNew(k,3) / (J**third)
C   Ubarxy = stretchNew(k,4) / (J**third)
C   Ubaryz = stretchNew(k,5) / (J**third)
C   Ubarxz = stretchNew(k,6) / (J**third)

C
C   CALCULATE MODIFIED STRETCH TENSOR SQUARED, Ubar^2

```

```

C -----
Ubar2xx = Ubarxx * Ubarxx
Ubar2yy = Ubaryy * Ubaryy
Ubar2zz = Ubarzz * Ubarzz
Ubar2xy = Ubarxy * Ubarxy
Ubar2yz = Ubaryz * Ubaryz
Ubar2xz = Ubarxz * Ubarxz

C
C FIRST INVARIANT OF Ubar^2 = tr(Ubar2)
C -----
C I1 = Ubar2xx + Ubar2yy + Ubar2zz
C
C ISOCHORIC TERM
C -----
C p0 = third * I1
Gfac = G / J

C
C facxx = Gfac * (Ubar2xx - p0)
C facyy = Gfac * (Ubar2yy - p0)
C faczz = Gfac * (Ubar2zz - p0)
C facxy = Gfac * Ubar2xy
C facyz = Gfac * Ubar2yz
C facxz = Gfac * Ubar2xz

C
C VOLUMETRIC CAUCHY STRESS TERM
C -----
C fac2 = (Kay / (J * beta)) * (one - (one / (J**beta)))
C
C MATRIX DIRECTION DEFINITIONS
C -----
! m1dpm1 = M11 * (M11 * Cxx + M12 * Cxy + M13 * Cxz) +
! M12 * (M11 * Cxy + M12 * Cyy + M13 * Cyz) +
! M13 * (M11 * Cxz + M12 * Cyz + M13 * Czz)
! m2dpm2 = M21 * (M21 * Cxx + M22 * Cxy + M23 * Cxz) +
! M22 * (M21 * Cxy + M22 * Cyy + M23 * Cyz) +
! M23 * (M21 * Cxz + M22 * Cyz + M23 * Czz)

C
C MATRIX OUTER PRODUCTS
C -----
! m1outxx = (stretchNew(k,1) * M11 + stretchNew(k,4) * M12 +
! stretchNew(k,6) * M13)**two
! m1outyy = (stretchNew(k,4) * M11 + stretchNew(k,2) * M12 +
! stretchNew(k,5) * M13)**two
! m1outzz = (stretchNew(k,6) * M11 + stretchNew(k,5) * M12 +
! stretchNew(k,3) * M13)**two
! m2outxx = (stretchNew(k,1) * M21 + stretchNew(k,4) * M22 +
! stretchNew(k,6) * M23)**two
! m2outyy = (stretchNew(k,4) * M21 + stretchNew(k,2) * M22 +
! stretchNew(k,5) * M23)**two
! m2outzz = (stretchNew(k,6) * M21 + stretchNew(k,5) * M22 +
! stretchNew(k,3) * M23)**two

C
C ANISOTROPIC STRESSES
C -----
C fac3xx1 = (two * k1 / J) * (m1dpm1 - one) * m1outxx
C fac3xx2 = (two * k2 / J) * (m2dpm2 - one) * m2outxx
C fac3yy1 = (two * k1 / J) * (m1dpm1 - one) * m1outyy

```

C
C
C

```
fac3yy2 = (two * k2 / J) * (m2dpm2 - one) * m2outyy  
fac3zz1 = (two * k1 / J) * (m1dpm1 - one) * m1outzz  
fac3zz2 = (two * k2 / J) * (m2dpm2 - one) * m2outzz
```

MATRIX DAMAGE CRITERIA

```
-----  
exx = twothirds * (stretchNew(k,1) - one) -  
!  
! third * (stretchNew(k,2) - one) -  
! third * (stretchNew(k,3) - one)  
eyy = twothirds * (stretchNew(k,2) - one) -  
!  
! third * (stretchNew(k,1) - one) -  
! third * (stretchNew(k,3) - one)  
ezz = twothirds * (stretchNew(k,3) - one) -  
!  
! third * (stretchNew(k,1) - one) -  
! third * (stretchNew(k,2) - one)  
exy = two * stretchNew(k,4)  
eyz = two * stretchNew(k,5)  
exz = two * stretchNew(k,6)  
epeqold = stateOld(k,1)  
epeq = twothirds * sqrt((three / two) * (exx**two + eyy**two +  
!  
! ezz**two) + (three / four) * (exy**two + eyz**two + exz**two))  
stateNew(k,1) = epeq  
strrate = (epeq - epeqold) / deetee  
Rmsold = stateOld(k,2)  
Rmeold = stateOld(k,3)  
IF (strrate.LT.one) THEN  
    Rms = Rmsold  
    Rme = Rmeold  
    lograte = zero  
    emsadj = ems  
    alphaadj = alpha  
ELSE  
    lograte = log(abs(strrate))  
    emsadj = ems * (one + clems * lograte)  
    Rms = epeq / emsadj  
    IF (J.GT.one) THEN  
        Rme = (J - one) / (Jet - one)  
    ELSE  
        alphaadj = alpha * (one + clalpha * lograte)  
        Rme = alphaadj * (one - J) * exp(J / Jec)  
    END IF  
END IF  
stateNew(k,2) = Rms  
stateNew(k,3) = Rme  
Rm = sqrt((Rms**two) + (Rme**two))  
IF (Rm.LT.one) THEN  
    matdamCurrent = zero  
ELSE  
    matdamCurrent = one - exp((one - Rm) / iota)  
END IF  
matdamOld = stateOld(k,4)  
IF (matdamCurrent.GE.matdamOld) THEN  
    matdamNew = matdamCurrent  
ELSE  
    matdamNew = matdamOld  
END IF  
stateNew(k,4) = matdamNew
```

C
C
C

FIBER DAMAGE CRITERIA

```
-----  
Rfit1 = (m1dpm1 - one) / tcrit  
Rfit2 = (m2dpm2 - one) / tcrit  
Rfic1 = (m1dpm1 - one) / ccrit  
Rfic2 = (m2dpm2 - one) / ccrit  
IF (Rfit1.GT.one) THEN  
    fibdam1 = one  
ELSE IF (Rfic1.GT.one .AND. matdamNew.EQ.zero) THEN  
    fibdam1 = one - eta  
ELSE IF (Rfic1.GT.one .AND. matdamNew.GT.zero) THEN  
    fibdam1 = one  
ELSE  
    fibdam1 = zero  
END IF  
IF (Rfit2.GT.one) THEN  
    fibdam2 = one  
ELSE IF (Rfic2.GT.one .AND. matdamNew.EQ.zero) THEN  
    fibdam2 = one - eta  
ELSE IF (Rfic2.GT.one .AND. matdamNew.GT.zero) THEN  
    fibdam2 = one  
ELSE  
    fibdam2 = zero  
END IF  
fibdam1Old = stateOld(k,5)  
fibdam2Old = stateOld(k,6)  
IF (fibdam1.GE.fibdam1Old) THEN  
    fibdam1New = fibdam1  
ELSE  
    fibdam1New = fibdam1Old  
END IF  
IF (fibdam2.GE.fibdam2Old) THEN  
    fibdam2New = fibdam2  
ELSE  
    fibdam2New = fibdam2Old  
END IF  
stateNew(k,5) = fibdam1New  
stateNew(k,6) = fibdam2New
```

C
C
C

COROTATIONAL CAUCHY STRESSES

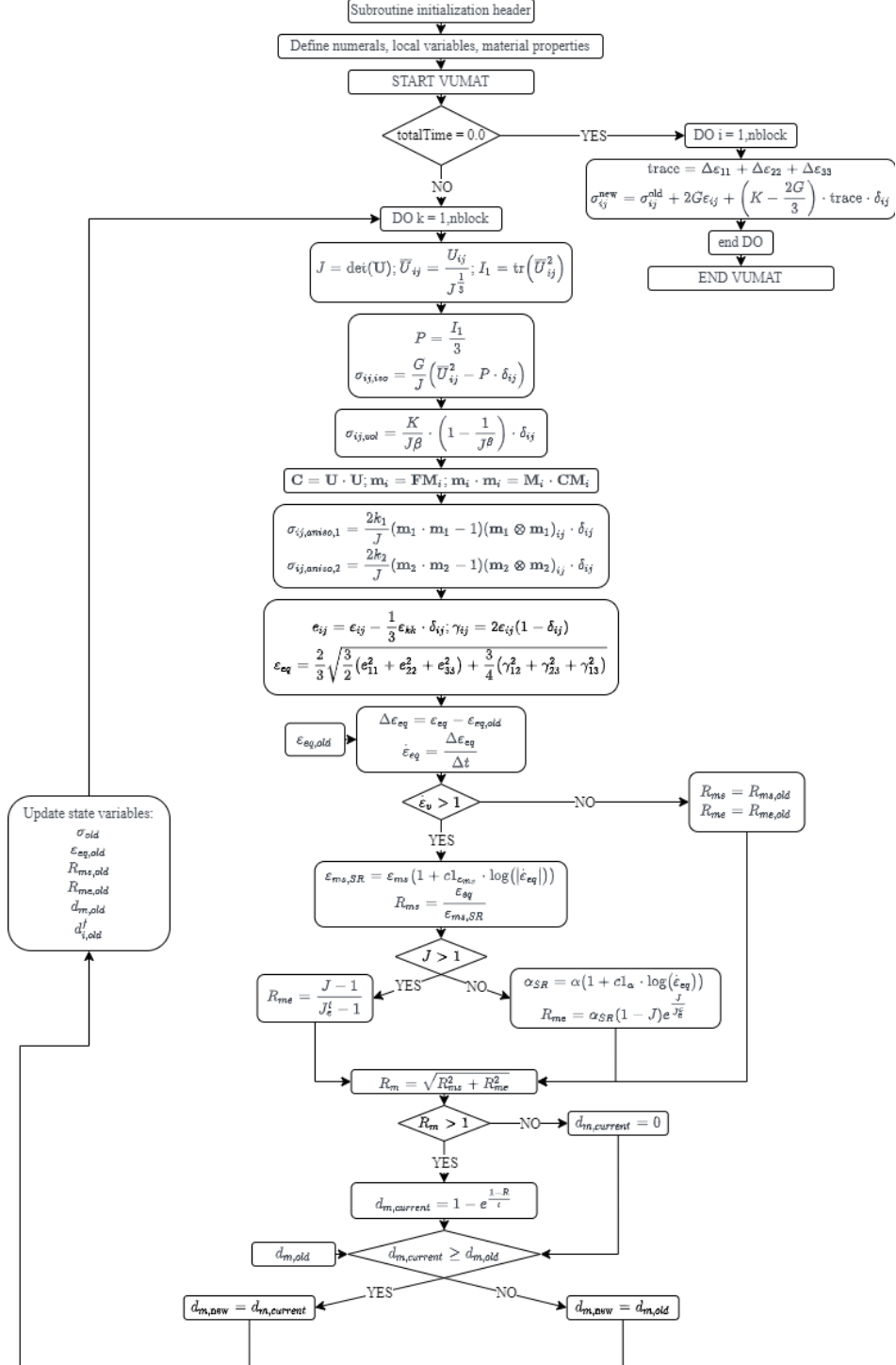
```
-----  
Totaldam = matdamNew + fibdam1New + fibdam2New  
IF (Totaldam.EQ.zero) THEN  
    stressNew(k,1) = C11 * (stretchNew(k,1) - one) +  
!   C12 * (stretchNew(k,2) - one) + C13 * (stretchNew(k,3) -  
!   one)  
    stressNew(k,2) = C12 * (stretchNew(k,1) - one) +  
!   C22 * (stretchNew(k,2) - one) + C23 * (stretchNew(k,3) -  
!   one)  
    stressNew(k,3) = C13 * (stretchNew(k,1) - one) +  
!   C23 * (stretchNew(k,2) - one) + C33 * (stretchNew(k,3) -  
!   one)  
    stressNew(k,4) = C66 * two * stretchNew(k,4)  
    stressNew(k,5) = C55 * two * stretchNew(k,5)  
    stressNew(k,6) = C44 * two * stretchNew(k,6)  
ELSE
```

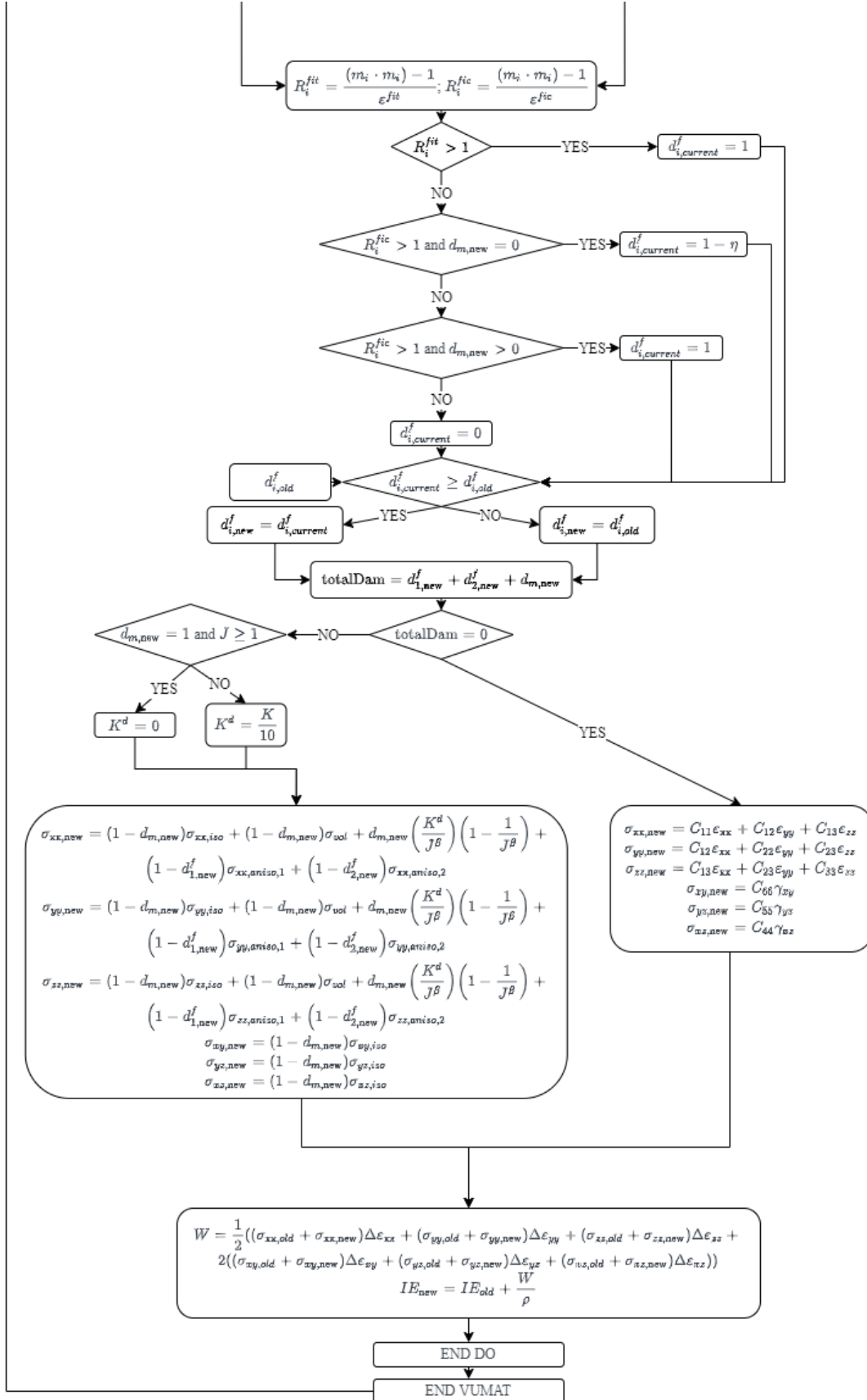
```

      IF (matdamNew.EQ.one .AND. J.GE.one .AND.
!       fibdam1New.EQ.one .AND. fibdam2New.EQ.one) THEN
      ELSE
        Kayd = Kay / ten
      END IF
      Kdterm = (Kayd / (J * beta)) * (one -
!       (one / (J**beta)))
      stressNew(k,1) = (one - matdamNew) * facxx +
!       (one - matdamNew) * fac2 + matdamNew * Kdterm +
!       (one - fibdam1New) * fac3xx1 + (one - fibdam2New) * fac3xx2
      stressNew(k,2) = (one - matdamNew) * facyy +
!       (one - matdamNew) * fac2 + matdamNew * Kdterm +
!       (one - fibdam1New) * fac3yy1 + (one - fibdam2New) * fac3yy2
      stressNew(k,3) = (one - matdamNew) * faczz +
!       (one - matdamNew) * fac2 + matdamNew * Kdterm +
!       (one - fibdam1New) * fac3zz1 + (one - fibdam2New) * fac3zz2
      stressNew(k,4) = (one - matdamNew) * facxy
      stressNew(k,5) = (one - matdamNew) * facyz
      stressNew(k,6) = (one - matdamNew) * facxz
      END IF
C
C     UPDATE SPECIFIC INTERNAL ENERGY
C     -----
      uliniso = half*((stressOld(k,1)+stressNew(k,1))*strainInc(k,1)+
!       (stressOld(k,2)+stressNew(k,2))*strainInc(k,2) +
!       (stressOld(k,3)+stressNew(k,3))*strainInc(k,3) +
!       two * ( (stressOld(k,4) + stressNew(k,4))*
!       strainInc(k,4) +
!       (stressOld(k,5) + stressNew(k,5))*
!       strainInc(k,5) +
!       (stressOld(k,6) + stressNew(k,6))*
!       strainInc(k,6) ) )
C
      enerInternNew(k) = enerInternOld(k) + uliniso / density(k)
      END DO
C
      RETURN
C
      END SUBROUTINE VUMAT

```

APPENDIX C





APPENDIX D

$$\left[\begin{array}{l}
 (U_{1M11}+U_{4M12}+U_{6M13})^2 \\
 (U_{4M11} + U_{2M12} + U_{5M13})(U_{1M11} + U_{4M12} + U_{6M13}) \\
 (U_{6M11} + U_{5M12} + U_{3M13})(U_{1M11} + U_{4M12} + U_{6M13})
 \end{array} \right]$$

$$\begin{array}{l}
 (U_{1M11}+U_{4M12}+U_{6M13})(U_{4M11}+U_{2M12}+U_{5M13}) \\
 (U_{4M11} + U_{2M12} + U_{5M13})^2 \\
 (U_{6M11} + U_{5M12} + U_{3M13})(U_{4M11} + U_{2M12} + U_{5M13})
 \end{array}$$

$$\begin{array}{l}
 (U_{1M11}+U_{4M12}+U_{6M13})(U_{6M11}+U_{5M12}+U_{3M13}) \\
 (U_{4M11} + U_{2M12} + U_{5M13})(U_{6M11} + U_{5M12} + U_{3M13}) \\
 (U_{6M11} + U_{5M12} + U_{3M13})^2
 \end{array}$$

VITA

EDUCATION

Bachelor of Science, majoring in Mechanical Engineering, minoring in Mathematics

University of Louisiana at Lafayette, Lafayette, LA, 2020

PRIOR EMPLOYMENT

Graduate Teaching Assistant

University of Mississippi, Oxford, MS, 2020-2022

Mechanical Plant Engineer Intern

Snowy Hydro Ltd., Cabramurra, NSW, 2019